

**MAGNETIC ORDER IN THE FCC KAGOME  
ANTIFERROMAGNET**

by ©

Martin LeBlanc

Thesis submitted to the School of Graduate Studies in partial fulfillment of the  
requirements for the degree of

**Doctor of Philosophy (Condensed Matter Physics)**

**Department of Physics and Physical Oceanography**

Memorial University of Newfoundland

**January 5, 2017**

St. John's, Newfoundland

## Abstract

The research in this thesis was inspired by a particular magnetic compound,  $\text{IrMn}_3$ , which has been used extensively as the antiferromagnetic layer for exchange pinning in spin valves for computer hard disk drives and other magnetic storage technologies. Its magnetic structure is the fcc kagome lattice, where 2D kagome layers are ABC stacked along [111] to give a full 3D lattice. To gain a better understanding of its basic spin structure and dynamics, several theoretical techniques are considered and an experiment was performed with a focus on examining the effect of adding magnetic anisotropy to the Heisenberg fcc kagome lattice model.

Monte Carlo simulations using the standard Metropolis algorithm are performed for the fcc kagome lattice with the addition of cubic magnetocrystalline anisotropy  $K$ . Comparisons are made between previous  $K = 0$  results and  $K > 0$  through spin order parameters and the specific heat, to study anisotropy effects on the spin degeneracies associated with the 3D kagome spin lattice. A look at energy histograms and Binder energy cumulants reveals a change from a first order to a continuous phase transition with the addition of anisotropy, associated with the removal of ground state degeneracies.

Magnetic neutron scattering experiments were carried out on a  $\text{IrMn}_3$  powder sample at the Oak Ridge National Laboratory to study the magnetic structure and determine whether anisotropy could be detected. Spin waves along with elastic and inelastic magnetic scattering theories are developed for the fcc lattice in an attempt to compare to the experiment. While noise in the data makes this quite difficult, the expected results may help shed some light on this material for future experiments on single crystals.

**Keywords:**  $\text{IrMn}_3$ ; Monte Carlo; Magnetic Neutron Scattering

## Acknowledgments

I would first like to extend tremendous appreciation to my primary supervisor, Prof. Martin Plumer. His patience and assistance enabled this project to continue when it otherwise had issues. He has acted as a mentor from which I have learned innumerable things and I am deeply thankful. Prof. John Whitehead, as co-supervisor, has always been willing to offer his time and support. There have been several hurdles that were overcome thanks to him for which I am grateful. Many elaborate discussions with Prof. Byron Southern from the University of Manitoba allowed this work to continue. His insight and hard work in helping develop theory for this project are well appreciated.

My thesis committee has been patient and instrumental to the success of this work. A willingness to lend their time and critical comments was well appreciated.

The Department of Physics and Physical Oceanography and its people at Memorial University of Newfoundland have provided an excellent and supportive environment. I am also grateful for the financial support received that made this project possible. Special thanks are extended to the group that helped us at Oak Ridge National Laboratory which allowed us to conduct an interesting experiment.

The support my family has provided has been a formidable asset. I would very much like to thank them for valuable support and encouragement. Similarly, I express gratitude to my friends for their help throughout this process.

Finally, this would not have been possible without the inspiration and perspective gained from many, many others that I have had the pleasure to interact with and admire. From acquaintances, to strangers, to simply passersby, I have gained much knowledge and taken many ideas simply from observations and interactions.

Thank you.

# Contents

<b>1</b>	<b>Introduction: Motivation</b>	<b>1</b>
1.1	The fcc Kagome Antiferromagnet . . . . .	1
1.2	Kagome Lattice . . . . .	5
1.2.1	2D Kagome Lattice . . . . .	5
1.2.2	3D Kagome Lattice . . . . .	8
1.3	Outline of the Thesis . . . . .	10
<b>2</b>	<b>Introduction: Techniques</b>	<b>12</b>
2.1	Monte Carlo Methods . . . . .	12
2.1.1	Introduction to Monte Carlo . . . . .	12
2.1.2	Principles of Monte Carlo . . . . .	12
2.1.3	Metropolis Algorithm . . . . .	14
2.1.4	Thermodynamic Quantities . . . . .	15
2.1.5	First-Order vs Continuous Phase Transitions . . . . .	16
2.2	Neutron Scattering and Spin Waves . . . . .	18
2.2.1	Motivation . . . . .	18
2.2.2	Spin Wave Theory . . . . .	19
2.2.3	Magnetic Neutron Scattering . . . . .	22

<b>3</b>	<b>Monte Carlo simulations of the fcc kagome lattice: Competition between triangular frustration and cubic anisotropy</b>	<b>28</b>
3.1	Introduction . . . . .	29
3.2	Model . . . . .	30
3.3	Previous Simulation Results $K = 0$ . . . . .	32
3.4	Ground State Properties . . . . .	36
3.5	Simulation Results . . . . .	39
3.6	Summary and Conclusions . . . . .	48
<b>4</b>	<b>Magnetic Elastic Scattering</b>	<b>51</b>
4.1	Nuclear cross section . . . . .	51
4.2	Magnetic form factor . . . . .	53
4.3	Magnetic cross section . . . . .	54
<b>5</b>	<b>Spin Waves and Inelastic Magnetic Scattering in the Anisotropic fcc Kagome Antiferromagnet</b>	<b>60</b>
5.1	Introduction . . . . .	60
5.2	Spin Wave Theory . . . . .	63
5.3	Spin Wave Analysis . . . . .	69
5.3.1	Zero Anisotropy . . . . .	69
5.3.2	Effects of Anisotropy . . . . .	72
5.3.3	Summary . . . . .	74
5.4	Inelastic Scattering - Spin Wave Theory . . . . .	75
5.4.1	Neutron Scattering for Single Crystals . . . . .	76
5.4.2	Powder Averaging . . . . .	77
5.4.3	Oak Ridge Results . . . . .	83

<b>6</b>	<b>Discussion and Conclusions</b>	<b>86</b>
6.1	Monte Carlo Simulations . . . . .	87
6.2	Elastic Neutron Scattering . . . . .	88
6.3	Spin Waves and Inelastic Neutron Scattering . . . . .	88
6.4	Future Areas of Study . . . . .	90
	<b>Bibliography</b>	<b>92</b>
<b>A</b>	<b>Magnetic Neutron Scattering</b>	<b>98</b>
A.1	General Derivation . . . . .	98
	A.1.1 Neutron Scattering . . . . .	98
	A.1.2 Nuclear Scattering . . . . .	100
	A.1.3 Magnetic Scattering . . . . .	100
A.2	Elastic Scattering . . . . .	102
A.3	Inelastic Scattering . . . . .	105
	A.3.1 Green's Functions . . . . .	105
	A.3.2 Calculation of $S(\boldsymbol{\kappa}, \omega)$ . . . . .	107
A.4	Elastic Cut of Experimental Data . . . . .	108
A.5	Single Crystal Calculations . . . . .	109

# List of Tables

4.1	Dimensionless Mn constants for different oxidation states as used in the magnetic form factor [53]. . . . .	53
4.2	Relative magnetic peak heights from Eq. 4.4, Tab. 4.1 and Eq. 4.12.	57

# List of Figures

1.1	Schematic showing a 2D kagome lattice, made by removing sites at the center of each empty hexagon from the triangular lattice. . . . .	2
1.2	Schematic of a read-head structure. . . . .	4
1.3	Schematic showing a 2D kagome lattice a) $q = 0$ and b) $\sqrt{3} \times \sqrt{3}$ $120^\circ$ structures. Three sublattices $A$ , $B$ , and $C$ are shown that make up the spins of the lattice, each making $120^\circ$ angles with its neighbor spins. The $z$ axis is outside the plane, along the $[111]$ cubic direction when used to describe the 3D kagome lattice. A kagome structure is highlighted for the $q = 0$ case using lines. . . . .	6
1.4	The fcc kagome lattice with magnetic Mn ions on cube faces forming stacked 2D kagome layers along the $(111)$ axis. Nonmagnetic Ir ions are at the corners. The four interlayer exchange interactions ( $J$ ) are indicated [13]. . . . .	9
3.1	Schematic showing a $120^\circ$ ground-state spin structure (blue arrows) in the cubic $(111)$ plane, along with the local $[100]$ anisotropy axis directions (red rods). The cube shown has sides of length $a/2$ , where $a$ is the lattice constant of the fcc unit cell [13]. . . . .	31

3.2	Double-peak seen in the energy histogram of the Heisenberg fcc kagome lattice near the Néel temperature for $K = 0$ indicative of a weakly first order transition. Figure taken from [12]. . . . .	34
3.3	Magnetization order parameter vs temperature for individual sublattices ( $M_1$ , $M_2$ , and $M_3$ or $A$ , $B$ , and $C$ ) at $K = 0$ for the $XY$ model corresponding to three different cooling simulations, (a), (b), and (c). The Heisenberg model showed the same behavior. Figure taken from [12]. . . . .	35
3.4	Interspin angle and magnetic moment at zero temperature vs anisotropy strength [13]. . . . .	39
3.5	Sublattice magnetization order parameter vs temperature for small values of $K$ from simulations with $L = 24$ [13]. . . . .	40
3.6	Specific heat vs temperature used to locate $T_N$ for the values of $K$ indicated from simulations with $L = 24$ . Inset shows results for $K = 10$ and the expected lower broad peak at $T \approx K/6 \approx 1.67$ due to short-range order [13]. . . . .	41
3.7	Néel temperature $T_N$ vs the anisotropy strength $K$ estimated from the specific-heat peaks from simulations with $L = 24$ [13]. . . . .	42
3.8	Simulation results with $L = 24$ for the ferromagnetic magnetization vs temperature for the values of $K$ indicated [13]. . . . .	43
3.9	Energy histograms at values of $T$ near $T_N$ for $K = 0.1$ and $K = 5$ with $L = 36$ from simulations using $L = 24$ [13]. . . . .	45
3.10	Energy cumulants for $K = 0$ and $K = 0.1$ at temperatures close to $T = T_N(L)$ estimated from the specific-heat peaks for the values of $L$ indicated [13]. . . . .	47

3.11	Estimated cumulant minimum vs $1/N$ from the results of Figure 3.10. The broken line shows behavior expected of a model continuous transition [13]. . . . .	48
4.1	Magnetic form factor vs wavevector for different oxidation states of Mn (from Eq. 4.4). . . . .	54
4.2	Elastic scattering showing several peaks for $K/J = 0, 5$ and $J = J' = 1$ . The intensity of the peaks is plotted vs the wavevector $\kappa$ , focusing on the locations of the peaks. The peaks at 111, 200, and 220 are unique to $K > 0$ [14]. . . . .	59
5.1	(a) The fcc lattice is divided into four cubic sublattices, each with lattice constant $a$ and labeled as A, B, C, and D. The D sites (spheres) are non-magnetic whereas the remaining three sublattices (arrows) are magnetic. (b) The A, B, and C sites form a set of kagome lattices stacked along the (111) direction. Figure from Ref. [14], adapted from Ref. [6]. . . . .	62
5.2	Spin wave modes along the $\Gamma X$ and $\Gamma R$ directions (a) $K = 0, J' = 0$ , (b) $K = 0.1J, J' = 0$ , (c) $K = 0, J' = 0.1J$ , (d) $K = 0.1J, J' = 0.1J$ , (e) $K = 0, J' = J$ , (f) $K = 0.1J, J' = J$ [14]. . . . .	73
5.3	Relative magnitude of the inelastic scattering function $S(\kappa, \omega)$ (side bar scale) assuming a single magnetic (111) domain with $J = J' = 1$ with $\kappa \parallel [100]$ . (a) $K=0$ , (b) $K/J=0.1$ , (c) $K=0$ over a smaller region than (a), and (d) $K/J=0.1$ over a smaller region than (b) [14].	76
5.4	Boundaries for $Q_1$ and $Q_2$ showing the (shaded) accessible range for $E_i = 50$ and $100$ meV. . . . .	80

5.5	Calculated powder averaged inelastic intensity. Value of $K$ included in the graphs. Different regions shown for $K = 0$ and $K = 0.1$ . Points of interest at $2\pi$ , $2\pi\sqrt{5}$ , $2\pi\sqrt{9} = 2\pi \cdot 3$ and $2\pi\sqrt{13}$ . Lower panels show details of the lower energy and also higher $Q$ regions. . . . .	81
5.6	Calculated powder inelastic results showing $E$ vs $Q$ for an initial energy $E_i = 100$ meV. Arrows point to the locations corresponding to [100] and [210] around $Q = 1.67 \text{ \AA}^{-1}$ and $3.75 \text{ \AA}^{-1}$ respectively, showing thick vertical bands. An expected band corresponding to [110] around $Q = 2.37 \text{ \AA}^{-1}$ does not appear. Color corresponds to intensity (arbitrary units). Figure provided by Prof. B. Southern (Univ. of Manitoba). . . . .	82
5.7	Experimental inelastic scattering results at $T = 5$ K with an incident energy of 100 meV with the color representing intensity (arbitrary units). Imperfect aluminum intensity subtraction has been done which leads to negative (set to zero) black regions and the colorful red, yellow and green sections towards the bottom. Arrows point to the locations corresponding to [100], [110] and [210] around $Q = 1.67 \text{ \AA}^{-1}$ , $2.36 \text{ \AA}^{-1}$ and $3.75 \text{ \AA}^{-1}$ respectively, showing visible vertical bands. . . . .	84
A.1	Elastic cut of the inelastic data before aluminum subtraction. Peaks are marked in Fig. A.2. . . . .	109
A.2	Elastic cut of the inelastic data after aluminum subtraction. Several known $\text{IrMn}_3$ ordered phase (O), aluminum (Al), and MnO peaks are marked. . . . .	109

A.3	Predicted $S(Q, E)$ intensities for a single crystal sample along specific $Q$ directions. $J = J' = 20$ meV, $K = 2$ meV, and an incident energy of 100 meV. The form factor term is included along with the term $k_f/k_i$ in Eq. 5.31. Figures provided by Prof. B. Southern (Univ. of Manitoba). . . . .	111
-----	--	-----

# Chapter 1

## Introduction: Motivation

### 1.1 The fcc Kagome Antiferromagnet

The research focus of this thesis was motivated by the realization that little work had previously been done to characterize the magnetic order and spin excitations in an unusual, yet popular, 3D frustrated antiferromagnet (AF), namely the fcc kagome lattice. The paradigm for frustration is the triangle with nearest neighbor (NN) AF exchange interactions [1]. Unlike the four NN AF interactions associated with the unfrustrated 2D square lattice, the three spins at the vertices of a triangle cannot all be antiparallel. The typical realization in the zero temperature ( $T = 0$ ) ground state of this frustration for real materials with lattice structures based on the triangle is the  $120^\circ$  spin structure, with spin vectors around the triangle having this inter-angle value. The 2D triangular lattice with six NN is constructed from edge-sharing triangles. The 2D kagome lattice is built from corner-sharing triangles and the word “kagome” comes from an ancient Japanese basket weaving design [2]. The 2D kagome lattice can also be constructed by removing one-quarter of the sites from a triangular lattice, as in Fig. 1.1, and each site has four NN. Over the

past few decades, there have been a very large number of studies on the spin order in the 2D kagome AF (with many kagome-dedicated sessions at conferences). As reviewed in Sec. 1.2, this interest is derived from the large macroscopic degeneracy of the NN AF spin model on this lattice which gives rise to exotic classical and quantum magnetic phenomena.

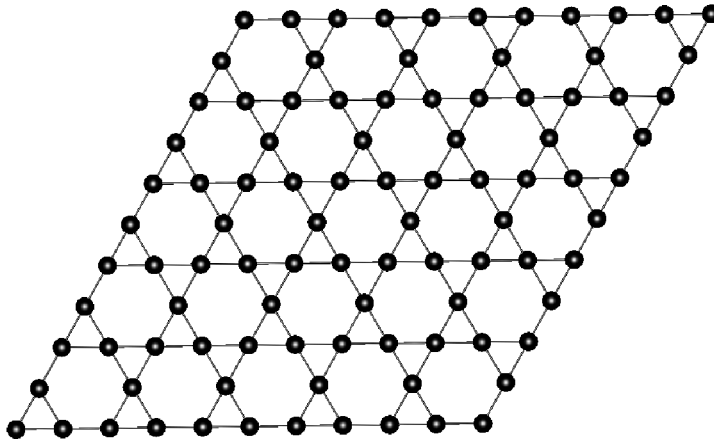


Figure 1.1: Schematic showing a 2D kagome lattice, made by removing sites at the center of each empty hexagon from the triangular lattice.

There are several 3D versions of the triangular lattice which can often be characterized simply by the stacking sequence of triangular layers [3]. The simple hexagonal lattice has AA stacking where exchange coupling between planes differs from that within the triangular plane due to the spacing between layers. Depending on the distance between layers, such AFs are described as being quasi-2D with six in-plane NN, or quasi-1D with two NN between planes. Antiferromagnets with hexagonal close-packed AB stacking of triangular layers also exist, with twelve NN. In the non-close-packed structures, the distance between layers is arbitrary and the symmetry changes from hexagonal to rhombohedral. Similarly, ABC stacked triangular layers can be realized with arbitrary spacing, or in a close-packed con-

figuration. The latter structure also describes the fcc lattice with twelve NN. The fcc AF has been studied over many decades and exhibits a large variety of types of magnetic order [4],[5].

The basic 2D kagome lattice can also be stacked in a variety of ways to form 3D crystal structures, as discussed in Sec. 1.2.2. ABC stacked kagome layers in a close-packed configuration form the fcc kagome lattice with eight NN, the most popular realization being  $\text{AuCu}_3$  and the most popular AF being  $\text{IrMn}_3$ , this structure having the crystal symmetry space group No. 221,  $\text{Pm}\bar{3}\text{m}$ . There have been a large number of publications on  $\text{IrMn}_3$  over the past few decades that mostly appear in journals focused on applied physics [6]. This is the material of choice for the so-called “Pinned Layer” in the spin valve structure used in hard drives [7], as seen in Fig. 1.2. The magnetic order was identified some time ago and is based on the  $120^\circ$  spin structure around each triangle. In all the published works on  $\text{IrMn}_3$  and sister AFs, there is no mention of “kagome” despite the fact it is a true realization of a 3D kagome structure, with 8 NN in 3D. In these publications, the 3D spin structure is called “T1” magnetic order. Correspondingly, none of the work published on the magnetic order in kagome lattices made the connection to the  $\text{IrMn}_3$ -class of compounds.

Exchange pinning, where the magnetization of a ferromagnetic layer is pinned to a certain direction, is crucial to the operation of a spin valve, which is based on the magnetoresistive response of the device. Due to spin-dependent electron scattering, the resistance of the spin-valve is dependent on the relative orientation of the two ferromagnetic thin-film layers shown in Fig. 1.2. In one of the layers, the “Free Layer”, the magnetization rotates in response to an external magnetic field (e.g., from a passing bit on a hard-drive disk). In the other layer, the Pinned

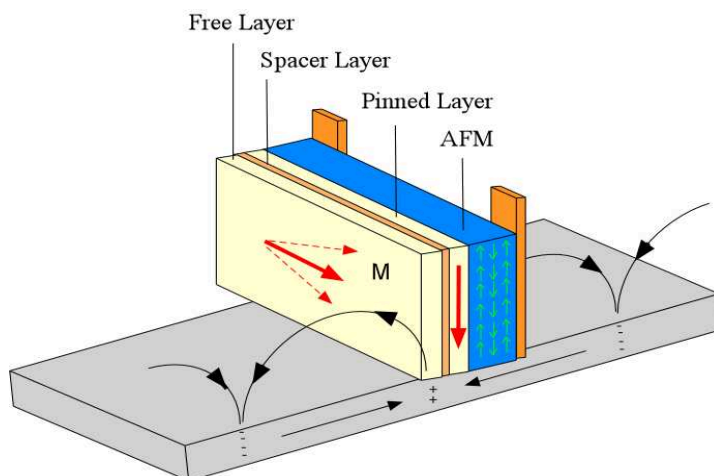


Figure 1.2: Schematic of a read-head structure.

Layer, the magnetic moments are pinned in a fixed direction through coupling to an adjacent AF. For the past decade, thin films of  $\text{IrMn}_3$  have been the most popular AF for this purpose.

Agreement on the fundamental mechanism responsible for exchange bias, the shift in the magnetization curve of the ferromagnet due to the AF, in Ir-Mn thin films and other materials remains elusive [8]. It is believed that frustration of some sort at the interface between the antiferromagnet and ferromagnet is essential [9]. It is clear that there needs to be a pinned ferromagnetic component within the first few layers of the AF. Some studies also suggest that exchange bias is enhanced if this component is perpendicular to the plane of the film [10],[11]. An essential requirement for technological applications is that the AF layer magnetically orders well above room temperature. A preliminary Monte Carlo (MC) study of the fundamental spin structures and spin degeneracy of the 3D fcc kagome lattice was performed by a previous graduate student (V. Hemmati) in our group [12]. Only NN exchange interactions were included, with cubic anisotropy omitted. A summary of the results of that study is presented below.

The work in this thesis represents a significant extension of this first investigation. There are two main focuses: MC simulations to explore the impact of cubic anisotropy and a theoretical and experimental study of spin excitations. The MC simulation results were published in an article [13] in Phys. Rev. B and represent the main contents of Chap. 3. The spin excitations results along with some preliminary neutron scattering theory were published in another Phys. Rev. B article [14] and are presented in Chaps. 4 and 5.

## 1.2 Kagome Lattice

### 1.2.1 2D Kagome Lattice

The macroscopic degeneracy associated with magnetic dipoles on the 2D kagome lattice (Fig. 1.1 and Fig. 1.3) composed of corner-sharing triangles, with four NN exchange interactions, continues to generate new physics after twenty years of study [15],[16]. The main focus of these works has been associated with ultralow temperature and quantum effects. Quasi-3D experimental manifestations have been limited to systems with weakly coupled kagome layers or distorted hyperkagome lattice structures [17],[18].

For continuous spin models on the 2D kagome lattice with NN exchange interactions, the ground state is highly degenerate with the only requirement being a net zero magnetic moment for each triangle. This gives rise to many degenerate configurations having an overall  $120^\circ$  spin structure in either  $q = 0$  or  $\sqrt{3} \times \sqrt{3}$  co-planar forms [15] (see Fig. 1.3), the names referring to their ordering wave vector. The  $120^\circ$  spin structure can be thought of as three interpenetrating ferromagnetic sublattices. In addition to the usual continuous degrees of freedom

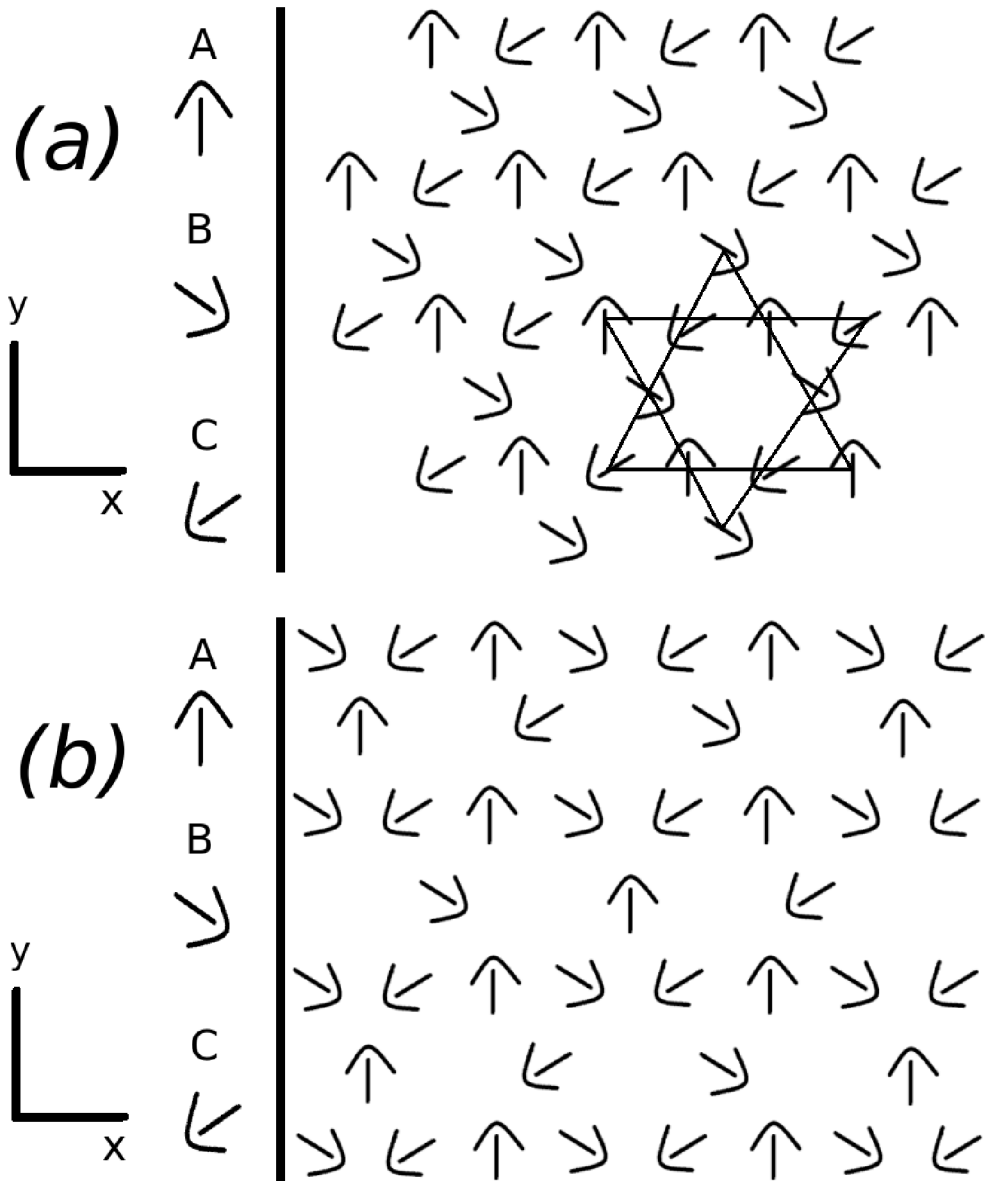


Figure 1.3: Schematic showing a 2D kagome lattice a)  $q = 0$  and b)  $\sqrt{3} \times \sqrt{3}$   $120^\circ$  structures. Three sublattices  $A$ ,  $B$ , and  $C$  are shown that make up the spins of the lattice, each making  $120^\circ$  angles with its neighbor spins. The  $z$  axis is outside the plane, along the  $[111]$  cubic direction when used to describe the 3D kagome lattice. A kagome structure is highlighted for the  $q = 0$  case using lines.

associated with  $XY$  and Heisenberg models, the  $q = 0$  spin structure on the 2D kagome lattice allows for the interchange of each sublattice spin with its neighbor

along a row with no change in energy. Unlike the triangular lattice AF, there is no correlation between chiralities, used to further characterize the spin order, of adjacent triangles [19]. The macroscopic degeneracy found in the 2D kagome lattice and similar systems such as spin ice materials [20],[21], where the correlated but disordered ground state has the local magnetization obeying ice rules leaving a residual entropy, can often be lifted by thermal or quantum fluctuations through the mechanism of order-by-disorder in which states are selected from the ground state manifold by entropic forces [22],[23]. The degeneracy can also be lifted with the addition of further neighbor interactions or magnetic anisotropies [24],[25].

Classical Heisenberg MC simulations found that low temperature ( $T \approx 10^{-4} - 10^{-1}J$ , with  $J$  the strength of the exchange interaction) 2D Heisenberg kagome models exhibit three separate states: a coplanar, a cooperative paramagnetic and a paramagnetic state seen in the specific heat  $C$  [17].  $C$  saturates at the value of  $11/12$  when the data is extrapolated to  $T = 0$ . Further analysis at even lower temperatures ( $T \approx 10^{-6}J$ ) show that the  $\sqrt{3} \times \sqrt{3}$  structure is maintained [16],[26].

For the 2D  $q = 0$  kagome lattice, a spin wave analysis [15] found that when there are only nearest neighbor interactions  $J_1$ , three spin wave modes emerged, one of which being a zero-frequency mode for all wavevectors  $\mathbf{k}$  and the other two modes being degenerate linear modes. The zero-frequency dispersionless mode allows the formation of local zero-energy modes corresponding to changing spin orientations of select spins in a local area without affecting the total energy.

By adding second and third nearest neighbor interactions  $J_2$  and  $J_3$ , the modes change according to the relationship between  $J_2$  and  $J_3$ .  $J_2 > J_3$  gives three non-degenerate modes,  $J_2 = J_3$  gives the same result as only having nearest neighbors and  $J_2 < J_3$  gives complex frequencies showing that  $q = 0$  is not stable in this

case. A similar analysis was performed on the  $\sqrt{3} \times \sqrt{3}$  lattice where zero-energy stable modes were also found.

Other studies on the addition of next NN [27] interactions show that having even a very small  $J_2$  (positive or negative) enables a finite-temperature phase transition.

### 1.2.2 3D Kagome Lattice

In the 3D fcc kagome case (see Fig. 1.4), only the  $q = 0$  structure is selected and two of the three sublattice spins within a plane defined by the eight NN exchange interactions can be reoriented with no cost in energy [12],[14]. As described in Chap. 3, much of the degeneracy in 2D carries over into 3D.

Interest in the fcc kagome lattice has been driven not only by it being a unique realization of this type of frustration in three dimensions but also due to its connection with magnetic thin-film technology through  $\text{IrMn}_3$ , which is commonly used as the AF exchange pinning layer in spin valves [28],[29] for magnetic recording.  $\text{IrMn}_3$  also serves as a candidate for observing the anomalous Hall effect in zero magnetic field [30],[31],[32]. It, and sister compounds  $\text{RhMn}_3$  and  $\text{PtMn}_3$ , have the fcc  $\text{CuAu}_3$  crystal structure [33],[34],[35],[36], where, in the ordered phase, magnetic Mn (manganese) ions reside on the cube faces and the nonmagnetic Ir (iridium) ions sit at the cube corners. The magnetic ions can thus be viewed as being on ABC stacked (111) kagome planes, where each site has eight NNs (four in-plane, two to the plane above, and two to the plane below) as shown in Fig. 1.4. Bulk  $\text{IrMn}_3$  was shown experimentally to have long-range magnetic order below a Néel temperature of  $T_N \simeq 960$  K [6], referred to as the “T1” structure, which is the 3D manifestation of the  $120^\circ$   $q = 0$  spin structure [12]. Similar magnetic order is

also observed in  $\text{RhMn}_3$  and  $\text{PtMn}_3$ . In thin-film applications, the  $[111]$  direction is perpendicular to the film plane. It is of interest to note that the 3D  $q = 0$  structure remains favored in the presence of 6 ferromagnetic second-NN exchange interactions, 16 AF third-NN exchange and 12 ferromagnetic fourth-NN exchange interactions, as calculated for  $\text{IrMn}_3$  [37] using density functional theory. These next NN exchange interactions strengths are calculated and also given as being as strong as 25% of the strength of the NN interactions, which are speculated to play a minor role in spin wave theory, though they are not considered in the present work.

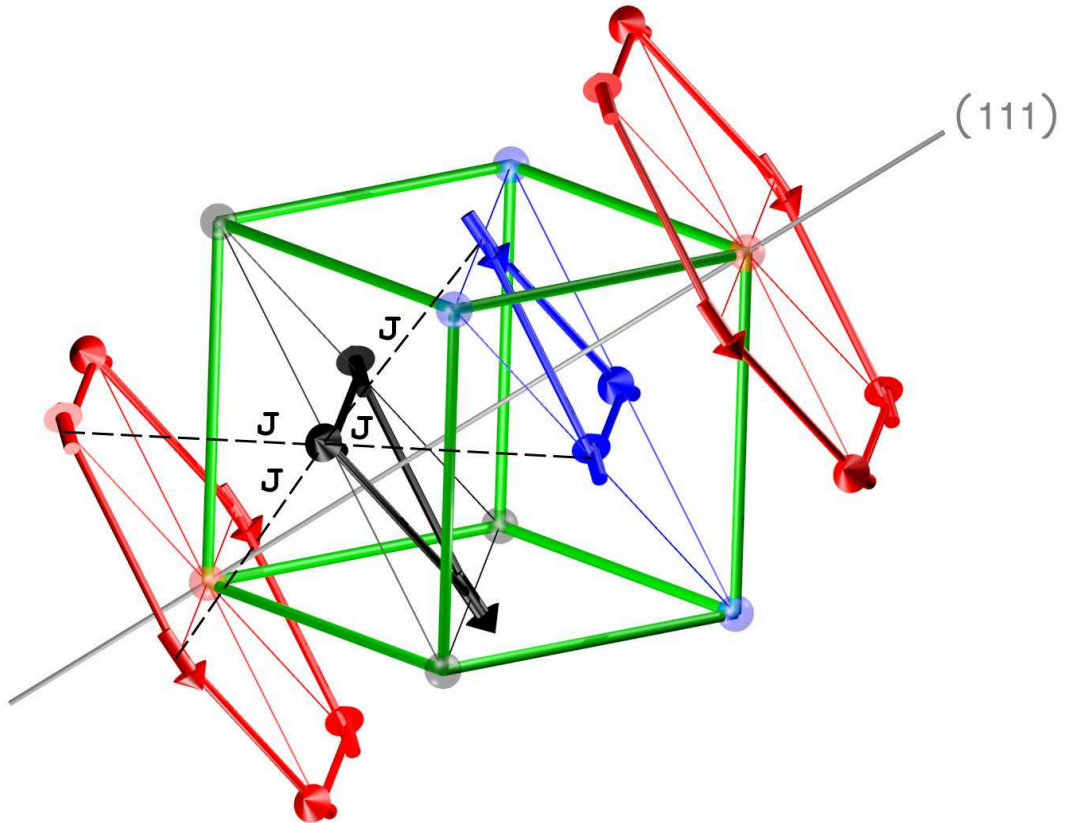


Figure 1.4: The fcc kagome lattice with magnetic Mn ions on cube faces forming stacked 2D kagome layers along the  $(111)$  axis. Nonmagnetic Ir ions are at the corners. The four interlayer exchange interactions ( $J$ ) are indicated [13].

## 1.3 Outline of the Thesis

This chapter provided an overview on the motivation behind this study.

Chap. 2 describes the theoretical, computational and experimental techniques used in this study of  $\text{IrMn}_3$ . MC methods are reviewed along with how they are used to study the fcc kagome lattice. An introduction to neutron scattering, used in later chapters, is also given.

Chap. 3 reviews previous MC simulation results on the fcc kagome lattice using pure (no anisotropy) Heisenberg and XY models. New MC simulations where cubic anisotropy is added to the NN Heisenberg fcc AF kagome lattice comprises the main focus of this chapter. An analytic calculation of the ground state reveals an out-of-plane rotation of the sublattice spins driven by the anisotropy as well as a concomitant net magnetic moment perpendicular to the plane. The effect of anisotropy in removing certain degeneracies is determined. The impact of anisotropy on the Néel temperature  $T_N$  and various thermodynamic properties is studied. In addition, results from energy histograms and fourth-order Binder energy cumulants [38] are used to argue that the transition changes from discontinuous to continuous as a consequence of anisotropy reducing spin degeneracies. Chap. 3 is based on Ref. [13].

Chap. 4, partially based on Ref. [14], describes a theory for elastic neutron scattering of  $\text{IrMn}_3$  through analysis of the fcc kagome lattice. An analysis of the nuclear and magnetic scattering cross sections is included to study the effects of adding anisotropy to the model, with theoretical results being derived.

Chap. 5, based heavily on Ref. [14], focuses on neutron scattering of  $\text{IrMn}_3$  through analysis of the fcc kagome lattice. A linear spin wave approach is described that includes the effect of cubic anisotropy. Also considered is the impact of

having a coupling strength between kagome lattices different from the one within the planes (rhombohedral symmetry). Spin wave modes  $\omega(k)$  are plotted along with the intensity for elastic and inelastic scattering, relevant for the single-crystal case. Experimental neutron scattering intensity results on powdered  $\text{IrMn}_3$  are also presented and matching theory to these experiments performed at Oak Ridge National Laboratory (ORNL) is attempted. Discrepancies are noted and possible explanations are presented.

A discussion on the results and conclusions drawn from them is presented in Chap. 6. Possibilities for future work are also suggested. Finally, an appendix that expands on deriving the fundamentals of magnetic neutron scattering and shows supplementary calculations and data is located in Appendix A.

# Chapter 2

## Introduction: Techniques

### 2.1 Monte Carlo Methods

#### 2.1.1 Introduction to Monte Carlo

The Monte Carlo (MC) method can provide an accurate solution to many types of problems using a very simple process that relies on random numbers. It is used to solve a wide variety of problems and done correctly can be an efficient tool, with applications such calculating integrals or performing simulations. In statistical mechanics applications, the internal energy and other thermodynamic properties of a system can be calculated using MC techniques with minimal programming effort.

#### 2.1.2 Principles of Monte Carlo

In the Boltzmann distribution, which gives the probability of a system being in a certain microstate based on the system energy and temperature, a system at equilibrium is in a state  $a$  with probability

$$p_a = \frac{1}{Z} e^{-\beta E_a}, \quad (2.1)$$

where  $\beta = \frac{1}{kT}$  with  $k$  the Boltzmann constant ( $1.38 \times 10^{-23} JK^{-1}$ ),  $T$  the temperature,  $E_a$  is the internal energy for the state  $a$ , and  $Z$  is the partition function

$$Z = \sum_a e^{-\beta E_a}. \quad (2.2)$$

In Monte Carlo simulations an algorithm is used that generates a set of random states with the probability given by the Boltzmann distribution. The algorithm takes some initial set of states from which a Markov chain, where a new state can be obtained randomly from a current state without access to all the previous states, is generated with the transition probability between successive states  $a \rightarrow b$  given by  $P(a, b)$ . This probability is made to satisfy ergodicity and detailed balance to get a good algorithm. The number of steps in the Markov chain required to equilibrate some set of initial states depends on a number of factors and while difficult to determine initially can be validated with some measure of confidence afterwards.

Ergodicity requires that any state of a system must be accessible from any other state given enough simulation time. There must be a path from any state  $a$  to any other state  $b$ , and conversely one from state  $b$  to state  $a$ .

Detailed balance is best described by an equation

$$\frac{P(a, b)}{P(b, a)} = \frac{p_b}{p_a}, \quad (2.3)$$

where  $P(a, b)$  ( $P(b, a)$ ) is the probability that the system will transition to state  $b$  ( $a$ ) from state  $a$  ( $b$ ), and the  $p_a$  and  $p_b$  are the probabilities of occupation at

equilibrium. The transition probability  $P(a, b)$  involves the selection probability (probability that the algorithm generates a state  $b$  from state  $a$ ) and the acceptance ratio (probability that the system changes from state  $a$  to state  $b$ ). When following the Boltzmann distribution,  $p_a$  and  $p_b$  are known and Eq. 2.3 becomes

$$\frac{P(a, b)}{P(b, a)} = e^{-\beta(\Delta E)}, \quad (2.4)$$

where  $\Delta E \equiv E_b - E_a$ .

### 2.1.3 Metropolis Algorithm

As detailed balance does not dictate the transition probability  $P(a, b)$  needed, the choice of algorithm remains, so long as it satisfies ergodicity and detailed balance. Due to its simplicity and efficiency, the Metropolis-Hastings algorithm is the most popular algorithm, and is the one used here. It has single-spin flip dynamics, only considering a single spin at a time.

This algorithm can be summarized as

1. Calculate the energy of the system.
2. Pick a random spin on the lattice.
3. Calculate the energy if the spin is flipped and  $\Delta E$ , the difference in energy between this energy and the previous one.
4. If  $\Delta E \leq 0$ , the spin is flipped. Otherwise, the next step is followed.
5. Calculate the Boltzmann weight,  $w = e^{-\beta\Delta E}$ .
6. Generate a random number  $0 \leq r < 1$ .

7. If  $r < w$ , flip the spin. If not, no change is made.

A Metropolis MC step (MCS) is defined as one sweep of the lattice with the Metropolis algorithm, picking as many random spins as there are sites in the lattice. The total energy of the system can either be calculated every single step, or calculated initially and updated iteratively. This can be applied to other quantities of interest, such as the order parameter and the magnetization. As such, the process of flipping (or not) a single spin can be made to be computationally efficient. This is very important since, due to the quantity of spins considered, the application of the algorithm can quickly become a bottleneck in simulations at large system sizes which reveal information relevant to the thermodynamic limit (infinite system size).

#### 2.1.4 Thermodynamic Quantities

The fundamental thermodynamic quantities calculated for magnetic lattices in this work are defined below. The energy associated with nearest-neighbor interactions is (where scalar  $S_i$  spins are used for simplicity)

$$E_J = -J \sum_{\langle ij \rangle} S_i S_j, \quad (2.5)$$

with  $J$  the exchange interaction strength, either positive for a ferromagnet or negative for an antiferromagnet. A representative order parameter (magnetization) per spin is defined through

$$M(T) = \frac{1}{N} \left\langle \left| \sum_i S_i \right| \right\rangle, \quad (2.6)$$

where  $i$  is summed over all  $N$  lattice sites. For  $\text{IrMn}_3$ , this definition is modified, as seen in Chap. 3. In addition, the magnetic susceptibility per spin is calculated using:

$$\chi(T) = \beta N (\langle M(T)^2 \rangle - \langle M(T) \rangle^2), \quad (2.7)$$

where  $\beta = 1/kT$  and the specific heat per spin is given by

$$C(T) = \frac{\beta^2}{N} (\langle E(T)^2 \rangle - \langle E(T) \rangle^2). \quad (2.8)$$

In simulations, we define units such that  $k \equiv 1$  to simplify calculations.

### 2.1.5 First-Order vs Continuous Phase Transitions

When going from one state (phase) to another, a system undergoes a phase transition. These transitions can be seen in everyday life, such as ice melting into water. For phases that depend on temperature,  $T_C$  is defined as the critical temperature (Curie temperature) where this transition occurs. In magnetic systems, a well studied phase transition is a ferromagnet, becoming paramagnetic and losing its magnetism as the temperature is raised. In an antiferromagnet (AF), the phase transition temperature is denoted as the Néel temperature  $T_N$  instead.

These phase transitions are separated into two different types, first-order and continuous (or second and higher order). A first-order transition, such as ice melting, involves a latent heat where the system absorbs or releases energy at a constant temperature. Furthermore, there is a discontinuity in the first derivative of the energy versus thermodynamic variables such as  $T$ . A continuous transition, such as a ferromagnet losing its magnetism, does not have a discontinuity in the first derivative of the energy (as the name implies) but rather in the second derivative.

For many systems studied with MC techniques, it is not always straightforward to determine if a phase transition is first-order or continuous. In simulations, there is often enough inaccuracies due to simulated systems having finite sizes and a limited simulation time that does not allow determining the order of the transition simply by calculating the energy derivatives. Finite-size scaling methods can be employed in these cases. Two such methods were used in this thesis and in the previous work [12] on the fcc kagome lattice.

One common method used for studying the order of a phase transition involves Binder fourth-order cumulants [38]. These can be defined for the energy as

$$U_E = 1 - \frac{\langle E^4 \rangle}{3\langle E^2 \rangle^2}, \quad (2.9)$$

with a similar expression for the magnetization cumulant. While  $U_E$  is strictly a theoretical construct, it shows different behaviors for first-order and continuous phase transitions. From the theory of thermodynamic fluctuations, the energy  $E$  can be described by a probability distribution function  $P_N(E)$  that is approximated by a Gaussian and depends on the number of spins  $N$ . In a first-order transition, due to the defining discontinuity in the derivative of the energy,  $P_N(E)$  consists of a superposition of two Gaussians. Far from  $T_C$ ,  $P_N(E)$  in a first-order transition can be described by a single Gaussian such that for both first-order and continuous transitions,  $U_E \rightarrow \frac{2}{3}$  in the thermodynamic limit of  $N \rightarrow \infty$ . Around  $T_C$ ,  $U_E$  remains at  $\frac{2}{3}$  in the thermodynamic limit for a continuous transition, but  $U_E$  for first-order transitions is different. As simulations are done for a finite lattice size, the value of the cumulants around  $T_C$  are not at their limit values and extrapolation to large  $N$  must be used.

To use the cumulants,  $U_E$  is calculated at temperatures near  $T_C$ . It exhibits a

minimum near  $T_C$  that depends on the lattice size. By calculating  $U_E$  for different values of  $N$  near  $T_C$ , the minimum of  $U_E$  vs  $N$  can be obtained. Plotting this minimum against  $1/N$  and extrapolating towards  $1/N \rightarrow 0$  gives an indication of the order of the transition. In a continuous phase transition, it will extrapolate to  $\frac{2}{3}$  [39].

Using the same theory, another technique involves calculating energy histograms at several temperatures very close to the critical temperature. As the system traverses the critical temperature, indications of discontinuity are revealed by multiple energy peaks (two phases) if the transition is first-order. If the transition is continuous, there will only be a single peak observed that evolves smoothly as the temperature changes around  $T_C$  [40].

## 2.2 Neutron Scattering and Spin Waves

### 2.2.1 Motivation

Whereas MC simulations can provide some important insight into the thermodynamic behavior of the 3D fcc kagome lattice, it is useful to study other experimental methods that compliment these results. Magnetic elastic neutron scattering can be used to determine the magnetic structures, and inelastic scattering is used to study spin excitations of the equilibrium magnetic order.

A previous study by Tomeno *et al.* [6] reported on an elastic magnetic neutron scattering experiment on a single crystal of ordered  $\text{IrMn}_3$  that established the  $q = 0$  kagome spin structure. By observing the (100) peak over a wide range of temperatures, the Néel temperature was estimated to be  $T_N = 960 \pm 10$  K. A determination of the lattice parameter  $a$  was also possible by analysis of the

peak locations. In their study, the authors noted that the scattering results might have had a small but significant influence from the presence of disordered phases of  $\text{IrMn}_3$ . This disordered form of  $\text{IrMn}_3$  allows the Ir and Mn ions to randomly switch position, thus giving an overall fcc lattice structure to the Mn-ion positions. Both the ordered and the disordered phases have been studied in more detail in thin-film form [41]. Furthermore, the temperature range studied by Tomeno *et al.* did not go below 250 K.

This opened up the possibility of further neutron scattering studies, including inelastic neutron scattering, going to lower temperatures, and to study any impact of magnetic anisotropy. Experimental results were obtained through a week-long visit and collaboration with ORNL in Oak Ridge, Tennessee in May 2012. There, inelastic studies on  $\text{IrMn}_3$ , with powdered samples provided in collaboration with other research groups at ORNL, were performed at temperatures from about 5K up to room temperature. The inelastic intensity data could also be integrated to give elastic peaks. Further details of the experiment are given in Chap. 5 where the analysis of the data and a corresponding theory are presented.

### 2.2.2 Spin Wave Theory

In condensed matter physics, a quantity of great interest is the dispersion relation giving frequency versus wavenumber,  $\omega(k)$ , which describes how waves propagate through a medium and the effects of dispersion. It can often be a challenge to obtain  $\omega(k)$  and its derivation can differ considerably from one material to another. Once it is known, an important application is in inelastic magnetic scattering. As such, calculating  $\omega(k)$  for the fcc kagome lattice is the focus of Chap. 5, where the effect of cubic anisotropy is included.

In magnetic materials, spin waves describe excitations about the equilibrium magnetic order and can be characterized with the dispersion relation. An equivalent description of the magnetic lattice disturbances is through magnons, quasiparticles that quantize spin waves. In Chap. 5, the goal is to find the spin dispersion relation  $\omega(k)$  for the 3D fcc kagome lattice. A number of theories can be utilized, either classical or quantum, but as  $S = 5/2$  for the magnetic manganese atoms in  $\text{IrMn}_3$ , quantum effects are negligible and a classical theory is likely sufficient. Furthermore, for large  $S$  and small temperatures (typically well below the critical temperature), a linear spin wave theory can be applied that provides additional theoretical simplifications.

### An Example Spin Wave Calculation

An example of classical linear spin theory, for a simple 1D antiferromagnet, is given here [42]. The spin wave theory used for the fcc kagome lattice described in Chaps. 4-5 follows the basic method described below.

For  $N$  spins  $\mathbf{S}_p$  of magnitude  $S = 1$  in one dimension, coupled with an antiferromagnetic exchange interaction conventionally chosen such that  $J > 0$ , the Heisenberg Hamiltonian is given as

$$\mathcal{H} = J \sum_{p=1}^N \mathbf{S}_p \cdot \mathbf{S}_{p+1}. \quad (2.10)$$

Each nearest neighbor (NN) spin  $p$  will have a term of the form

$$J\mathbf{S}_p \cdot (\mathbf{S}_{p-1} + \mathbf{S}_{p+1}). \quad (2.11)$$

From the magnetic torque equation, the time derivative of the angular momen-

tum  $\hbar\mathbf{S}_p$  is equal to the torque (cross product of the magnetic moment with the magnetic field) which acts on the spin. This then gives

$$\frac{d\mathbf{S}_p}{dt} = \frac{-J}{\hbar}(\mathbf{S}_p \times \mathbf{S}_{p-1} + \mathbf{S}_p \times \mathbf{S}_{p+1}). \quad (2.12)$$

At equilibrium, all the spins point along a single axis (defined here to be  $\mathbf{z}$ ), alternating in direction along the chain. In the linear approximation, only transverse excitations occur with  $S_p^z = S$  such that  $\frac{dS_p^z}{dt} = 0$ . Thus, two equations for  $x$  and  $y$  remain. For an antiferromagnet, half the spins can be divided in one sublattice  $A$  with  $S_{2p}^z = S \equiv 1$  in equilibrium, and the other half into another sublattice  $B$  with  $S_{2p+1}^z = -S \equiv -1$ .

For sublattice  $A$  spins, Eq. 2.12 becomes

$$\frac{dS_{2p}^x}{dt} = -(J/\hbar)(-2S_{2p}^y - S_{2p-1}^y - S_{2p+1}^y), \quad (2.13)$$

$$\frac{dS_{2p}^y}{dt} = (J/\hbar)(-2S_{2p}^x - S_{2p-1}^x - S_{2p+1}^x). \quad (2.14)$$

For sublattice  $B$  spins, Eq. 2.12 becomes

$$\frac{dS_{2p+1}^x}{dt} = -(J/\hbar)(2S_{2p+1}^y + S_{2p}^y + S_{2p+2}^y), \quad (2.15)$$

$$\frac{dS_{2p+1}^y}{dt} = (J/\hbar)(2S_{2p+1}^x + S_{2p}^x + S_{2p+2}^x). \quad (2.16)$$

From these,  $S^+ = S^x + iS^y$  can be used so that

$$\frac{dS_{2p}^+}{dt} = -(iJ/\hbar)(2S_{2p}^+ + S_{2p-1}^+ + S_{2p+1}^+), \quad (2.17)$$

$$\frac{dS_{2p+1}^+}{dt} = (iJ/\hbar)(2S_{2p+1}^+ + S_{2p}^+ - S_{2p+2}^+). \quad (2.18)$$

Defining  $\omega_c = 2J/\hbar$  and looking for solutions of the type  $S_{2p}^+ = ue^{i(2pka-\omega t)}$  and  $S_{2p+1}^+ = ve^{i(2(p+1)ka-\omega t)}$ , with  $p$  a position variable, gives

$$\omega u = \frac{1}{2}\omega_c(2u + ve^{-i(ka)} + ve^{i(ka)}), \quad (2.19)$$

$$-\omega v = \frac{1}{2}\omega_c(2v + ue^{-i(ka)} + ue^{i(ka)}). \quad (2.20)$$

To determine  $\omega$ , the coefficient matrix  $C$  of  $u$  and  $v$  is obtained

$$C = \begin{pmatrix} \omega_c - \omega & \omega_c \cos(ka) \\ \omega_c \cos(ka) & \omega_c + \omega \end{pmatrix}, \quad (2.21)$$

with the solution to the secular equation giving

$$\omega = \omega_c |\sin(ka)|. \quad (2.22)$$

Note that  $\omega \sim k$  for small wave vectors and that this classical derivation reproduces results obtained using quantum techniques (such as Holstein-Primakov [43]) in the large  $S$  limit.

### 2.2.3 Magnetic Neutron Scattering

Magnetic neutron scattering gives two separate but related types of information. Inelastic scattering measures neutrons that change energy after colliding with a material, while in elastic scattering there is no change in energy of the incident neutron. By analyzing how the neutrons interact with the sample, it is possible

to study the intensity as a function of  $\mathbf{k}$  in reciprocal space. Due to the lattice configuration, different refractions will occur that can be measured for certain wavevectors  $\mathbf{k}$ . It is then possible to calculate the relative intensity for different  $\mathbf{k}$  and thus compare with experiments.

Another important factor when looking at magnetic neutron scattering is single crystals compared to powder samples. Single crystals, which can be theorized as an infinite lattice structure, are highly desirable but not always possible to synthesize easily. Often, powder samples, where the material is essentially ground up and made of many smaller crystals, are used and powder diffraction is necessary. A theoretical analysis that examines these samples is constructed for a single crystal before doing a powder average.

## Elastic Scattering

For elastic scattering, it is important to identify the differential cross section which is related to the count of neutrons scattered into a solid angle  $d\Omega$  in the direction  $\theta, \phi$ . This quantity,  $\frac{d\sigma}{d\Omega}$ , once found gives all the information necessary to know how neutrons are scattered. In turn, the location in wavevector space and relative intensity of peaks are obtained. The cross section used in elastic magnetic scattering is derived in Appendix A and can be written as [44]

$$\frac{d\sigma}{d\Omega} = r_0^2 \sum_{l'} e^{i\boldsymbol{\kappa} \cdot (\mathbf{l} - \mathbf{l}')} \left| \sum_d e^{i\boldsymbol{\kappa} \cdot \mathbf{d}} e^{-W_d(\boldsymbol{\kappa})} \frac{1}{2} g_d \langle S_d \rangle F_d(\boldsymbol{\kappa}) \left[ \hat{\boldsymbol{\kappa}} \times \left( \hat{\mathbf{S}}_d(\boldsymbol{\kappa}) \times \hat{\boldsymbol{\kappa}} \right) \right] \right|^2. \quad (2.23)$$

Each term is defined in Appendix A.2, but important ones are the scattering vector  $\boldsymbol{\kappa} = \mathbf{k} - \mathbf{k}'$ , the form factor  $F_d(\boldsymbol{\kappa})$ , the index  $d$  of the ion at position  $\mathbf{d}$  within the unit cell, and the spin vector  $\mathbf{S}$ . For a simple ferromagnet with a Bravais lattice,

the sum over  $d$  only has one term,  $\mathbf{d} = \mathbf{0}$ . Note that for a single domain of spins,

$$\left| \sum_d \hat{\boldsymbol{\kappa}} \times \left( \hat{\mathbf{S}}_d(\boldsymbol{\kappa}) \times \hat{\boldsymbol{\kappa}} \right) \right|^2 = 1 - (\hat{\mathbf{S}} \cdot \hat{\boldsymbol{\kappa}})^2. \quad (2.24)$$

$\hat{\mathbf{S}}$  can also be written as  $\hat{\boldsymbol{\eta}}$  (direction of the domain). When  $\boldsymbol{\kappa} = \boldsymbol{\tau}$  (reciprocal lattice vector),  $1 - (\hat{\mathbf{S}} \cdot \hat{\boldsymbol{\kappa}})^2 = 1 - (\hat{\boldsymbol{\tau}} \cdot \hat{\boldsymbol{\eta}})^2$ . If there are multiple domains for a ferromagnet, each with its own orientation, an average over the various orientations is taken. If  $\hat{\boldsymbol{\eta}}$  has an equal probability to be in any direction, or if it is equally likely to be along axes related by cubic symmetry, then  $1 - (\hat{\boldsymbol{\tau}} \cdot \hat{\boldsymbol{\eta}})_{\text{av}}^2 = \frac{2}{3}$ .

An example for a simple AF is given here [45]. In this case, all the spins of the unit cell are parallel or antiparallel to a single direction  $\hat{\boldsymbol{\eta}}$  within a domain.

For the AF, there can also be multiple domains and an average over  $1 - (\hat{\boldsymbol{\tau}} \cdot \hat{\boldsymbol{\eta}})_{\text{av}}^2$  can be used, which does not affect peak locations in  $\mathbf{k}$  space. The spin is described as either pointing along  $+\hat{\boldsymbol{\eta}}$  or  $-\hat{\boldsymbol{\eta}}$ , so an Ising-like variable  $\sigma_d = +1$  or  $-1$  is introduced into  $\mathbf{S}_d$  to take this into account. Then, from Eq. 2.23 one finds that

$$\frac{d\sigma}{d\Omega} = r_0^2 N \frac{(2\pi)^3}{\nu_0} \sum_{\boldsymbol{\tau}} \delta(\boldsymbol{\kappa} - \boldsymbol{\tau}) \left| \sum_d \sigma_d e^{i\boldsymbol{\tau} \cdot \mathbf{d}} e^{-W_d(\boldsymbol{\tau})} \frac{1}{2} g_d \langle S_d \rangle F_d(\boldsymbol{\tau}) \right|^2 [1 - (\hat{\boldsymbol{\tau}} \cdot \hat{\boldsymbol{\eta}})_{\text{av}}^2]. \quad (2.25)$$

For the simplest AF, there is only one type of ion  $d$  with the only variation between sites being  $\sigma_d$ . In such cases, the magnetic unit cell is larger than the chemical unit cell due to the greater diversity in sites. The cross section can be put in the following form

$$\frac{d\sigma}{d\Omega} = r_0^2 N \frac{(2\pi)^3}{\nu_0} \sum_{\boldsymbol{\tau}} \delta(\boldsymbol{\kappa} - \boldsymbol{\tau}) e^{-2W(\boldsymbol{\tau})} |F_M(\boldsymbol{\tau})|^2 [1 - (\hat{\boldsymbol{\tau}} \cdot \hat{\boldsymbol{\eta}})_{\text{av}}^2], \quad (2.26)$$

with

$$F_M(\boldsymbol{\tau}) = \sum_d \sigma_d e^{i\boldsymbol{\tau}\cdot\mathbf{d}} \frac{1}{2} g_d \langle S_d \rangle F_d(\boldsymbol{\tau}) = \frac{1}{2} g \langle S \rangle F(\boldsymbol{\tau}) \sum_d \sigma_d e^{i\boldsymbol{\tau}\cdot\mathbf{d}}. \quad (2.27)$$

As such, due to the delta function, peaks are located at  $\boldsymbol{\kappa} = \boldsymbol{\tau}$ , for  $\boldsymbol{\tau}$  corresponding to the reciprocal lattice vectors for the magnetic lattice (often simple cubic with a basis); however, the sum over  $d$  in  $F_M(\boldsymbol{\tau})$  can still cancel peaks.

As a specific example, MnTe<sub>2</sub> is reproduced here [44]. The unit cell is fcc for Mn atoms, spins having twelve NN. Looking at an fcc cube, four sides on a horizontal plane have spins pointing in the opposite direction of the other eight spins. Treating the cell as simple cubic with a basis, the four sites of the unit cell are given by (direction given by “up” or “down” to indicate whether spins are parallel or antiparallel to the spin direction that lies unspecified in the (001) planes)

$$\begin{aligned} \mathbf{d}_1 &= a(0, 0, 0) \text{ up,} \\ \mathbf{d}_2 &= a\left(\frac{1}{2}, \frac{1}{2}, 0\right) \text{ up,} \\ \mathbf{d}_3 &= a\left(\frac{1}{2}, 0, \frac{1}{2}\right) \text{ down,} \\ \mathbf{d}_4 &= a\left(0, \frac{1}{2}, \frac{1}{2}\right) \text{ down.} \end{aligned} \quad (2.28)$$

The simple cubic values  $\boldsymbol{\tau}$  are given by  $\boldsymbol{\tau} = \frac{2\pi}{a}(t_1, t_2, t_3)$  for  $t_i$  any integer. The

interesting part of the structure factor  $F_M(\boldsymbol{\tau})$  concerns the sum over  $\mathbf{d}$ . Indeed,

$$\begin{aligned} \sum_d \sigma_d e^{i\boldsymbol{\tau} \cdot \mathbf{d}} &= (+1) + (+1)e^{i\frac{2\pi}{a}(t_1, t_2, t_3) \cdot a(\frac{1}{2}, \frac{1}{2}, 0)} + \\ &\quad (-1)e^{i\frac{2\pi}{a}(t_1, t_2, t_3) \cdot a(\frac{1}{2}, 0, \frac{1}{2})} + (-1)e^{i\frac{2\pi}{a}(t_1, t_2, t_3) \cdot a(0, \frac{1}{2}, \frac{1}{2})} \quad (2.29) \\ &= 1 + e^{i\pi(t_1+t_2)} - e^{i\pi(t_2+t_3)} - e^{i\pi(t_1+t_3)}. \end{aligned}$$

This means that any reflections associated with fcc ( $t_1$ ,  $t_2$  and  $t_3$  all even or all odd) will cause the structure factor to be zero. In fact, the only reflections allowed are either: a)  $t_1, t_2$  even,  $t_3$  odd b)  $t_1, t_2$  odd  $t_3$  even. So, (111) and (100) are not allowed but (110) and (001) are.

A further application of Eq. 2.23 is expanded upon in Chap. 4.

## Inelastic Scattering

Inelastic magnetic scattering is proportional to the dynamic structure factor

$$S(\boldsymbol{\kappa}, \omega) = \sum_{\alpha, \beta=x, y, z} S^{\alpha\beta}(\boldsymbol{\kappa}, \omega) (\delta_{\alpha\beta} - \hat{\kappa}_\alpha \hat{\kappa}_\beta), \quad (2.30)$$

where  $S^{\alpha\beta}(\boldsymbol{\kappa}, \omega)$  is the double Fourier transform of the correlation function  $\langle S_i^\alpha(0) S_j^\beta(t) \rangle$  and can be calculated using the spin wave analysis dispersion relations along with standard Green's functions techniques [44].  $S^{\alpha\beta}(\boldsymbol{\kappa}, \omega)$  is equal to the imaginary part of the time Fourier transform of the retarded Green's function

$$G^{\alpha\beta}(\boldsymbol{\kappa}, \omega) = -iG(t) \langle [S_{\boldsymbol{\kappa}}^\alpha(t), S_{-\boldsymbol{\kappa}}^\beta(0)] \rangle. \quad (2.31)$$

The results for a simple AF are given here. The dynamic structure factor for creation (+) and annihilation (-) of a single magnon can be expressed as [44]

$$\sum_{d=0,1} \sum_{\mathbf{q}, \boldsymbol{\tau}} \left( n_{\mathbf{q},d} + \frac{1}{2} \pm \frac{1}{2} \right) \delta(\hbar\omega_{\mathbf{q},d} \mp \hbar\omega) \delta(\boldsymbol{\kappa} \mp \mathbf{q} - \boldsymbol{\tau}) (u_{\mathbf{q}}^2 + v_{\mathbf{q}}^2 + 2u_{\mathbf{q}}v_{\mathbf{q}} \cos(\mathbf{p} \cdot \boldsymbol{\tau})). \quad (2.32)$$

Here,  $d$  corresponds to two separate modes,  $\mathbf{p}$  is a vector joining NN between separate sublattices, and  $n_{\mathbf{q},d} = (e^{\hbar\omega_{\mathbf{q},d}\beta} - 1)^{-1}$ . The  $u_{\mathbf{q}}$  and  $v_{\mathbf{q}}$  are related to  $\omega_{\mathbf{q}}$  through (ignoring constants)

$$u_{\mathbf{q}} \sim \frac{1 + \omega_{\mathbf{q}}}{2\omega_{\mathbf{q}}}, \quad (2.33)$$

$$v_{\mathbf{q}} \sim \frac{1 - \omega_{\mathbf{q}}}{2\omega_{\mathbf{q}}}, \quad (2.34)$$

$$u_{\mathbf{q}}v_{\mathbf{q}} \sim \frac{-\gamma_{\mathbf{q}}}{2\omega_{\mathbf{q}}}, \quad (2.35)$$

with  $\gamma_{\mathbf{q}} \sim (1 - \omega_{\mathbf{q}})$ .

Simplifications can be made based on symmetry, as the analysis can be quite involved. This is illustrated in Chap. 5 for the fcc kagome lattice.

## Chapter 3

# Monte Carlo simulations of the fcc kagome lattice: Competition between triangular frustration and cubic anisotropy

The impact of local cubic anisotropy on the magnetic states of the Heisenberg model on the fcc kagome lattice is examined through classical Monte Carlo simulations. Previous simulations revealed that the macroscopic degeneracy of the two-dimensional (2D) kagome exchange-coupled co-planar spin system partially persists in the 3D case of ABC stacked layers giving rise to a discontinuous phase transition. Local cubic anisotropy is shown to remove this degeneracy by re-orienting the spins out of the co-planar configuration. In addition, the re-oriented states are shown to carry a uniform magnetic moment. Simulation results indicate that the effect of anisotropy is to transform the first-order phase transition to a

continuous one.

## 3.1 Introduction

Szunyogh *et al.* [37] used symmetry arguments supported by electronic structure calculations to demonstrate the importance of an effective local-axis cubic anisotropy term in the spin Hamiltonian for  $\text{IrMn}_3$  (see Fig. 3.1). Its value is estimated to be about 10% of the NN exchange strength and results in the sublattice moments being tilted out of a co-planar configuration along the  $\langle 100 \rangle$  axes while the projection of the spins in the (111) plane maintains the  $120^\circ$  structure.

In this chapter the effects of adding cubic anisotropy to the NN Heisenberg fcc kagome lattice AF are studied through a series of extensive MC simulations. Previous MC results of Heisenberg and XY models on this lattice, that included only exchange effects, revealed the spin degeneracies in three dimensions with the suggestion that the discontinuous phase transition is of the order-by-disorder type [12]. This order-by-disorder phenomenon can be explained by looking at the ground state degeneracy of classical frustrated AFs [18]. If the degeneracy is not a consequence of symmetry, ground states with larger entropy and lowest possible energy can be selected by thermal (or quantum) fluctuations. This can lead to an otherwise unexpected ordered state. While mean field theory predicts a continuous phase transition for all AF magnetic transitions at  $T_N$ , as all terms in the Landau free energy are even due to time reversal symmetry [46], large thermal fluctuations due to the ground state degeneracies select the  $q = 0$  configuration for the kagome lattice which points towards a critical fluctuation driven [47] weakly first-order transition.

In the present work, an analytic calculation of the ground state reveals an

out-of-plane rotation of the sublattice spins driven by the anisotropy as well as a concomitant net magnetic moment perpendicular to the plane. The effect of anisotropy in removing certain degeneracies is demonstrated and the impact of anisotropy on the Néel temperature and various thermodynamic properties is studied. In addition, results from energy histograms and fourth-order cumulants [38] are used to argue that the transition changes from discontinuous to continuous as a consequence of anisotropy reducing degeneracies of the ground state spin configurations.

This chapter is organized as follows. In Sec. 3.2, the Heisenberg model on a 3D kagome fcc lattice is described. Sec. 3.3 provides previous results [12] for a system that has no anisotropy. In Sec. 3.4, analytical calculations are presented for the zero-temperature ground states with anisotropy. In Sec. 3.5, MC simulation results are shown that describe the effect of the anisotropy on the critical temperature and analyze the order of the phase transition in comparison to the results of earlier work without anisotropy. Results are discussed in Sec. 3.6.

## 3.2 Model

A 3D lattice is considered that consists of  $L$  layers of  $L \times L$  spins per kagome (111) plane, ABC stacked as shown in Fig. 1.4. MC simulations were performed on this model for lattice sizes  $L = 18, 24, 30,$  and  $36$  using the Metropolis algorithm. This method gave satisfactory results even down to the lowest relevant temperatures. Typically between  $10^5$  and  $10^7$  Monte Carlo steps (MCS) were used with an initial 10% discard rate for equilibration, determined to be sufficient by analyzing magnetization vs MCS data and also the smoothness of the magnetization vs temperature data. The interactions include NN Heisenberg exchange, and the

effective local cubic anisotropy developed by Szunyogh *et al.* [37], as described by the Hamiltonian

$$\mathcal{H} = J \sum_{\langle i,j \rangle} \mathbf{S}_i \cdot \mathbf{S}_j - K \sum_{\gamma} \sum_{k \subset \gamma} (\mathbf{S}_k \cdot \mathbf{n}_{\gamma})^2, \quad (3.1)$$

where  $i, j$  are summed over all the  $N = \frac{3}{4}L^3$  spins of the entire lattice, with a quarter of the spins being removed due to the geometry of the kagome lattice,  $J \equiv 1$  is the antiferromagnetic coupling of a spin to its four in-plane and four out-of-plane NN spins, and  $K$  denotes the cubic anisotropy constant. Here,  $\gamma$  represents sublattice 1, 2, and 3 and  $k$  is summed over the  $\frac{N}{3} = \frac{1}{3}(\frac{3}{4}L^3)$  spins of sublattice  $\gamma$ ,  $\mathbf{S}_i$  are unit spin vectors at each site, and  $\mathbf{n}_{\gamma}$  are unit vectors in the cube axes directions,  $\mathbf{n}_1 = \hat{\mathbf{x}}, \mathbf{n}_2 = \hat{\mathbf{y}},$  and  $\mathbf{n}_3 = \hat{\mathbf{z}},$  as in Fig. 3.1. Electronic

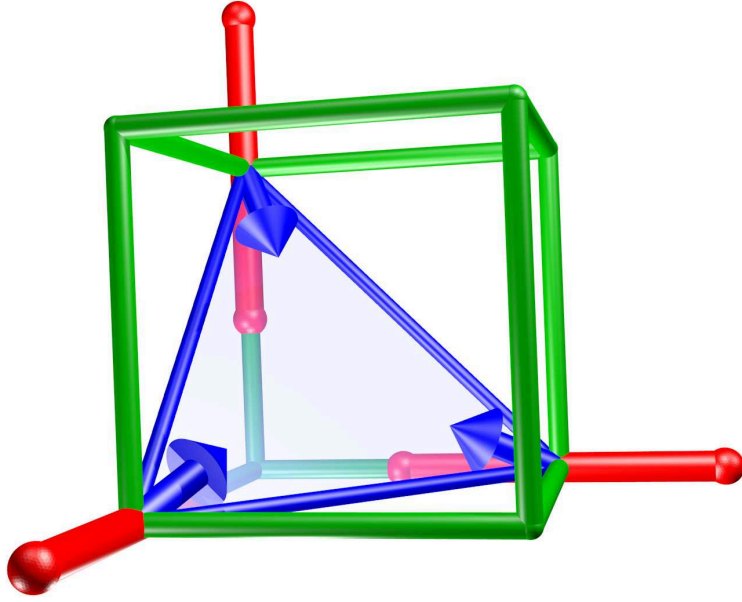


Figure 3.1: Schematic showing a  $120^\circ$  ground-state spin structure (blue arrows) in the cubic (111) plane, along with the local [100] anisotropy axis directions (red rods). The cube shown has sides of length  $a/2$ , where  $a$  is the lattice constant of the fcc unit cell [13].

structure calculations [37] have been used to estimate  $K \approx 0.1$  in the case of  $\text{IrMn}_3$ , however in these series of simulations a range of anisotropy values are considered. The anisotropy term in Eq. 3.1 represents a simplification of a more general form derived from *ab initio* calculations with anisotropic exchange and on-site anisotropy matrices. Symmetry considerations simplify these to an effective anisotropy.

There are two order parameters calculated for this model. The sublattice magnetization is defined as

$$M_t = \frac{1}{N} \left\langle \sum_{\gamma} \left| \sum_{k \subset \gamma} \mathbf{S}_k \right| \right\rangle. \quad (3.2)$$

where the angular brackets denote thermal averaging over MC states. A similar order parameter was also used in the case [12] of  $K = 0$  to characterize the ground-state spin configuration. With the addition of anisotropy, the ferromagnetic magnetization vector becomes nonzero and is defined as

$$M_f = \frac{1}{N} \left| \left\langle \sum_i \mathbf{S}_i \right\rangle \right|. \quad (3.3)$$

It is statistically zero for all temperatures when  $K = 0$  and also zero in the paramagnetic state ( $T > T_N$ ) when  $K \neq 0$ . Its zero-temperature value can be calculated analytically, as shown later in this chapter.

### 3.3 Previous Simulation Results $K = 0$

This thesis extends the MC simulations reported in [12], which examined the NN XY and Heisenberg fcc kagome lattice AFs with no anisotropy. Simulations of energy histograms and Binder energy cumulants were included to study the order of the phase transitions. Degeneracies associated with the lattice through cooling,

heating, and independent temperature MC runs were reported. In cooling (heating) runs, the system is set to a high (low) temperature and gradually decreased (increased) while using the previous temperature step spin configuration result as the initial configuration for the next temperature step. For independent temperature runs, previous spin configurations are not used and a random state is used at the start of every temperature value. These results are summarized here to provide a framework for this chapter.

The results of Ref. [12] showed that only the  $q = 0$  spin configuration was consistent with the eight NN AF exchange interactions. Cooling, heating, and independent temperature runs were simulated over a wide range of temperature that covered the Néel temperature  $T_N$ . Peaks in the specific heat yielded the estimates  $T_N = 0.760 \pm 0.005$  for the XY model and  $T_N = 0.476 \pm 0.005$  for the Heisenberg model.

The orders of the phase transitions were also examined. The energy versus temperature data showed that the XY model exhibited a discontinuity near  $T_N$  which indicated a first-order phase transition. The order of the phase transition of the Heisenberg model proved more difficult to determine, but a small gap in the energy vs temperature plot at large  $N$  suggested a weakly first-order transition. To study this, energy histograms and Binder energy cumulants plots were generated. The energy histograms showed two distinct peaks for both the XY and Heisenberg models, the latter reproduced here in Fig. 3.2, near the Néel temperature, indicative of first-order transitions [38]. A clear separation near  $T_N$  is seen, which illustrates a discontinuous jump in the energy. The energy cumulants were studied at several different lattice sizes in an attempt to extrapolate its behavior as  $L \rightarrow \infty$ , to verify the histogram results. The cumulants extrapolated to  $\frac{2}{3}$  in

the thermodynamic limit which is expected of a continuous transition, but the data is not accurate enough to point towards such a transition. It was concluded that the Heisenberg model in the absence of anisotropy most likely has a weakly first-order transition. In the present work of this chapter, simulations for  $K = 0$  give cumulants that are more consistent with a first-order transition.

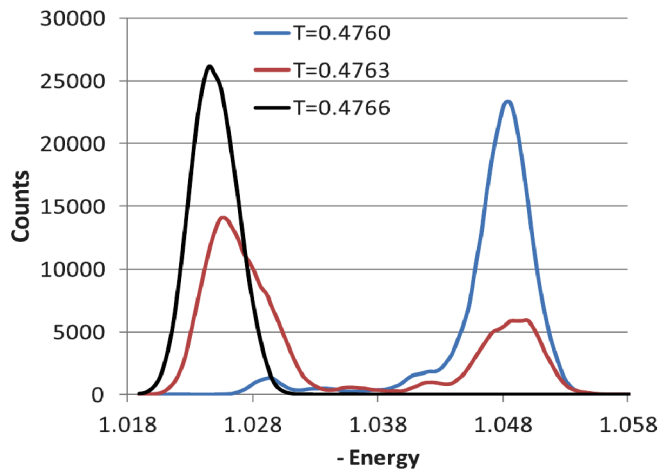


Figure 3.2: Double-peak seen in the energy histogram of the Heisenberg fcc kagome lattice near the Néel temperature for  $K = 0$  indicative of a weakly first-order transition. Figure taken from [12].

Whereas the temperature dependence of the energy obtained from these simulations did not show a difference for cooling, heating, and independent temperature runs, this was not the case for the sublattice magnetization order parameter  $M_t$  and the associated susceptibility. While heating the system from one of its ground states led to the expected paramagnetic behavior above the Néel temperature, the cooling runs showed a lowered value of the order parameter that did not saturate at the same value as anticipated from the ground state spin configuration (as will be shown in Chap. 3 for  $K \gtrsim 0$ ). Furthermore, the independent temperature runs exhibited strong fluctuations below  $T_N$  which indicated energetically equivalent ground states. By looking at the magnetization of the individual sublattices for

different cooling runs, as shown in Fig. 3.3, it was deduced that a plane, such as the (100) plane, containing spins from two separate sublattices could have its spins interchange directions with no cost to the energy. This resulted in a set of discrete degeneracies, in addition to the continuous rotational Heisenberg degeneracy.

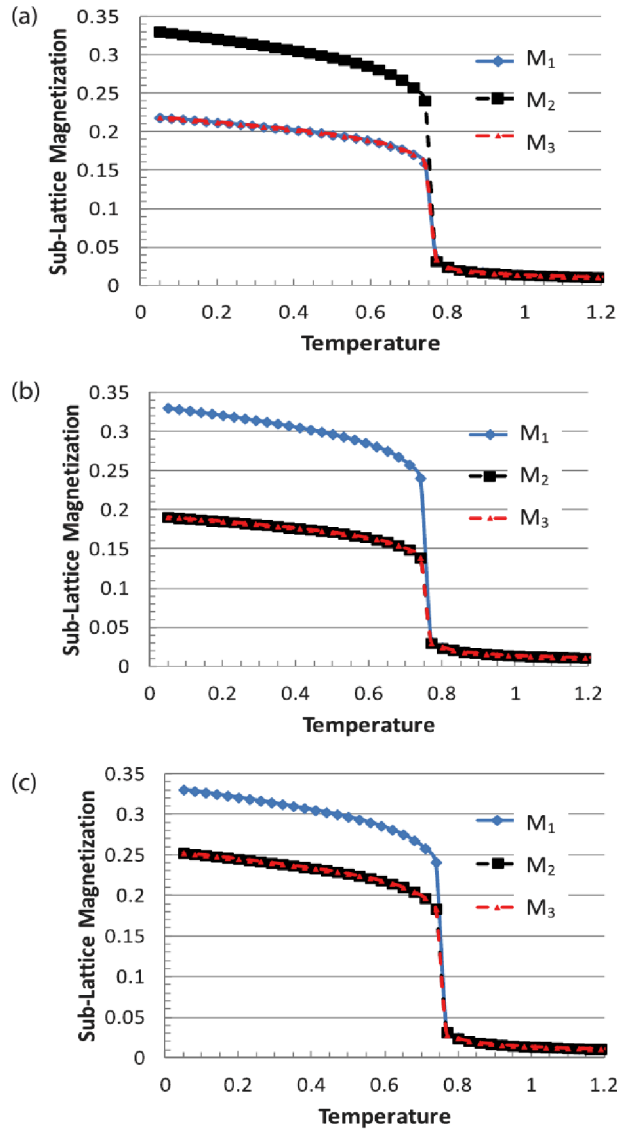


Figure 3.3: Magnetization order parameter vs temperature for individual sublattices ( $M_1$ ,  $M_2$ , and  $M_3$  or  $A$ ,  $B$ , and  $C$ ) at  $K = 0$  for the  $XY$  model corresponding to three different cooling simulations, (a), (b), and (c). The Heisenberg model showed the same behavior. Figure taken from [12].

This discrete degeneracy can be examined by looking at the effects on the sublattice magnetizations. By switching a row of spins in 2D or a plane of spins in 3D, the ground state ( $T = 0$ ) sublattice magnetizations for  $L \times L$  or  $L \times L \times L$  systems can be determined through an analysis of the individual effects of switching spins. This can be summarized in the following equation

$$M_\eta = \frac{\sqrt{\left(\frac{1}{4}L^3 - \frac{3}{2}n\right)^2 + \left(\frac{\sqrt{3}}{2}n\right)^2}}{\frac{3}{4}L^3}, \quad (3.4)$$

where  $\eta$  is the sublattice (1, 2 or 3) and  $n$  is the number of spins switching. In 2D, switching occurs in a row of  $n = L/2$  spins, whereas switching a plane in 3D has  $n = (L/2)(L/2)$ . In the ideal  $q = 0$  ground state,  $M_\eta = \frac{1}{3}$  whereas the maximum variation comes from switching half the population,  $n = \frac{1}{8}L^3$ , giving  $M_\eta = \frac{1}{6}$ . This degeneracy is removed when anisotropy is added, as shown below.

### 3.4 Ground State Properties

To analyze the effect of the anisotropy on the ground state spin configuration, it is convenient to define  $\alpha$  as the cosine of the angle between each sublattice spin and its anisotropy axis  $\alpha = \mathbf{S}_i \cdot \mathbf{n}_i$  and  $\beta$  the cosine of the angle with respect to the other anisotropy axes  $\beta = \mathbf{S}_i \cdot \mathbf{n}_j, i \neq j$ . As such, each spin will have direction cosines of the general form 1 :  $(\pm\alpha, \pm\beta, \pm\beta)$ , 2 :  $(\pm\beta, \pm\alpha, \pm\beta)$ , and 3 :  $(\pm\beta, \pm\beta, \pm\alpha)$ . When  $K = 0$ , this gives specific planar configurations of the Heisenberg spin system's continuously degenerate ground states.

With the addition of a finite anisotropy, the continuous degeneracy is removed, as the spins now have a preferential direction. There are eight possible ground

states when this anisotropy is added to the system, corresponding to the four possible (111) planes with two configurations related to spins being lifted out of either side of each plane. The degeneracies obtained numerically are enumerated as

$$\begin{aligned}
\pm(111) &\rightarrow \pm[\mathbf{S}_1 = (\alpha, -\beta, -\beta), \mathbf{S}_2 = (-\beta, \alpha, -\beta), \mathbf{S}_3 = (-\beta, -\beta, \alpha)], \\
\pm(\bar{1}11) &\rightarrow \pm[\mathbf{S}_1 = (-\alpha, -\beta, -\beta), \mathbf{S}_2 = (\beta, \alpha, -\beta), \mathbf{S}_3 = (\beta, -\beta, \alpha)], \\
\pm(1\bar{1}1) &\rightarrow \pm[\mathbf{S}_1 = (\alpha, \beta, -\beta), \mathbf{S}_2 = (-\beta, -\alpha, -\beta), \mathbf{S}_3 = (-\beta, \beta, \alpha)], \\
\pm(11\bar{1}) &\rightarrow \pm[\mathbf{S}_1 = (\alpha, -\beta, \beta), \mathbf{S}_2 = (-\beta, \alpha, \beta), \mathbf{S}_3 = (-\beta, -\beta, -\alpha)].
\end{aligned} \tag{3.5}$$

Since each spin is a unit vector,

$$\mathbf{S}_i \cdot \mathbf{S}_i = 1 = \alpha^2 + 2\beta^2. \tag{3.6}$$

The system energy per spin is given by

$$\begin{aligned}
E &= -\frac{4}{3}J(\mathbf{S}_1 \cdot \mathbf{S}_2 + \mathbf{S}_2 \cdot \mathbf{S}_3 + \mathbf{S}_3 \cdot \mathbf{S}_1) \\
&\quad - \frac{1}{3}K [(\mathbf{S}_1 \cdot \mathbf{n}_1)^2 + (\mathbf{S}_2 \cdot \mathbf{n}_2)^2 + (\mathbf{S}_3 \cdot \mathbf{n}_3)^2],
\end{aligned} \tag{3.7}$$

with the energy in the ground state given by

$$E = 4(\beta^2 - 2\alpha\beta) - K\alpha^2. \tag{3.8}$$

Finding the energy minimum and solving for  $\alpha$  gives

$$\alpha = \sqrt{1/2 + 1/2\sqrt{1 - 1/[1 + (K + 2)^2/32]}}, \tag{3.9}$$

and [from Eq. 3.6]

$$\beta = \sqrt{\frac{1 - \alpha^2}{2}}, \quad (3.10)$$

using the positive values of the square roots to give physical solutions. When  $K = 0$ ,  $\alpha = 2/\sqrt{6}$  and  $\beta = 1/\sqrt{6}$  which defines spins in the co-planar  $120^\circ$  spin structure.

For low values of  $K$ , an expansion can be obtained which gives an energy per magnetic site in the ground state of  $E \approx -2 - 2K/3$ . The degeneracy that corresponded to interchanging sublattice spins in a plane at zero anisotropy will now have an energy cost of  $K/(3L)$ , thus removing the degeneracy up to order  $K$ .

When  $K = 0$ , the spins are in one of many degenerate coplanar ground states subject to the requirement that the interspin angle on a triangle be  $120^\circ$ . This angle can be calculated using

$$\mathbf{S}_i \cdot \mathbf{S}_j = \beta^2 - 2\alpha\beta, \quad (3.11)$$

for any  $i \neq j$  with the analysis above for finite  $K$ . The results in Fig. 3.4 show how the addition of anisotropy modifies the  $120^\circ$  spin configuration. In the limit of very large  $K$ , the angle between spins reaches  $90^\circ$  where the spins are no longer in the (111) plane and are pointing along the anisotropy (cube axes) directions.

For any nonzero anisotropy the spins are no longer coplanar and have a net moment directed out of the (111) plane, given by

$$\begin{aligned} \mathbf{M}_f &= \mathbf{S}_1 + \mathbf{S}_2 + \mathbf{S}_3 \\ &= [\pm(\alpha - 2\beta), \pm(\alpha - 2\beta), \pm(\alpha - 2\beta)], \end{aligned} \quad (3.12)$$

with its norm equal to  $(\alpha - 2\beta)/\sqrt{3}$ . The magnetization as a function of  $K$  is shown in Fig. 3.4, where in the limit of large  $K$ ,  $M \rightarrow \frac{1}{\sqrt{3}}$ .

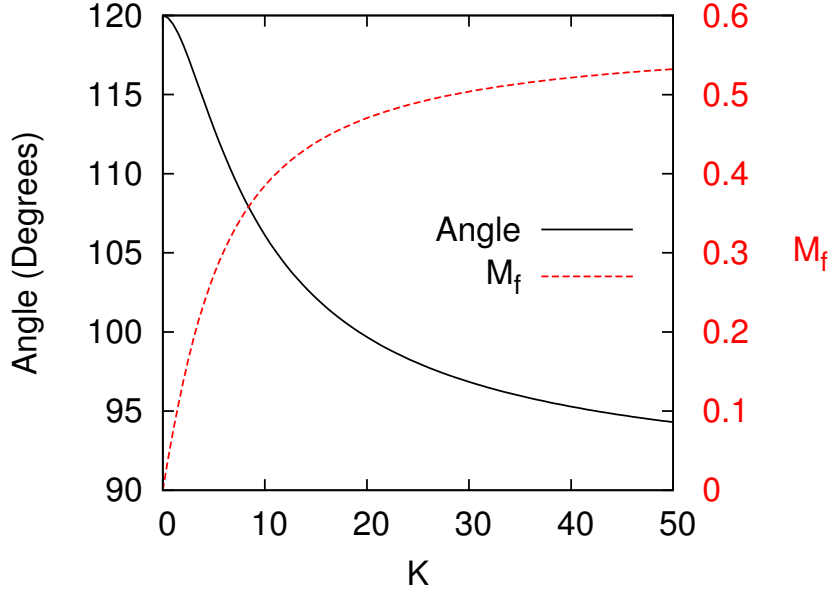


Figure 3.4: Interspin angle and magnetic moment at zero temperature vs anisotropy strength [13].

### 3.5 Simulation Results

MC simulation results for the  $K = 0$  Heisenberg model on the fcc kagome lattice [12] demonstrated the onset of long-range  $q = 0$  spin order at  $T_N = 0.476J$ . Degeneracies were evident by examining the total order parameter  $M_t$  in cooling runs, where complete saturation,  $M_t \rightarrow 1$  at  $T = 0$ , does not occur due to sublattice spin switching, as seen in Fig. 3.3.

Figure 3.5 shows results for the total order parameter  $M_t$  as a function of temperature in cooling runs for values of  $K$  between 0 and 0.06 for  $L = 24$ . At  $K = 0.03, 0.05$ , and  $0.06$ , the system fully saturates, indicating that it has relaxed

to a ground state spin configuration in the limit  $T \rightarrow 0$ ; however, for  $K = 0.01$  and  $0.04$  the order parameter  $M_t$  does not saturate in the limit  $T \rightarrow 0$  indicating that the system has locked into a low energy spin configuration that includes one or more defect. The particular low energy spin configuration that the system locks into upon cooling below  $T_N$  is largely random and the impact of  $K$  on reducing the degeneracy is dependent upon its value relative to thermal fluctuations as well as the system size and number of MCSs. For  $K$  larger than  $\approx 0.06$ , this is no longer the case (for the set of simulation conditions used in this example) and the sublattice magnetization order parameter always tends toward unity as  $T = 0$  is approached. This result, together with the analysis of the ground state, is suggestive that any nonzero value of  $K$  eliminates the degeneracy that is associated with the NN Heisenberg model on a kagome lattice.

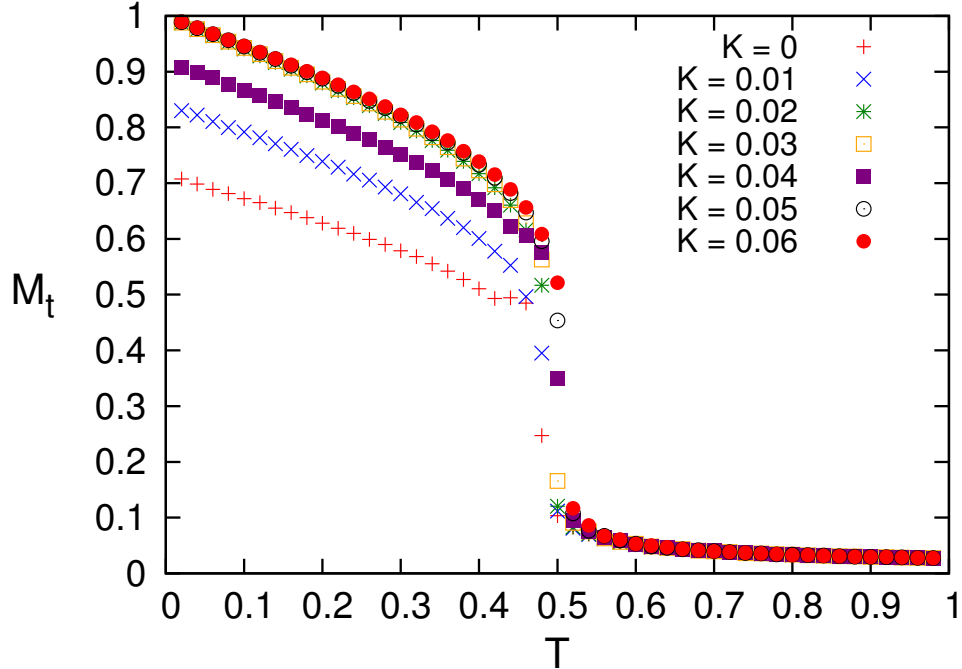


Figure 3.5: Sublattice magnetization order parameter vs temperature for small values of  $K$  from simulations with  $L = 24$  [13].

The impact of anisotropy on the transition temperature  $T_N$  can be estimated through the location of the specific-heat peak, as shown in Fig. 3.6 for  $K = 0, 0.1, 0.5, 1, 5,$  and  $10$  taken from the same cooling runs as the magnetization. Horizontal error bars are not shown, but are quite small, on the order of  $T = 0.01$  for low values of  $K$  and  $T_N$ . Higher values of  $T_N$  have a higher uncertainty, on the order of  $T = 0.03$  and would require better simulations for more accurate results. Note that for large  $K$  the system acts primarily under the influence of the single-site axial anisotropy. In this case, a broad maximum in the specific heat is expected [48] at  $T \approx K/6$  due to the onset of short-range correlations well above  $T_N$ . Such a maximum is seen in the inset of Fig. 3.6 for  $K = 10$  around  $T \approx 1.67$  as a lower peak than the sharp  $T_N$  peak.

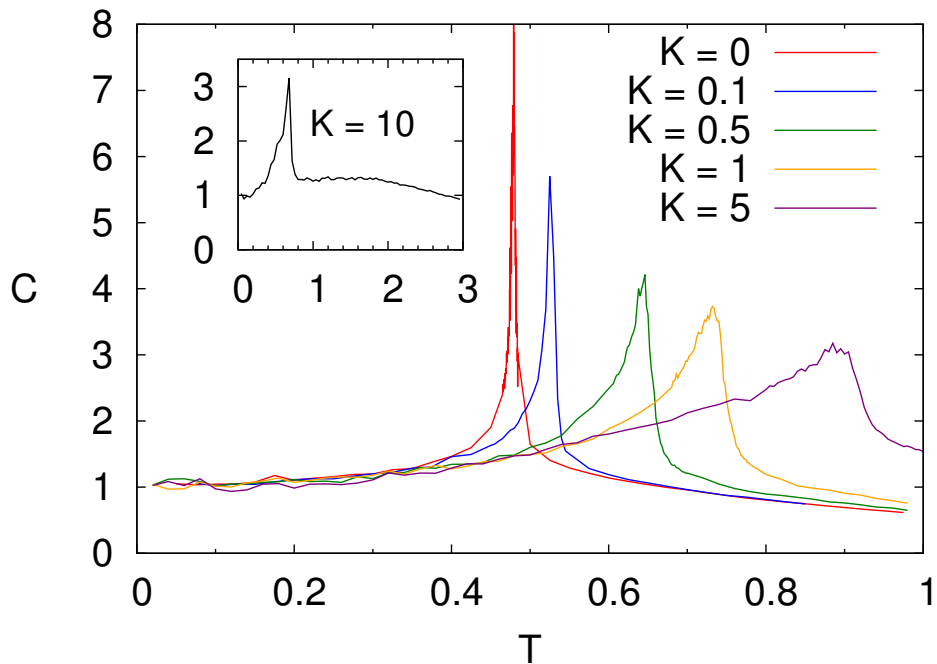


Figure 3.6: Specific heat vs temperature used to locate  $T_N$  for the values of  $K$  indicated from simulations with  $L = 24$ . Inset shows results for  $K = 10$  and the expected lower broad peak at  $T \approx K/6 \approx 1.67$  due to short-range order [13].

Figure 3.7 summarizes the results of estimating  $T_N$  from simulations of the specific heat for a wide range of  $K$  values. For small and moderate values of  $K$  it is seen that  $T_N$  increases to a maximum of about  $0.9J$  at  $K \approx 5$ , followed by a monotonic decrease up to the largest anisotropy value ( $K = 50$ ) examined. In the limit of infinite anisotropy, all NN spins are perpendicular to each other and the interspin exchange interaction would thus be reduced to zero, eliminating long-range order.

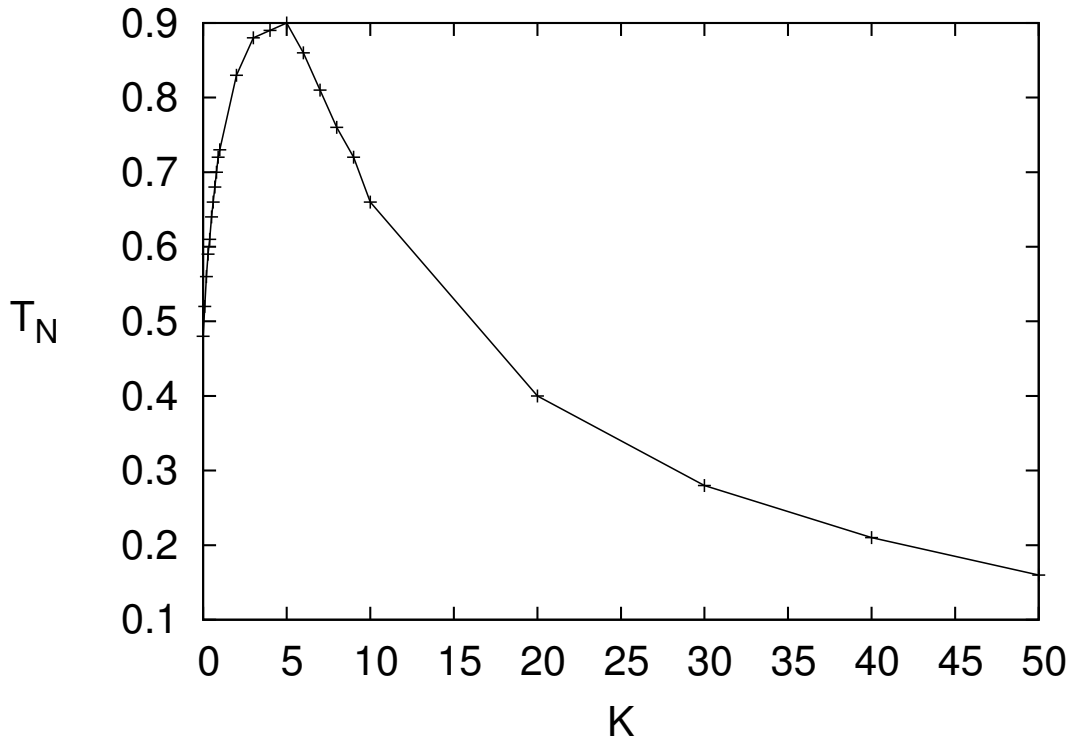


Figure 3.7: Néel temperature  $T_N$  vs the anisotropy strength  $K$  estimated from the specific-heat peaks from simulations with  $L = 24$  [13].

Figure 3.8 shows the total magnetization  $M_f$  vs temperature at  $K = 0, 0.1,$  and  $0.5$ . In the absence of anisotropy, the simulated  $M_f$  is zero for all  $T$ , as expected from the ground-state calculations. Its temperature dependence for the nonzero values of  $K$  is similar to the order parameter results of Fig. 3.5, although much smaller. The values of  $M_f$  extrapolated from these data at  $T = 0$  agree with those expected from the analytic analysis of Sec. 3.4.

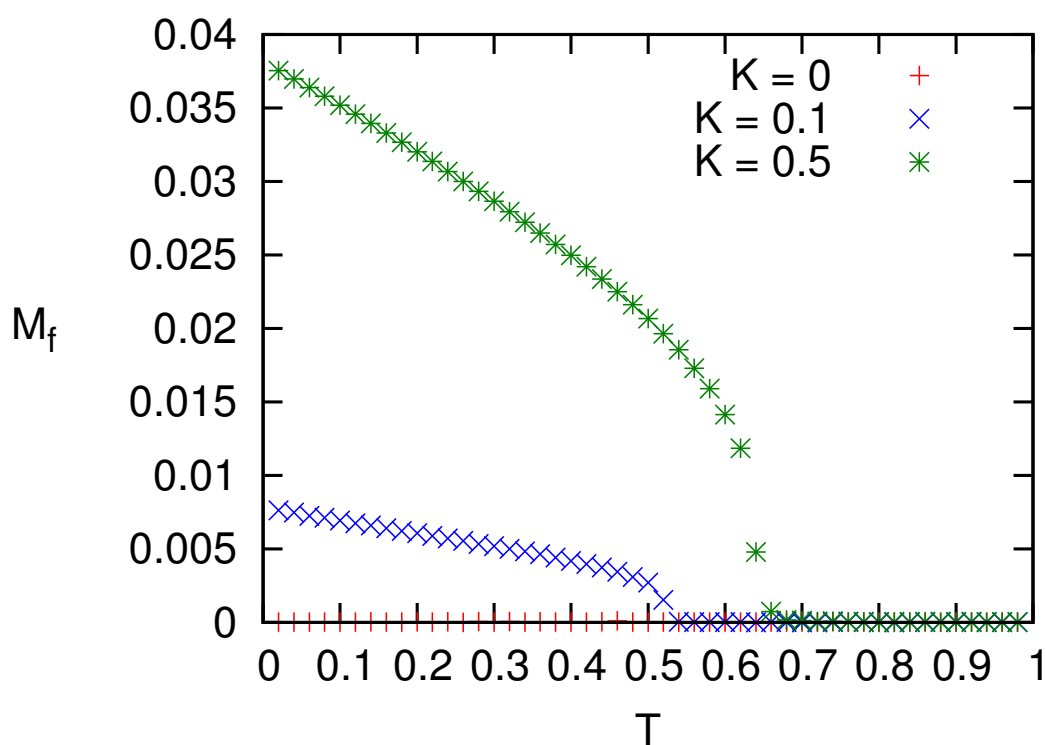


Figure 3.8: Simulation results with  $L = 24$  for the ferromagnetic magnetization vs temperature for the values of  $K$  indicated [13].

In the absence of anisotropy, the Heisenberg fcc kagome lattice has a phase transition that appears to be weakly first-order as deduced from MC simulations. Evidence in support of these ideas was found in MC simulation results of energy histograms and the Binder energy cumulant [12], as shown in Fig. 3.2. The addition of anisotropy removes the usual kagome-type degeneracies and it is believed that this leads to a continuous transition, as would occur within mean-field theory. To verify this, energy histograms and cumulants were calculated for a number of different values of  $K$ . Figure 3.9 shows the results for the energy histograms near the corresponding critical temperatures (determined by the specific-heat peak locations) for  $K = 0.1$  and  $K = 5$ . In contrast with the previous MC results for  $K = 0$ , a double-peak structure is not observed in the present cases indicative of a continuous phase transition.

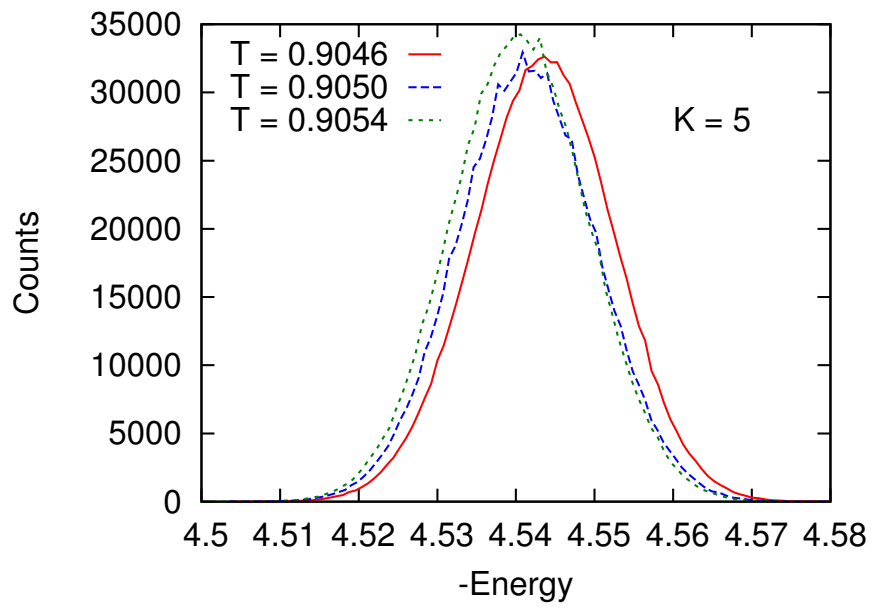
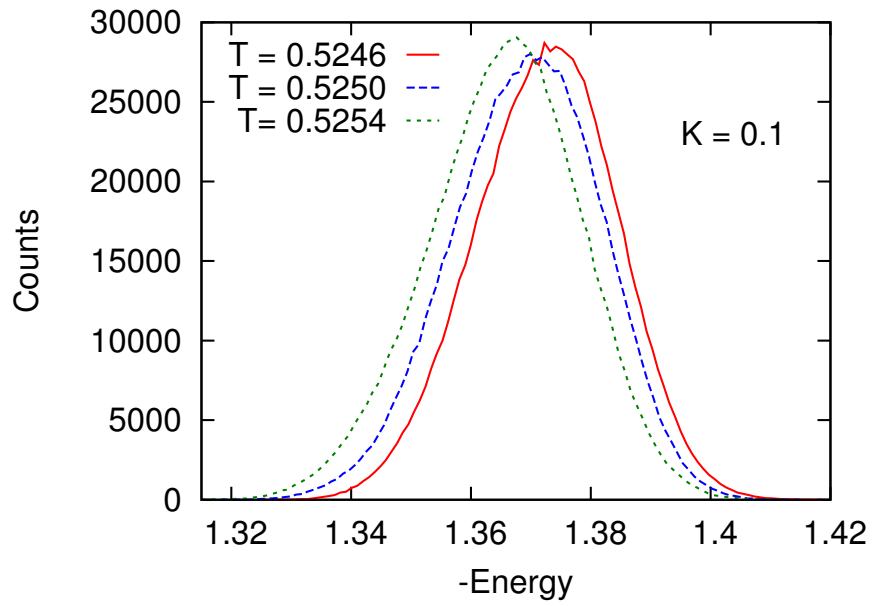


Figure 3.9: Energy histograms at values of  $T$  near  $T_N$  for  $K = 0.1$  and  $K = 5$  with  $L = 36$  from simulations using  $L = 24$  [13].

The energy cumulant, defined by  $U_E = 1 - \langle E^4 \rangle / 3 \langle E^2 \rangle^2$ , was examined in Ref. [12] for  $K = 0$  but provided inconclusive support for a first-order transition [38]. In the present work, this case is studied again along with an analysis of cumulant results at  $K = 0.1, 0.5$ , and  $1$  for lattice sizes  $L = 18, 24, 30$ , and  $36$ . Simulations were performed at temperatures close to  $T_N(L)$  estimated from specific-heat peaks using  $10^6$  MCS. Figure 3.10 shows example data for the cases  $K = 0$  and  $K = 0.1$ . The value of the minimum for each curve was estimated and clearly will depend on the temperature interval examined. Data collected for the study presented in Ref. [12] were at a relatively large interval of  $\Delta T = 0.001$  whereas a smaller value of  $0.0002$  was used in the present work allowing for a more accurate estimate of the minimum.

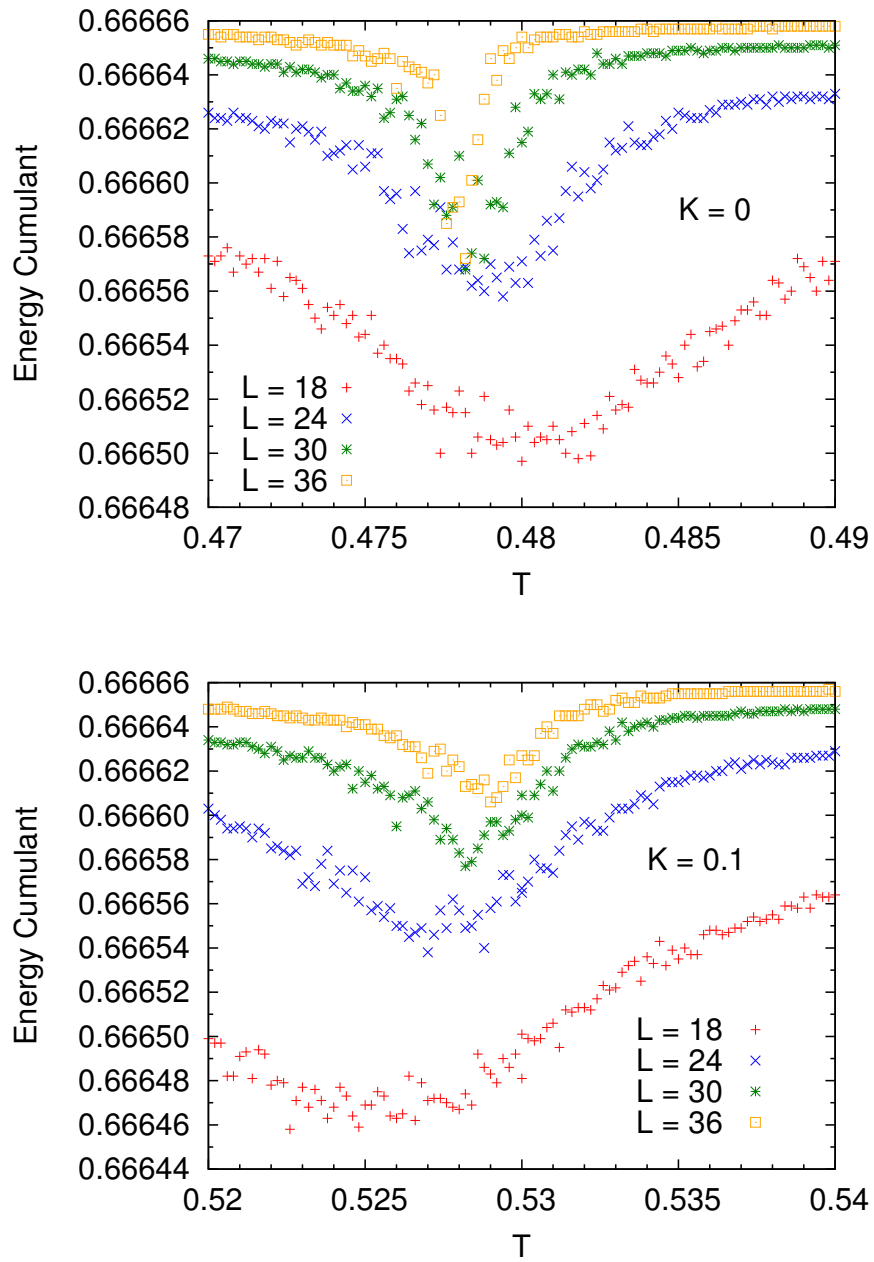


Figure 3.10: Energy cumulants for  $K = 0$  and  $K = 0.1$  at temperatures close to  $T = T_N(L)$  estimated from the specific-heat peaks for the values of  $L$  indicated [13].

Figure 3.11 shows the best estimation of the minimum vs  $1/N$  where  $N$  is the number of magnetic lattice sites ( $N = \frac{3}{4}L^3$ ) for  $K = 0, 0.1, 0.5,$  and  $1$ . In the case of a continuous transition, the minimum should extrapolate to  $2/3$  in the thermodynamic limit [38]. The data seem to show a distinction in the trend of the finite-size scaling between the results for finite  $K$ , which appear to be consistent with the  $2/3$  limit, and the  $K = 0$  case, in support of the notion that nonzero anisotropy drives the transition to be continuous.

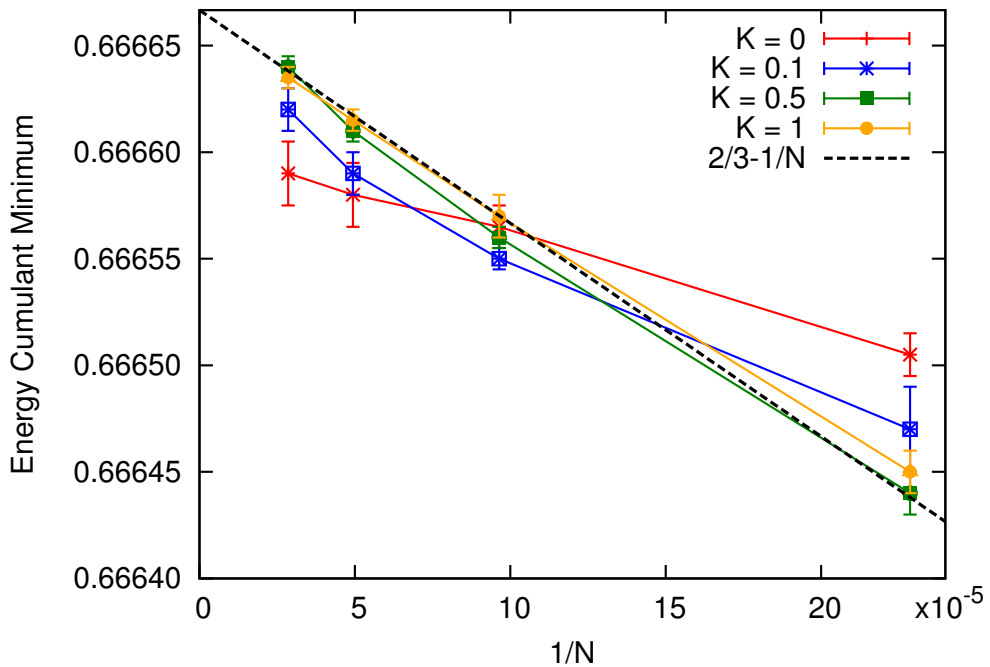


Figure 3.11: Estimated cumulant minimum vs  $1/N$  from the results of Figure 3.10. The broken line shows behavior expected of a model continuous transition [13].

### 3.6 Summary and Conclusions

The extensive Monte Carlo simulations analyzed in this work have demonstrated the importance of cubic anisotropy on the ABC stacked kagome lattice of magnetic

dipoles, relevant for fcc  $\text{IrMn}_3$  and related compounds. An expression for the eight possible degenerate ground states is obtained at  $T = 0$ , allowing for an analytic description of the interspin angle showing an increasing deviation from  $120^\circ$  with increasing  $K$ . As a result of anisotropy, the spins develop a nonzero ferromagnetic moment along the  $[111]$  direction. Simulations show that the Néel temperature increases nonlinearly as the anisotropy strength is increased until a maximum at  $K \approx 5$  when it begins to overwhelm the exchange interaction. The transition temperature then decreases for larger  $K$ , approaching zero in the limit of infinite anisotropy.

It is argued that the large spin degeneracy of the pure isotropic Heisenberg model is removed with the addition of cubic anisotropy and that the phase transition to long-range  $q = 0$ , local  $120^\circ$ , magnetic order changes from first-order [12] to continuous. Evidence to support this conjecture comes from simulation data on the energy histograms near  $T_N$ , which show a double peak at  $K = 0$  and a single peak at  $K \neq 0$ . Analysis of the Binder energy cumulants is also consistent with this conclusion. It is speculated that the spin degeneracy of the pure Heisenberg model for this lattice leads to a first-order transition driven by critical fluctuations. An analysis of the spin-wave modes in the 3D pure Heisenberg system show the presence of a zero-energy mode (for wave vectors along certain directions) which develops a finite energy of order  $K$  as anisotropy is added, as explored in Chap. 5. It is anticipated that finite-temperature fluctuations remove the degeneracy associated with this  $K = 0$  mode. A somewhat analogous effect has been shown to occur in the pyrochlore antiferromagnet  $\text{Er}_2\text{Ti}_2\text{O}_7$  which involves a partial removal of the infinite ground-state degeneracy due to the addition of exchange anisotropy [49],[50],[51].

The development of a finite magnetic moment along the  $[111]$  direction as a consequence of anisotropy and the expected in-plane canting of the spins on the top layer of the antiferromagnet in the presence of a ferromagnetic layer [11] are expected to be important to describe the exchange bias seen in  $\text{IrMn}_3$ .

# Chapter 4

## Magnetic Elastic Scattering

Considered here are the effects of anisotropy on magnetic elastic scattering in the fcc kagome lattice, with a focus on  $\text{IrMn}_3$ . Appendix A.2 explains some of the more fundamental concepts necessary to understand the theory. Both Appendix A.2 and this chapter serve to expand upon the brief introduction given in Chap. 2 (also see Ref. [44]).

### 4.1 Nuclear cross section

To study the effects of magnetic elastic scattering, it is important to know the form of both the nuclear and magnetic cross sections. The nuclear cross section can be written as

$$\left(\frac{d\sigma}{d\Omega}\right)_{\text{nuc,coh,el}} = N \frac{(2\pi)^3}{\nu_0} \sum_{\boldsymbol{\tau}} \delta(\boldsymbol{\kappa} - \boldsymbol{\tau}) |F_N(\boldsymbol{\kappa})|^2, \quad (4.1)$$

and involves the nuclear structure factor

$$F_N(\boldsymbol{\kappa}) = \sum_d \bar{b}_d e^{i\boldsymbol{\kappa} \cdot \mathbf{d}} e^{-W_d}, \quad (4.2)$$

with  $\boldsymbol{\kappa} = \mathbf{k} - \mathbf{k}'$ ,  $b_d$  the scattering length for atom  $d$ . The Debye-Waller factor  $W_d$ , often called temperature factor, is specific to each atom and is often approximated to be the same for all the atoms and is often ignored. This allows the nuclear structure factor of IrMn<sub>3</sub> to be written, without the temperature factor, as

$$F_N(\boldsymbol{\kappa}) = [b_{\text{Ir}} + b_{\text{Mn}}((-1)^{h+k} + (-1)^{h+l} + (-1)^{k+l})], \quad (4.3)$$

with the relevant scattering lengths  $b_{\text{Ir}} = 10.6 \times 10^{-13}$  cm and  $b_{\text{Mn}} = -3.73 \times 10^{-13}$  cm [6]. Here, as in a typical fcc crystal, the atoms in the basis are such that there is an Ir atom at the origin with three Mn neighbor atoms at face centers. If  $h = k = l$  or they are all even or all odd, there is an almost exact accidental cancellation of the structure factor due to  $b_{\text{Ir}} + 3b_{\text{Mn}}$  being almost zero. This is an unusual and unfortunate feature of IrMn<sub>3</sub>. The difference between  $(b_{\text{Ir}} - b_{\text{Mn}})^2$  and  $(b_{\text{Ir}} + 3b_{\text{Mn}})^2$  is almost a factor of 600. This makes it difficult to differentiate magnetic and nuclear peaks as there are forbidden magnetic peaks for the same  $\boldsymbol{\kappa}$  that give a nearly zero nuclear peak, as is shown below. There is also the possibility of the IrMn<sub>3</sub> containing a significant proportion of a disordered phase. In such a phase, the manganese and iridium do not align in a Cu<sub>3</sub>Au-type structure with the magnetic ions at face centers. Experimentally, it is difficult to create a sample with no disordered phase. If there is a significant presence of this disordered phase, the (111) and (200) peak locations will be slightly altered given that the lattice parameter  $a$  for IrMn<sub>3</sub> is larger in the disordered phase, as it does not possess the

same magnetic structure as the ordered phase [6].

## 4.2 Magnetic form factor

For the magnetic cross section, an expression for the magnetic form factor is needed. In the usual dipole, or spherical, approximation this is given by [52],[53]

$$F(s) = Ae^{-as^2} + Be^{-bs^2} + Ce^{-cs^2} + D, \quad (4.4)$$

where  $s = |q|/4\pi$ . This function approaches zero at  $s \gtrsim 1\text{\AA}^{-1}$  and is negligible for  $|q| \gtrsim 4\pi\text{\AA}^{-1}$ .

The values of the dimensionless [54] constants depend on the oxidation state of Mn, as indicated in Table 4.1.

State	A	a	B	b	C	c	D
Mn <sup>0</sup>	0.2438	24.9629	0.1472	15.6728	0.6189	6.5403	-0.0105
Mn <sup>1</sup>	-0.0138	0.4214	0.4231	24.6680	0.5905	6.6545	-0.0010
Mn <sup>2</sup>	0.4220	17.6840	0.5948	6.0050	0.0043	-0.6090	-0.0219
Mn <sup>3</sup>	0.4198	14.2829	0.6054	5.4689	0.9241	-0.0088	-0.9498
Mn <sup>4</sup>	0.3760	12.5661	0.6602	5.1329	-0.0372	0.5630	0.0011

Table 4.1: Dimensionless Mn constants for different oxidation states as used in the magnetic form factor [53].

Thus far the local Heisenberg exchange model has been adequate in describing the observed equilibrium spin structure. As Mn is a transition metal, a more precise model would take into account the itinerant nature of the electrons which could give a better clue on the correct oxidation state. Despite the significant variation in constants for the different oxidation states, differences in  $F$  as a function of the oxidation state are small, as shown in Fig. 4.1.

The wavevector in Fig. 4.1 is  $|q|$  (or  $\kappa$ ) as used in the experiments and is

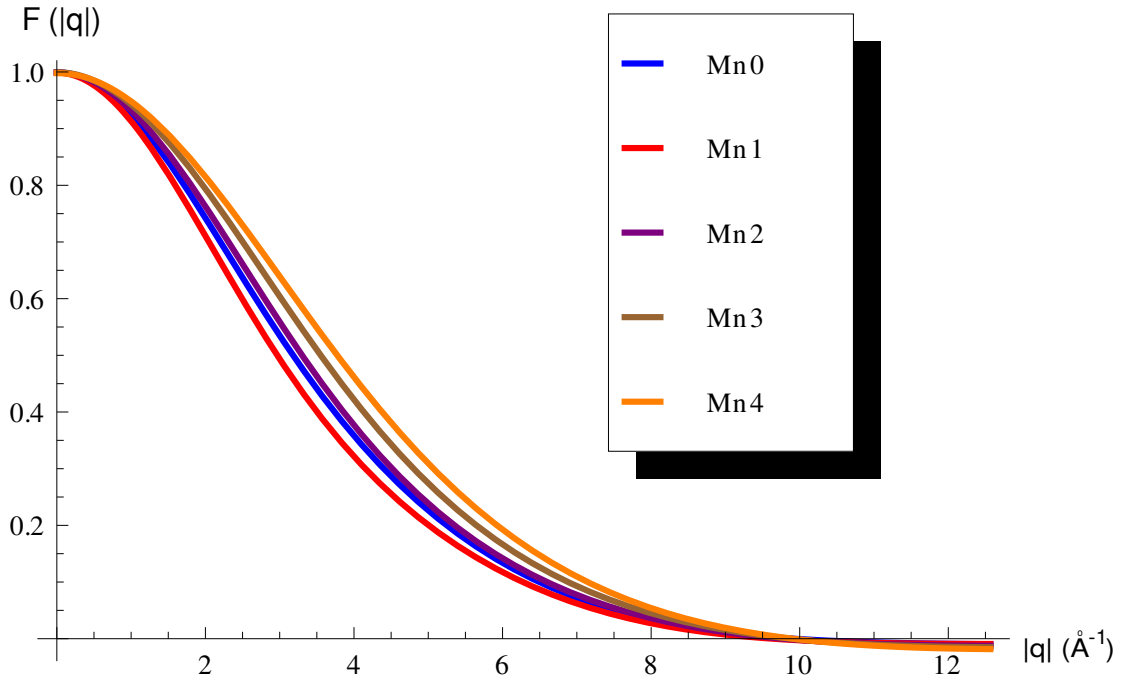


Figure 4.1: Magnetic form factor vs wavevector for different oxidation states of Mn (from Eq. 4.4).

calculated through  $|q| = \frac{2\pi}{a}\sqrt{h^2 + k^2 + l^2}$ , with  $a$  the lattice constant estimated to be around 3.75 – 3.77 at low temperatures [6]. Based on this figure, the oxidation state of Mn does not have a large impact on the form factor.

### 4.3 Magnetic cross section

The factors involved in the scattering cross section which allows a determination of the relative peak heights and positions for different scattering vectors can be calculated for the fcc kagome lattice. The following simplified analysis assumes  $K = 0$  (zero anisotropy) for one ground state (single domain) as it is possible to obtain a simple analytical result. From Eqs. A.15, A.16 and A.20, the magnetic

cross section can be written

$$\frac{d\sigma}{d\Omega} = r_0^2 N \frac{(2\pi)^3}{\nu_0} \sum_{\boldsymbol{\tau}} \delta(\boldsymbol{\kappa} - \boldsymbol{\tau}) e^{-2W(\boldsymbol{\tau})} \left( \frac{1}{2} g F(\boldsymbol{\tau}) \right)^2 \langle S \rangle^2 I(\boldsymbol{\tau}), \quad (4.5)$$

with  $I(\boldsymbol{\tau})$  given by

$$I(\boldsymbol{\tau}) = \sum_{\alpha\beta} \sum_{dd'} \hat{S}_{d'}^{\alpha} \hat{S}_d^{\beta} e^{i\boldsymbol{\tau} \cdot (\mathbf{d} - \mathbf{d}')} (\delta_{\alpha\beta} - \hat{\tau}_{\alpha} \hat{\tau}_{\beta}). \quad (4.6)$$

This takes into account that all magnetic unit cells are the same size and each sublattice spin has the same orientation within its unit cell for all Mn ions, each having the same average value of the spin  $\langle S_d \rangle$ . Both double sums give rise to  $3 \times 3$  terms for a total of  $9 \times 9 = 81$  terms. While  $I$  depends on reciprocal lattice vectors  $\boldsymbol{\tau}$ , the previous equation and the following development focuses on  $\boldsymbol{\kappa}$ , with the knowledge that peaks appear when  $\boldsymbol{\kappa} = \boldsymbol{\tau} = \frac{2\pi}{a} (t_1, t_2, t_3)$  ( $a$  being the cubic lattice constant) for the simple cubic symmetry with  $t_1, t_2$ , and  $t_3$  any integer, as the fcc system is treated as simple cubic with a basis.

In the  $q = 0$  ground state spin structure as described in Chap. 3, the system has a magnetic unit cell (equal to the cubic crystal unit cell) of three spins such that there are three sublattices. The spin orientations for the three sublattices are chosen as

$$\hat{\mathbf{S}}_A = \left( -\frac{1}{\sqrt{6}}, -\frac{1}{\sqrt{6}}, \sqrt{\frac{2}{3}} \right), \quad (4.7)$$

$$\hat{\mathbf{S}}_B = \left( -\frac{1}{\sqrt{6}}, \sqrt{\frac{2}{3}}, -\frac{1}{\sqrt{6}} \right), \quad (4.8)$$

$$\hat{\mathbf{S}}_C = \left( \sqrt{\frac{2}{3}}, -\frac{1}{\sqrt{6}}, -\frac{1}{\sqrt{6}} \right). \quad (4.9)$$

with their position vectors being

$$\mathbf{d}_A = a \left( \frac{1}{2}, \frac{1}{2}, 0 \right) \quad \mathbf{d}_B = a \left( \frac{1}{2}, 0, \frac{1}{2} \right) \quad \mathbf{d}_C = a \left( 0, \frac{1}{2}, \frac{1}{2} \right). \quad (4.10)$$

Using these results and

$$\begin{aligned} \mathbf{D}_x &= \mathbf{d}_A - \mathbf{d}_B = -(\mathbf{d}_B - \mathbf{d}_A) = a \left( 0, \frac{1}{2}, -\frac{1}{2} \right) \\ \mathbf{D}_y &= \mathbf{d}_A - \mathbf{d}_C = -(\mathbf{d}_C - \mathbf{d}_A) = a \left( \frac{1}{2}, 0, -\frac{1}{2} \right) \\ \mathbf{D}_z &= \mathbf{d}_B - \mathbf{d}_C = -(\mathbf{d}_C - \mathbf{d}_B) = a \left( \frac{1}{2}, -\frac{1}{2}, 0 \right) \end{aligned} \quad (4.11)$$

in Eq. 4.6 yields

$$\begin{aligned} I(\boldsymbol{\kappa}) &= \frac{1}{3} \sum_{\alpha} \left[ (1 - \hat{\kappa}_{\alpha}^2) [3 + \cos(\boldsymbol{\kappa} \cdot \mathbf{D}_{\alpha}) - 2 \cos(\boldsymbol{\kappa} \cdot \mathbf{D}_{\alpha'}) - 2 \cos(\boldsymbol{\kappa} \cdot \mathbf{D}_{\alpha''])] \right. \\ &\quad \left. - \hat{\kappa}_{\alpha} \hat{\kappa}_{\alpha'} [5 \cos(\boldsymbol{\kappa} \cdot \mathbf{D}_{\alpha'}) - \cos(\boldsymbol{\kappa} \cdot \mathbf{D}_{\alpha'}) - \cos(\boldsymbol{\kappa} \cdot \mathbf{D}_{\alpha}) - 3] \right], \end{aligned} \quad (4.12)$$

where  $\alpha = x, y,$  and  $z$ . Here,  $\alpha'$  and  $\alpha''$  are defined such that  $x' = y, x'' = z,$   
 $y' = z, y'' = x, z' = x,$  and  $z'' = y$ .

If  $\boldsymbol{\kappa} = (k, k, k)$ , it is straightforward to show that  $I = 0$ . As such, there are no (111), (222), etc. reflections. It can also be determined that  $I = 0$  if  $h, k,$  and  $l$  are all simultaneously even or all odd, as in an fcc crystal. If those condition are not met,  $I > 0$  and there are reflections when  $\kappa = \tau$ , for simple cubic rules ( $(hkl)$  with any integer  $h, k,$  and  $l$ ).

The peak heights depend on  $I$  times the magnetic form factor squared. To give an idea of how it varies with  $\boldsymbol{\kappa}$ , the form factor for  $\text{Mn}^0$  (as the oxidation state has

minimal impact on the form factor, another state could also have been chosen) is used and the results are shown in Tab. 4.2. There is no peak for  $h, k, l$  all odd or all even.

$h$	$k$	$l$	$I \times  F( q ) _{Mn^0}^2$
1	0	0	1.140
1	1	0	1.961
1	1	1	0
2	0	0	0
2	1	0	1.920
2	1	1	1.492
2	2	0	0
3	0	0	0.381
2	2	1	1.059
3	1	0	0.743
3	1	1	0
2	2	2	0
3	2	0	0.567

Table 4.2: Relative magnetic peak heights from Eq. 4.4, Tab. 4.1 and Eq. 4.12.

For Bravais systems, the ratio of the magnetic and nuclear cross sections  $(\frac{d\sigma}{d\Omega})_{\text{mag,el}} / (\frac{d\sigma}{d\Omega})_{\text{nuc,coh,el}}$  is simple. The fcc kagome lattice is not a Bravais system, but the Debye-Waller factor can be approximated as if for a single ion (which uses a mean atomic mass), giving

$$\left(\frac{d\sigma}{d\Omega}\right)_{\text{mag,el}} / \left(\frac{d\sigma}{d\Omega}\right)_{\text{nuc,coh,el}} = \frac{1}{|F_N(\boldsymbol{\kappa})|^2} r_0^2 \langle S \rangle^2 |F(|q|)|^2 I, \quad (4.13)$$

with  $F_N(\boldsymbol{\kappa})$  the nuclear cross section showed earlier. In this,  $\langle S \rangle$  at  $T = 0$  is around 0.4 for Mn. Eq. 4.13 has a very similar form to what is shown in Tab. 4.2 and indeed would give the same results multiplied by a constant as the nuclear peaks are always the same if  $h, k$ , and  $l$  are not either all even or all odd (magnetic peaks). In their report, Tomeno *et al.* [6] found enough evidence to classify  $\text{IrMn}_3$

as having the  $q = 0$  structure based on the location of observed peaks as described here.

When looking at the effects of anisotropy, a similar analysis can be followed, where a different set of spins  $\tilde{\mathbf{S}}$  are used in Eq. 4.6. These ground spins change when anisotropy is added, as described in Eq. 3.5, which adds a dependence on the strength of  $K$  through  $\alpha$  and  $\beta$ . Multiplying the new  $I$  by the form factor squared, summing over possible permutations of  $h$ ,  $k$ , and  $l$  and applying a distribution around the peak centers is then carried out numerically to obtain Fig. 4.2, showing the peak height difference for different values of  $K$  (0 and  $5J$  in the figure). Since the expected experimental value of  $K$  is only around  $0.1J$ , the effect of anisotropy on the elastic scattering is not pronounced. The impact of  $K$  on inelastic scattering is examined in detail in the following chapter.

For zero anisotropy, the spins have a  $120^\circ$  structure and lie in the (111) plane, but for  $K > 0$  the spins are non-planar each with a component along the [111] direction leading to a non-zero magnetization. The value of  $I(h, k, l)$  depends on the direction of  $\vec{\kappa}$  with respect to the [111] direction. For zero anisotropy, there are no contributions from  $h, k, l$  all even or all odd whereas for  $K > 0$  these terms become non-zero and are proportional to the magnetization squared. However, these additional peaks are very small compared to the principal peaks. The results for  $K/J = 0.1$  were calculated, but showed especially small differences. Fig. 4.2 shows the elastic scattering intensity vs wavevector  $\kappa$  for  $K/J = 0$  and  $K/J = 5$  using values of the form factor for Mn ions. These results would be appropriate for a powder sample as all marked peaks correspond to a summation of the multiplicity for a given  $h$ ,  $k$ , and  $l$ . A more promising signature of anisotropy in  $\text{IrMn}_3$  may be through inelastic magnetic scattering.

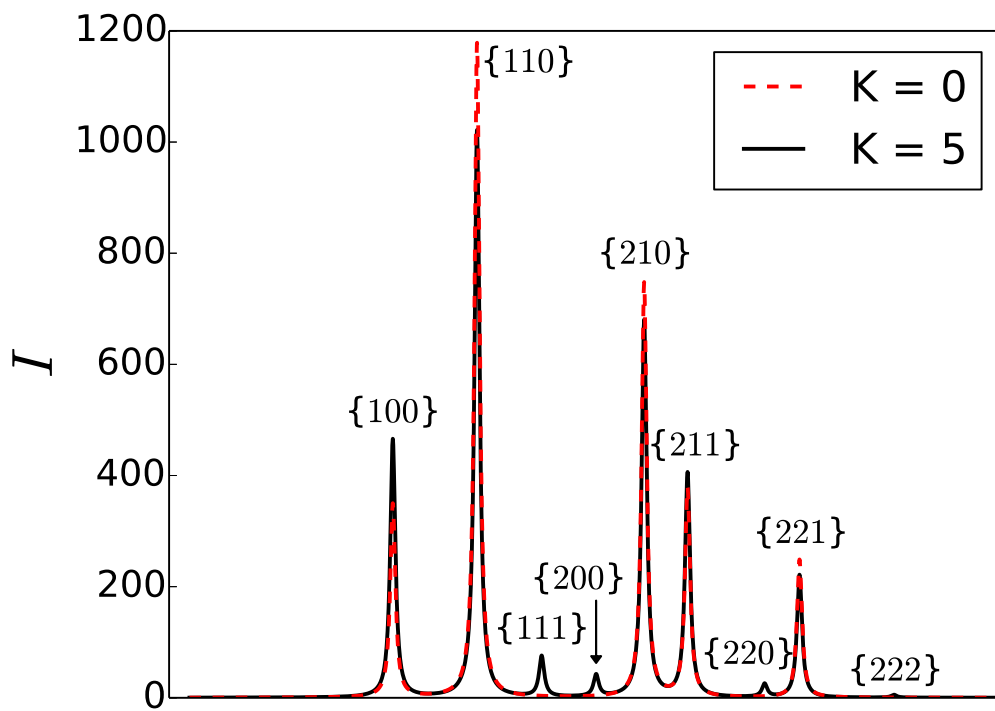


Figure 4.2: Elastic scattering showing several peaks for  $K/J = 0, 5$  and  $J = J' = 1$ . The intensity of the peaks is plotted vs the wavevector  $\kappa$ , focusing on the locations of the peaks. The peaks at 111, 200, and 220 are unique to  $K > 0$  [14].

# Chapter 5

## Spin Waves and Inelastic Magnetic Scattering in the Anisotropic fcc Kagome Antiferromagnet

### 5.1 Introduction

Classical spin wave calculations demonstrate that the macroscopic continuous degeneracy associated with the two-dimensional kagome Heisenberg spin lattice persists in the case of the stacked fcc structure giving rise to zero energy modes in three dimensions. The addition of an effective local cubic anisotropy is shown to remove this continuous degeneracy and introduce a gap in the spectrum as well as modify the inelastic scattering function  $S(\boldsymbol{\kappa}, \omega)$ . This scenario supports earlier Monte Carlo simulations which indicate that the phase transition to long

range  $q = 0$  magnetic order is driven to be discontinuous by critical fluctuations associated with the large degeneracy in the absence of anisotropy, but becomes continuous with the addition of anisotropy. The results are relevant to Ir-Mn alloys which are widely used in the magnetic storage industry in thin film form as the antiferromagnetic pinning layer in spin-valve structures.

Evidence for zero-energy spin wave modes through inelastic neutron scattering experiments has been reported in a system with weakly coupled kagome layers [24] (more exotic ground states have also been predicted to occur in the 2D kagome spin lattice when quantum effects are important [55]). Zero-energy (classical) modes also occur in the stacked triangular lattice antiferromagnet where the inter-layer exchange coupling  $J'$  differs from the intra-layer interaction  $J$  (a model of the magnetism in solid oxygen) [56],[57],[58]. In this case of rhombohedral symmetry, the degeneracy is associated with ground state helimagnetism, where the spins are arranged in a helical pattern, and occurs if  $|J'| < 3|J|$ . For this system, degenerate modes occur along lines in reciprocal space that are dependent on the value of  $J'$ . Similar macroscopic degeneracies are found in spin ice materials [20],[21],[51],[59],[50] and can often be lifted by thermal or quantum fluctuations through the mechanism of order-by-disorder in which states are selected from the ground state manifold by entropic forces [22],[23]. Such degeneracies can also be removed with the addition of further neighbor interactions or magnetic anisotropies [24],[25],[56],[57].

In this chapter, the sublattice numbering uses an ABC nomenclature as opposed to 1, 2 and 3 from Chap. 3 as shown in Fig. 5.1. The Hamiltonian from Eq. 3.1 is adapted to include  $J'$  when considering interactions between different

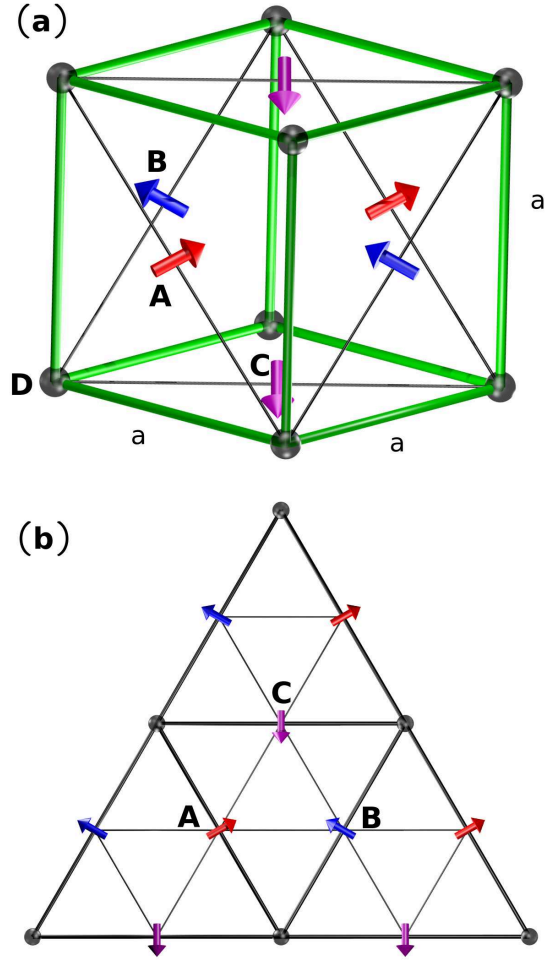


Figure 5.1: (a) The fcc lattice is divided into four cubic sublattices, each with lattice constant  $a$  and labeled as A, B, C, and D. The D sites (spheres) are non-magnetic whereas the remaining three sublattices (arrows) are magnetic. (b) The A, B, and C sites form a set of kagome lattices stacked along the (111) direction. Figure from Ref. [14], adapted from Ref. [6].

planes as

$$\mathcal{H} = J \sum_{i < j} \mathbf{S}_i \cdot \mathbf{S}_j + J' \sum_{i < j} \mathbf{S}_i \cdot \mathbf{S}_j - K \sum_{\gamma} \sum_{l \subset \gamma} (\mathbf{S}_l \cdot \hat{\mathbf{n}}_{\gamma})^2, \quad (5.1)$$

where  $J'$  is used here to show the transition from the 2D  $J' = 0$  kagome lattice to the 3D  $J' = J$  fcc case as explored in Sec. 5.3.

## 5.2 Spin Wave Theory

This section is based on notes from Prof. B. Southern (Univ. of Manitoba). In order to study the linearized spin wave excitations, a single domain in which the net magnetization is along the [111] direction is considered. The spins  $\mathbf{S}_i$  on each sublattice are transformed to local spin coordinates  $\tilde{\mathbf{S}}_i$  such that  $\tilde{S}_i^z = 1$  in the ground state. Plane wave solutions involving the transverse spin components  $\tilde{\mathbf{S}}_i = \tilde{\mathbf{S}} e^{i(\mathbf{k} \cdot \mathbf{r}_i - \omega t)}$  are desired. The linearized equations for the six transverse spin amplitudes can be obtained through the standard torque equation [60, 61] or other techniques [62] (see Chap. 2)

$$\frac{d\mathbf{S}}{dt} = (\mathbf{S} \times \mathbf{H}_{\text{eff}}), \quad (5.2)$$

where  $\mathbf{H}_{\text{eff}} = -\frac{\partial E}{\partial \mathbf{S}}$  is the field. Linearization of the torque equations with respect to this equation is required. One can also use the quantum equation of motion for the spin operators

$$i\hbar \frac{d\mathbf{S}}{dt} = [\mathbf{S}, \mathcal{H}], \quad (5.3)$$

where  $\mathcal{H}$  is the Hamiltonian and  $[,]$  is a commutator. The spin components satisfy  $[S_\alpha, S_\beta] = \epsilon_{\alpha\beta\gamma} \delta_\gamma i\hbar$ .

The simplest approach is to first transform the Hamiltonian from a crystal coordinate system to local spin coordinates  $\tilde{\mathbf{S}}_i$  using rotation matrices based on the  $q = 0$  spin structure. These rotation matrices are derived for each sublattice [15].

Writing the sublattice spin vectors as column vectors,

$$\mathbf{S}_A = \begin{pmatrix} \sqrt{2}\beta & 0 & \alpha \\ \alpha/\sqrt{2} & -1/\sqrt{2} & -\beta \\ \alpha/\sqrt{2} & 1/\sqrt{2} & -\beta \end{pmatrix} \tilde{\mathbf{S}}_A = \mathbf{M}_A \tilde{\mathbf{S}}_A, \quad (5.4)$$

$$\mathbf{S}_B = \begin{pmatrix} \alpha\sqrt{2} & 1/\sqrt{2} & -\beta \\ \sqrt{2}\beta & 0 & \alpha \\ \alpha/\sqrt{2} & -1/\sqrt{2} & -\beta \end{pmatrix} \tilde{\mathbf{S}}_B = \mathbf{M}_B \tilde{\mathbf{S}}_B, \quad (5.5)$$

$$\mathbf{S}_C = \begin{pmatrix} \alpha/\sqrt{2} & -1/\sqrt{2} & -\beta \\ \alpha/\sqrt{2} & 1/\sqrt{2} & -\beta \\ \sqrt{2}\beta & 0 & \alpha \end{pmatrix} \tilde{\mathbf{S}}_C = \mathbf{M}_C \tilde{\mathbf{S}}_C. \quad (5.6)$$

Here,  $\mathbf{S}_{ABC}$  are the spin coordinates in the reference frame of the crystal while  $\tilde{\mathbf{S}}_{ABC}$  are the local spin coordinates. These transformations preserve the spin length and the commutation relations.

In the crystal axes, the Hamiltonian can be expanded as

$$\begin{aligned} \mathcal{H} &= J \sum_{i<j} \mathbf{S}_i \cdot \mathbf{S}_j + J' \sum_{i<j} \mathbf{S}_i \cdot \mathbf{S}_j - K \sum_{\gamma} \sum_{l \subset \gamma} (\mathbf{S}_l \cdot \hat{\mathbf{n}}_{\gamma})^2 \\ &= J \sum_{i<j} [(\mathbf{S}_i^A \cdot \mathbf{S}_j^B) + (\mathbf{S}_i^B \cdot \mathbf{S}_j^C) + (\mathbf{S}_i^C \cdot \mathbf{S}_j^A)] \\ &\quad + J' \sum_{l<m} [(\mathbf{S}_l^A \cdot \mathbf{S}_m^B) + (\mathbf{S}_l^B \cdot \mathbf{S}_m^C) + (\mathbf{S}_l^C \cdot \mathbf{S}_m^A)] \\ &\quad - K \sum_i [(\mathbf{S}_{iA} \cdot \hat{\mathbf{n}}_A)^2 + (\mathbf{S}_{iB} \cdot \hat{\mathbf{n}}_B) + (\mathbf{S}_{iC} \cdot \hat{\mathbf{n}}_C)]. \end{aligned} \quad (5.7)$$

To transform the scalar product  $\mathbf{S}_A \cdot \mathbf{S}_B$  to local coordinates requires writing  $\mathbf{S}_A$

as a row vector and  $\mathbf{S}_B$  as a column vector

$$\mathbf{S}_A = \mathbf{M}_A \tilde{\mathbf{S}}_A, \quad (5.8)$$

$$\mathbf{S}_A^T = \tilde{\mathbf{S}}_A^T \mathbf{M}_A^T, \quad (5.9)$$

where  $T$  indicates transpose. Furthermore,

$$\begin{aligned} \mathbf{S}_A^T \cdot \mathbf{S}_B &= \tilde{\mathbf{S}}_A^T \mathbf{M}_A^T \mathbf{M}_B \tilde{\mathbf{S}}_B \\ &= \mathbf{S}_A^T \mathbf{\Lambda}_{AB} \tilde{\mathbf{S}}_B, \end{aligned} \quad (5.10)$$

where

$$\mathbf{\Lambda}_{AB} = \begin{pmatrix} 2\alpha\beta + \frac{\alpha^2}{2} & \beta - \alpha/2 & \frac{\alpha^2 - 2\beta^2 - \beta\alpha}{\sqrt{2}} \\ -\beta + \frac{\alpha}{2} & -\frac{1}{2} & -\frac{\alpha + \beta}{\sqrt{2}} \\ \frac{\alpha^2 - 2\beta^2 - \alpha\beta}{\sqrt{2}} & \frac{\alpha + \beta}{\sqrt{2}} & \beta^2 - 2\alpha\beta \end{pmatrix}. \quad (5.11)$$

A similar process is used for the other sublattice interactions and finds  $\mathbf{\Lambda}_{CA} = \mathbf{\Lambda}_{BC} = \mathbf{\Lambda}_{AB} = \mathbf{\Lambda}$ .

In addition,

$$\begin{aligned} -K S_{Ax}^2 &= -K \mathbf{S}_A^T \begin{pmatrix} 1 & 0 & 0 \\ 0 & 0 & 0 \\ 0 & 0 & 0 \end{pmatrix} \mathbf{S}_A \\ &= -K \tilde{\mathbf{S}}_A^T \mathbf{M}_A^T \begin{pmatrix} 1 & 0 & 0 \\ 0 & 0 & 0 \\ 0 & 0 & 0 \end{pmatrix} \mathbf{M}_A \tilde{\mathbf{S}}_A \\ &= -K \tilde{\mathbf{S}}_A^T \mathbf{W} \tilde{\mathbf{S}}_A, \end{aligned} \quad (5.12)$$

where

$$\mathbf{W} = \begin{pmatrix} 2\beta^2 & 0 & \sqrt{2}\beta\alpha \\ 0 & 0 & 0 \\ \sqrt{2}\beta\alpha & 0 & \alpha^2 \end{pmatrix}. \quad (5.13)$$

Similarly,

$$-KS_{By}^2 = -K\tilde{\mathbf{S}}_B^T \mathbf{W} \tilde{\mathbf{S}}_B, \quad (5.14)$$

$$-KS_{Cy}^2 = -K\tilde{\mathbf{S}}_C^T \mathbf{W} \tilde{\mathbf{S}}_C. \quad (5.15)$$

Hence, in local coordinates, the Hamiltonian is

$$\mathcal{H} = J \sum_{i<j} \tilde{\mathbf{S}}_i^T \Lambda \tilde{\mathbf{S}}_j + J' \sum_{i<j} \tilde{\mathbf{S}}_i^T \Lambda \tilde{\mathbf{S}}_j - K \sum_i \tilde{\mathbf{S}}_i^T \mathbf{W} \tilde{\mathbf{S}}_i. \quad (5.16)$$

The equation of motion for  $\tilde{S}_{ix}^A$  becomes

$$\begin{aligned} \frac{i\hbar \tilde{S}_{ix}^A}{dt} = [\tilde{S}_{ix}^A, \mathcal{H}] &= i\hbar J \sum_j \left[ (0, \tilde{S}_{iz}^A, -\tilde{S}_{iy}^A) \Lambda \begin{pmatrix} \tilde{S}_{jx}^B \\ \tilde{S}_{jy}^B \\ \tilde{S}_{jz}^B \end{pmatrix} + (\tilde{S}_{jx}^C, \tilde{S}_{jy}^C, \tilde{S}_{jz}^C) \Lambda \begin{pmatrix} 0 \\ \tilde{S}_{iz}^A \\ -\tilde{S}_{iy}^A \end{pmatrix} \right] \\ &+ \text{same terms for } J' \\ &- i\hbar K \left[ (0, \tilde{S}_{iz}^A, -\tilde{S}_{iy}^A) \mathbf{W} \begin{pmatrix} \tilde{S}_{ix}^A \\ \tilde{S}_{iy}^A \\ \tilde{S}_{iz}^A \end{pmatrix} + (\tilde{S}_{ix}^A, \tilde{S}_{iy}^A, \tilde{S}_{iz}^A) \mathbf{W} \begin{pmatrix} 0 \\ \tilde{S}_{iz}^A \\ -\tilde{S}_{iy}^A \end{pmatrix} \right]. \end{aligned} \quad (5.17)$$

Retaining terms linear in  $\tilde{S}_x, \tilde{S}_y$  and replacing  $\tilde{S}_z$  by 1,

$$\begin{aligned}
\frac{d\tilde{S}_{ix}^A}{dt} &= J \sum_j \left[ \left( \frac{\alpha}{2} - \beta \right) \tilde{S}_{jx}^B - \frac{1}{2} \tilde{S}_{jy}^B - (\beta^2 - 2\alpha\beta) \tilde{S}_{iy}^A \right. \\
&\quad \left. + \left( \beta - \frac{\alpha}{2} \right) \tilde{S}_{jx}^C - \frac{1}{2} \tilde{S}_{jy}^C - (\beta^2 - 2\alpha\beta) \tilde{S}_{iy}^A \right] \\
&\quad + \text{same terms for } J' \\
&\quad + K\alpha^2 \tilde{S}_{iy}^A + K\alpha^2 \tilde{S}_{iy}^A.
\end{aligned} \tag{5.18}$$

Now letting  $\tilde{S}_i = \sum_{\mathbf{q}} \tilde{S}_{\mathbf{q}} e^{i\mathbf{q}\cdot\mathbf{r}_i}$  on each sublattice,

$$\begin{aligned}
\frac{d\tilde{S}_{qx}^A}{dt} &= \left( \frac{\alpha}{2} - \beta \right) \lambda_{AB} \tilde{S}_{qx}^B - \frac{1}{2} \lambda_{AB} \tilde{S}_{qy}^B - 4(\beta^2 - 2\alpha\beta)(J + J') \tilde{S}_{qy}^A \\
&\quad + \left( \beta - \frac{\alpha}{2} \right) \lambda_{AC} \tilde{S}_{qx}^C - \frac{1}{2} \lambda_{AC} \tilde{S}_{qy}^C + 2K\alpha^2 \tilde{S}_{qy}^A \\
&= -Y_{AB} \tilde{S}_{qx}^B - Z_{AB} \tilde{S}_{qy}^B + Y_{AC} \tilde{S}_{qx}^C - Z_{AC} \tilde{S}_{qy}^C - X \tilde{S}_{qy}^A,
\end{aligned} \tag{5.19}$$

and so on for the other spin components. Eq. 5.19 combined with the similar equation for  $y$  and the ones for  $x$  and  $y$  on sites  $B$  and  $C$  give a system of linear equations which may be integrated to obtain  $\tilde{\mathbf{S}}^A(t), \tilde{\mathbf{S}}^B(t)$  and  $\tilde{\mathbf{S}}^C(t)$ . Assuming solutions of the form  $\tilde{\mathbf{S}}(t) = \tilde{\mathbf{S}} e^{i\omega t}$ , the following eigenvalue equation in the form of a 6x6 matrix  $\mathbf{\Gamma}$  for the allowed frequencies is obtained

$$-i\omega \begin{pmatrix} \tilde{S}_A^x \\ \tilde{S}_B^x \\ \tilde{S}_C^x \\ \tilde{S}_A^y \\ \tilde{S}_B^y \\ \tilde{S}_C^y \end{pmatrix} = \begin{pmatrix} 0 & Y_{AB} & -Y_{AC} & X & Z_{AB} & Z_{AC} \\ -Y_{AB} & 0 & Y_{BC} & Z_{AB} & X & Z_{BC} \\ Y_{AC} & -Y_{BC} & 0 & Z_{AC} & Z_{BC} & X \\ W & T_{AB} & T_{AC} & 0 & Y_{AB} & -Y_{AC} \\ T_{AB} & W & T_{BC} & -Y_{AB} & 0 & Y_{BC} \\ T_{AC} & T_{BC} & W & Y_{AC} & -Y_{BC} & 0 \end{pmatrix} \begin{pmatrix} \tilde{S}_A^x \\ \tilde{S}_B^x \\ \tilde{S}_C^x \\ \tilde{S}_A^y \\ \tilde{S}_B^y \\ \tilde{S}_C^y \end{pmatrix}, \quad (5.20)$$

where

$$\begin{aligned} X &= 4(J + J')(\beta - 2\alpha)\beta - 2K\alpha^2 \\ W &= 4(J + J')(2\alpha - \beta)\beta + 2K(\alpha^2 - 2\beta^2) \\ Y_{ij} &= (\beta - \alpha/2)\lambda_{ij} \\ Z_{ij} &= \lambda_{ij}/2 \\ T_{ij} &= (2\alpha\beta + \alpha^2/2)\lambda_{ij}, \end{aligned} \quad (5.21)$$

and

$$\begin{aligned} \lambda_{AB} &= 2J \cos\left(\left(k_x - k_y\right)\frac{a}{2}\right) + 2J' \cos\left(\left(k_x + k_y\right)\frac{a}{2}\right) \\ \lambda_{BC} &= 2J \cos\left(\left(k_x - k_z\right)\frac{a}{2}\right) + 2J' \cos\left(\left(k_x + k_z\right)\frac{a}{2}\right) \\ \lambda_{AC} &= 2J \cos\left(\left(k_y - k_z\right)\frac{a}{2}\right) + 2J' \cos\left(\left(k_y + k_z\right)\frac{a}{2}\right). \end{aligned} \quad (5.22)$$

The wavevector components  $k_x, k_y, k_z$  are defined with respect to the cubic axes with lattice constant  $a$ . The linearized equations yield six real eigenvalues  $\pm\omega_1, \pm\omega_2, \pm\omega_3$ , although it should be noted that the corresponding eigenvectors associated with each pair  $\pm\omega_n$ , while linearly independent, are not orthogonal. While in the gen-

eral case the eigenvalues and the corresponding eigenvectors must be obtained numerically, analytical results can be determined in special cases.

Note that this matrix has a sign difference from that given in Ref. [14] due to a lack of minus sign in the torque equation, but it does not change the value of pairs of  $\pm\omega$ .

## 5.3 Spin Wave Analysis

### 5.3.1 Zero Anisotropy

For  $K = 0$ , the ground state is the (111) planar spin configuration with the three sublattices oriented at  $120^\circ$  with respect to each other. In this case the problem can be reduced to finding the eigenvalues  $\omega^2$  of a  $3 \times 3$  symmetric matrix

$$\begin{pmatrix} A_1 & B_1 & B_2 \\ B_1 & A_2 & B_3 \\ B_2 & B_3 & A_3 \end{pmatrix}, \quad (5.23)$$

where

$$\begin{aligned} A_1 &= 4(J + J')^2 - (\lambda_{AB}^2 + \lambda_{AC}^2)/2 \\ A_2 &= 4(J + J')^2 - (\lambda_{AB}^2 + \lambda_{BC}^2)/2 \\ A_3 &= 4(J + J')^2 - (\lambda_{AC}^2 + \lambda_{BC}^2)/2 \\ B_1 &= (J + J')\lambda_{AB} - \lambda_{AC}\lambda_{BC}/2 \\ B_2 &= (J + J')\lambda_{AC} - \lambda_{AB}\lambda_{BC}/2 \\ B_3 &= (J + J')\lambda_{BC} - \lambda_{AB}\lambda_{AC}/2. \end{aligned} \quad (5.24)$$

If the interplane coupling  $J'$  is also zero (the 2D case), the  $\lambda_{ij}$  satisfy the following relation for arbitrary values of the wavevector  $\mathbf{k}$

$$\lambda_{AB}^2 + \lambda_{BC}^2 + \lambda_{AC}^2 = 4J^2 + \lambda_{AB}\lambda_{BC}\lambda_{AC}/J. \quad (5.25)$$

The characteristic cubic equation has a zero eigenvalue for all  $\mathbf{k}$  and the remaining two eigenvalues are degenerate and given by the following expressions

$$\begin{aligned} \omega_1 &= 0 \\ \omega_{2,3} &= \sqrt{2}J\{\sin[(k_x - k_y)a/2]^2 + \sin[(k_x - k_z)a/2]^2 \\ &\quad + \sin[(k_y - k_z)a/2]^2\}^{1/2}, \end{aligned} \quad (5.26)$$

where the wavevector components  $k_x, k_y, k_z$  are defined with respect to the cubic axes with lattice constant  $a$ . These expressions agree with previous results [15] for the 2D NN  $q = 0$  kagome spin lattice when  $a = \sqrt{2}$  (corresponding to a NN distance of unity). The dispersionless mode is related to the local rotations of the spins from one ground state to another. Note that for  $k_x = k_y = k_z$  all three modes are dispersionless. The latter case corresponds to the fact that the decoupled kagome planes can have arbitrary uniform rotations with respect to one another. For  $\mathbf{k}$  along one of the cube axes, Eq. 5.26 reduces to  $\omega_2 = \omega_3 = 2J|\sin(ka/2)|$ .

When the interplane interaction  $J' > 0$ , the cubic characteristic equation again factors if any two of the  $\lambda_{ij}$  are equal, such as when  $k_y = k_z$ . In this particular case,  $A_1 = A_3$  and  $B_1 = B_3$  and the eigenvalues are

$$\begin{aligned} \omega_1^2 &= A_1 - B_2 \\ \omega_{2,3}^2 &= \frac{A_1 + A_2 + B_2}{2} \pm \frac{\sqrt{(A_1 - A_2 + B_2)^2 + 8B_1^2}}{2}. \end{aligned} \quad (5.27)$$

Similar expressions can be obtained for  $k_x = k_y$  or  $k_x = k_z$ . In general, all three modes are dispersive and non-degenerate when  $J' > 0$ . However, there are two special cases where degeneracy occurs and where zero frequency modes are present.

For  $k_x = k_y = k_z$ , analysis shows that

$$\begin{aligned}\omega_1^2 = \omega_3^2 &= [1 - \cos(k_x a)][4J'^2 + 6JJ' + 2J'^2 \cos(k_x a)] \\ \omega_2^2 &= [1 - \cos(k_x a)][4J'^2 + 12JJ' + 8J'^2 \cos(k_x a)].\end{aligned}\tag{5.28}$$

All three modes are dispersive due to the coupling between kagome planes and two are degenerate. However, note that  $\omega_2$  becomes zero at the zone boundary  $k_x = \pi/a$  when  $J' = 3J$ . For values of the inter-plane coupling  $J' > 3J$  the ground state is no longer the  $q = 0$  kagome state but rather corresponds to ferromagnetic kagome planes which are ordered antiferromagnetically with respect to each other. Here, a constraint of  $J' < 3J$  is applied.

In the second special case,  $k_y = k_z = 0$ , which corresponds to spin waves propagating parallel to one of the cubic crystal axes,

$$\begin{aligned}\omega_1 &= 0 \\ \omega_2 = \omega_3 &= 2(J + J')|\sin(ka/2)|,\end{aligned}\tag{5.29}$$

where  $k$  represents  $k_x, k_y$ , or  $k_z$ . These expressions reduce to the correct 2D result above when  $J' = 0$ . Hence, the coupling of the planes stiffens the excitations for wavevectors along the crystal axes but does not remove the zero frequency mode.

The zero mode can be understood from Fig. 5.1. The  $x = na$  planes only have B sites whereas the  $x = (n + 1/2)a$  planes have both A and C sites where  $n = 0, 1, 2, \dots$ . In the ground state the A and C sublattices are at  $120^\circ$  to each other and to the B sublattice. The entire plane of AC spins can be rotated continuously

about the direction of the B sublattice spins in the planes on either side with no change in energy. In addition, these rotations in each of the AC planes are independent and correspond to a set of localized excitations for  $J + J' > 0$ . When  $J' = 0$ , there are additional degeneracies which lead to a zero energy mode [15] for all  $\mathbf{k}$ .

### 5.3.2 Effects of Anisotropy

In the general case with  $K > 0$ , the spin wave frequencies can only be obtained numerically. The ground state is no longer a planar configuration and the continuous degeneracies are removed and there are no zero modes. For values of  $\mathbf{k}$  along the cubic axes, the lowest mode is almost dispersionless while the other two modes have strong dispersion. In all other wavevector directions, all three modes have strong dispersion. Fig. 5.2 shows the spin wave frequencies  $\omega$  along the  $\Gamma X(100)$  and  $\Gamma R(111)$  directions for different values of the inter-plane coupling  $J'$  and the cubic anisotropy  $K$ . For  $K = 0$ , the effect of  $J'$  is to stiffen the frequencies along  $\Gamma X$  and to remove the zero modes along  $\Gamma R$ . For  $K > 0$ , the zero modes along both  $\Gamma X$  and  $\Gamma R$  now have a substantial gap. Along the  $\Gamma X$  direction, there is a low frequency mode which is almost dispersionless (similar to the mode reported in Ref. [24]). Based on electronic structure calculations [37], the case  $K = 0.1J$  with  $J' = J$  best represents  $\text{IrMn}_3$ . As shown in the next section, there is a strong dependence of the inelastic scattering intensity on wave vector.

At the zone center  $\mathbf{k} = \mathbf{0}$  the leading behavior of the three positive frequencies

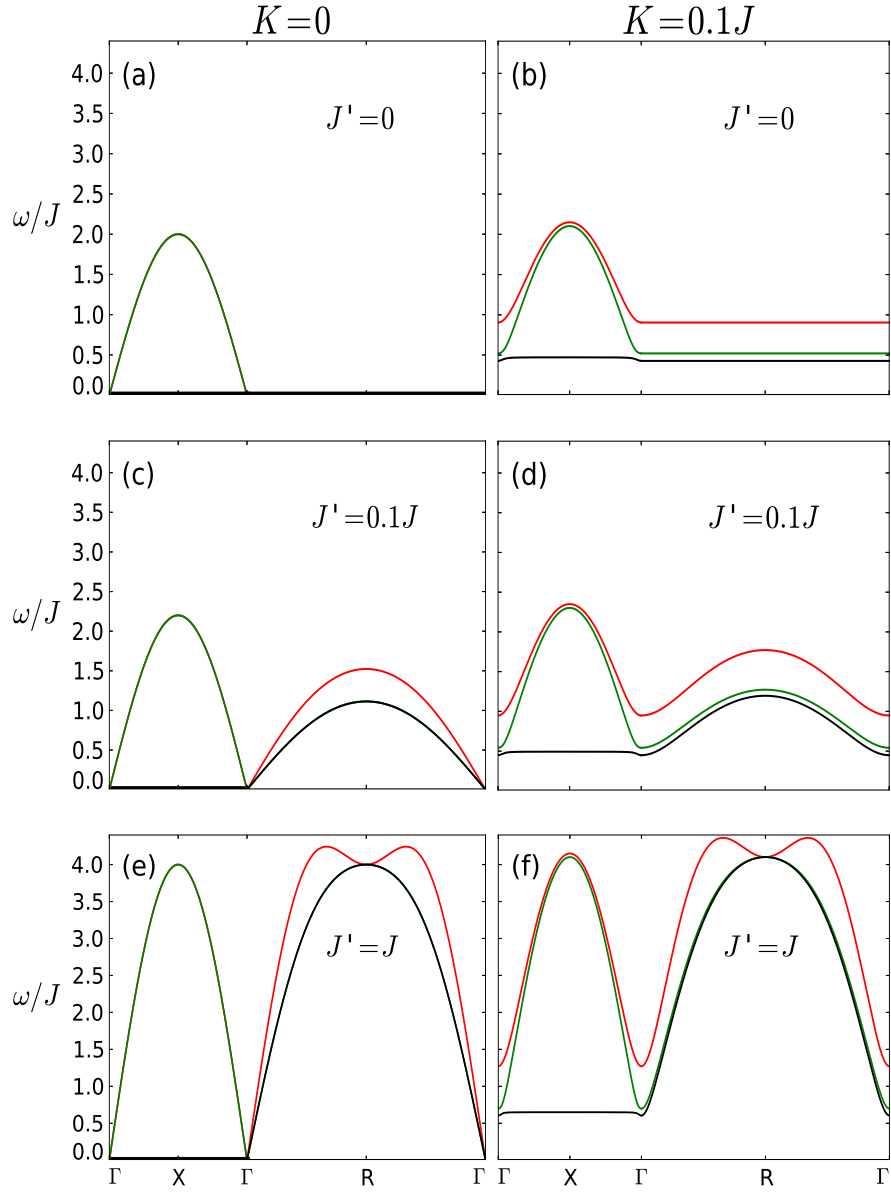


Figure 5.2: Spin wave modes along the  $\Gamma X$  and  $\Gamma R$  directions (a)  $K = 0, J' = 0$ , (b)  $K = 0.1J, J' = 0$ , (c)  $K = 0, J' = 0.1J$ , (d)  $K = 0.1J, J' = 0.1J$ , (e)  $K = 0, J' = J$ , (f)  $K = 0.1J, J' = J$  [14].

as a function of  $K$  is obtained

$$\begin{aligned} \omega_1 \simeq \omega_2 &\simeq \sqrt{2(J + J')K} \\ \omega_3 &\simeq 2\sqrt{2(J + J')K}. \end{aligned} \tag{5.30}$$

As such, all modes have a gap for  $K > 0$  and although  $\omega_1, \omega_2$  are degenerate to leading order in  $K$ , they become nondegenerate as  $K$  increases. At the point R ( $k_x = k_y = k_z = \pi/a$ ) and with  $J' = J$ , all three modes are degenerate for all  $K$ .

In the MC simulations of the Chap. 3, the sublattice magnetizations did not saturate at low  $T$  and displayed evidence of degenerate spin configurations at  $T = 0$  for values of  $K/J$  smaller than  $\sim 0.06$ . This behavior is consistent with the presence of a small gap in the excitation spectrum. As  $K$  increases, the gap increases and the sublattices become fully saturated as  $T = 0$  is approached.

### 5.3.3 Summary

The results above have demonstrated that the fcc kagome antiferromagnet is an example of the relatively rare phenomenon of macroscopic continuous degeneracy in 3D that gives rise to zero energy spin wave modes. Local cubic anisotropy is found to remove this degeneracy and introduce a gap in the spectrum. The lowest mode at small  $K$  is almost dispersionless and has energy  $\omega \sim 2\sqrt{JK}$  when  $J' = J$ , which is about  $0.63J$ , assuming  $K/J \approx 0.1$ . The electronic structure calculations [37] on  $\text{IrMn}_3$  provide the estimate  $J \sim 40$  meV giving  $\omega \sim 25$  meV. Other more exotic quantum effects are not anticipated and as such the  $S$  spin quantum number as studied in quantum calculations [62] is omitted from these results. While anisotropy did not show a strong effect in elastic scattering results from Chap. 4, it does induce a uniform magnetization in the [111] direction which could be utilized to stabilize a single-domain sample using field cooling techniques to better facilitate observation of these effects with inelastic neutron scattering experiments. These results support earlier MC simulations which suggest that, in the absence of anisotropy, critical fluctuations drive the phase transition to be

discontinuous, but that it becomes continuous with the addition of anisotropy due to the removal of degeneracies. The link between such removal of degeneracy in geometrically frustrated spin systems through anisotropic interactions, the nature of the phase transition to long-range order, and magnetic excitations, has recently been established in the pyrochlore antiferromagnet  $\text{Er}_2\text{Ti}_2\text{O}_7$  [50] (as noted in Chap. 3). Degeneracies are known to give rise to critical fluctuations which can drive a phase transition that is continuous within mean field theory to be first-order [47], [63]. In the present system, the introduction of an energy gap in the spin wave spectrum due to the addition of local cubic anisotropy suppresses the low-energy excitations responsible for the critical fluctuations near the Néel temperature.

## 5.4 Inelastic Scattering - Spin Wave Theory

The ORNL results carried out on powdered ordered samples were analyzed using inelastic magnetic neutron scattering. To compare them to theory, the following analysis, first for single crystal and then for powder, is carried out. While the spin wave overview of this chapter examines  $\omega$  using torque equations, more analysis is needed to develop a theory of inelastic magnetic scattering intensity.

The relevant parts of the scattering cross section for inelastic magnetic scattering are given as [44]

$$\left( \frac{d^2\sigma}{d\Omega dE'} \right)_{\text{inel}} \propto \frac{k'}{k} F(\boldsymbol{\kappa})^2 S(\boldsymbol{\kappa}, \omega), \quad (5.31)$$

where  $F(\boldsymbol{\kappa})$  is the form factor and  $S(\boldsymbol{\kappa}, \omega)$  is the dynamic structure factor. The development in Appendix A.3 reviews the derivation of the dynamic structure factor in terms of the retarded Green's function  $G^{\alpha\beta}(\boldsymbol{\kappa}, t) = -i\theta(t) \langle [S_{\boldsymbol{\kappa}}^{\alpha}(t), S_{-\boldsymbol{\kappa}}^{\beta}(0)] \rangle$ .

It is also shown how the previous analysis used to identify the eigenvectors and the associated eigenvalues can be generalized to calculate the retarded Green's function in the linearized spin wave approximation.

### 5.4.1 Neutron Scattering for Single Crystals

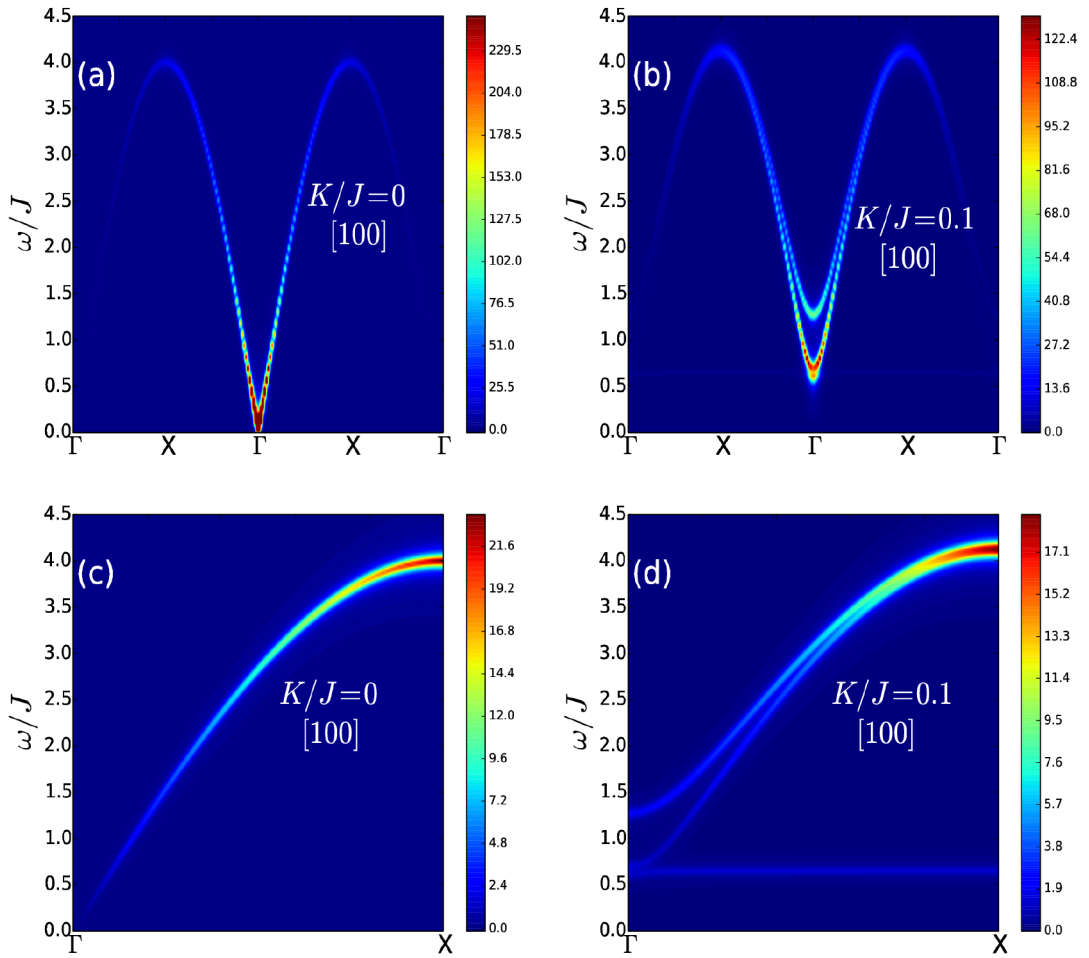


Figure 5.3: Relative magnitude of the inelastic scattering function  $S(\boldsymbol{\kappa}, \omega)$  (side bar scale) assuming a single magnetic (111) domain with  $J = J' = 1$  with  $\boldsymbol{\kappa} \parallel [100]$ . (a)  $K=0$ , (b)  $K/J=0.1$ , (c)  $K=0$  over a smaller region than (a), and (d)  $K/J=0.1$  over a smaller region than (b) [14].

Fig. 5.3 shows  $S(\boldsymbol{\kappa}, \omega)$  calculated with the assumption of a single magnetic

(111) domain at fixed values of  $\kappa$  along [100] directions with  $J = J' = 1$  for both  $K = 0$  and  $K/J = 0.1$ . The wave vector is allowed to extend beyond the first zone boundary for Fig. 5.3(a) and Fig. 5.3(b), but is restricted to be in the first zone for Fig. 5.3(c) and Fig. 5.3(d). In Fig. 5.3(a) and Fig. 5.3(b), the intensity is very large at the wave vectors corresponding to the elastic peaks with  $h, k, l$  not all even or odd, but the scale is such that the smaller wave vector modes (which can be seen in Fig. 5.3(c) and Fig. 5.3(d)) are not visible due to the large intensity near the elastic peaks located at  $h = 1, k = l = 0$ . The flat mode is clearly visible in Fig. 5.3(d) on the smaller scale but has an intensity much reduced from the other modes at the zone boundary. Fig. 5.3 can be compared with Figs. 5.2(e) and (f), illustrating the appearance of the low frequency mode along  $\Gamma X$  and the splitting of the degeneracy of the higher frequency modes. While the [111] direction ( $\Gamma R$ ) is not shown, the intensity is on the order of a hundred times smaller than the [100] direction.

Of particular note for all of the results shown in Fig. 5.3 is that the intensity is expected to be relatively small in the first Brillouin zone but is substantially larger in the second zone. On comparing panels (a) and (c) with (b) and (d), the impact of the anisotropy on the calculated spectrum is very strong.

## 5.4.2 Powder Averaging

### Average Over Angles

For powder samples as used in the Oak Ridge experiments, it is necessary to average  $S(\kappa, \omega)$  over crystalline orientations, or angles. The average over angles

can be calculated directly with

$$S(\kappa, \omega) = \int_{\phi=0}^{2\pi} \int_{\theta=0}^{\pi} S(\boldsymbol{\kappa}, \omega) \sin \theta d\theta d\phi, \quad (5.32)$$

which can be solved through Monte Carlo integration using, with  $r^1$  and  $r^2$  two random numbers from 0 to 1 and  $n$  the number of iteration steps,

$$S(\kappa, \omega) = \frac{1}{n} \sum_{i=1}^n S(\kappa, \arccos(2r_i^1 - 1), 2\pi r_i^2, \omega). \quad (5.33)$$

### Experimental Range

While the wavevector  $\boldsymbol{\kappa} = \mathbf{k} - \mathbf{k}'$  is used when describing the system from a theoretical point a view,  $\mathbf{Q} = \mathbf{k}_i - \mathbf{k}_f$  is often employed in experiments instead to represent the change between the initial and final states with the notation  $Q$ . Furthermore,  $\omega$  is related through the energy  $E$  by the relation  $E = \frac{\hbar^2 Q^2}{2m} = \hbar\omega$ . While they represent the same concepts, they are described here in this method to maintain consistency with conventional experimental naming systems.

In these experiments, there is a relation between  $Q$  and  $E$  such that certain regions are not accessible. Here a derivation of the upper and lower bounds for  $Q$  versus  $E$  is shown. Conservation of momentum gives

$$\mathbf{Q} = \mathbf{k}_i - \mathbf{k}_f, \quad (5.34)$$

whereas conservation of energy requires that the measured energy of the scattered neutron satisfy

$$E = E_i - E_f. \quad (5.35)$$

Here, the initial energy of the neutron is

$$E_i = \frac{\hbar^2 k_i^2}{2M_n}, \quad (5.36)$$

with  $M_n$  the neutron mass. It is possible to write

$$\frac{E_f}{E_i} = 1 - \frac{E}{E_i} = \left( \frac{k_f}{k_i} \right)^2. \quad (5.37)$$

Now, the scattered wavevector  $\mathbf{Q} = \mathbf{k}_i - \mathbf{k}_f$  satisfies

$$Q^2 = k_i^2 + k_f^2 - 2k_i k_f \cos(\theta), \quad (5.38)$$

where  $\theta$  is the scattering angle. Rearranging this gives

$$(Q/k_i)^2 = 1 + 1 - E/E_i - 2\sqrt{1 - E/E_i} \cos(\theta). \quad (5.39)$$

Since  $E_i = \frac{\hbar^2}{2M_n} k_i^2 = (2.072 \text{ meV } \text{\AA}^2) k_i^2 = L k_i^2$  with  $L = \frac{\hbar^2}{2M_n} \approx 2.072 \text{ meV } \text{\AA}^2$ , it can be written that

$$Q = \sqrt{\frac{E_i}{L} (2 - E/E_i - 2\sqrt{1 - E/E_i} \cos(\theta))}, \quad (5.40)$$

where  $E, E_i$  are in meV and  $Q$  is in  $\text{\AA}^{-1}$ .

The Oak Ridge results for  $\text{IrMn}_3$  has a maximum scattering angle around  $\theta = 60^\circ$ . Thus, for a given  $E, E_i$ ,  $Q_1 \leq Q \leq Q_2$  can be used with

$$Q_1 = \sqrt{\frac{E_i}{L} (2 - E/E_i - 2\sqrt{1 - E/E_i})}, \quad (5.41)$$

and

$$Q_2 = \sqrt{\frac{E_i}{L}(2 - E/E_i - \sqrt{1 - E/E_i})}. \quad (5.42)$$

This relation can be seen in Fig. 5.4 for  $E_i = 50$  meV and  $E_i = 100$  meV, two values that were used experimentally.

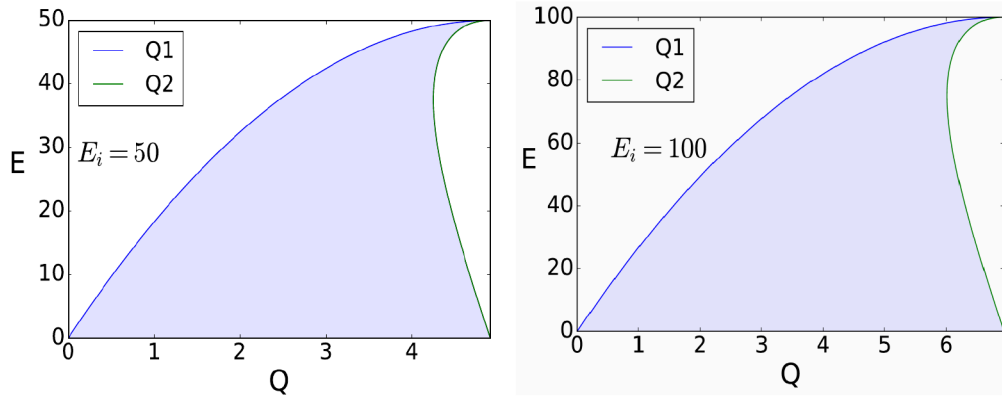


Figure 5.4: Boundaries for  $Q_1$  and  $Q_2$  showing the (shaded) accessible range for  $E_i = 50$  and 100 meV.

## Predicted Powder Results

In Sec. 5.4.1, the case of single crystals was considered. Here, Fig. 5.5 shows simulated powdered results for  $S(Q, \omega)$  without the form factor or  $k_f/k_i$  terms in Eq. 5.31. It shows the cases of  $K = 0$  and  $K = 0.1J$  and is a straightforward implementation of the previous theory (without experimental borders). The top figures show a full  $\omega$  range, while the bottom figures show a zoomed in version vertically and expanded horizontal cutoff.

The figures show the effect of anisotropy through a low energy gap of around  $0.6 \omega/J$ . Peaks appear at  $Q = 2\pi/a$  and  $Q = 2\pi\sqrt{5}/a$  corresponding to the [100] and [210] directions.

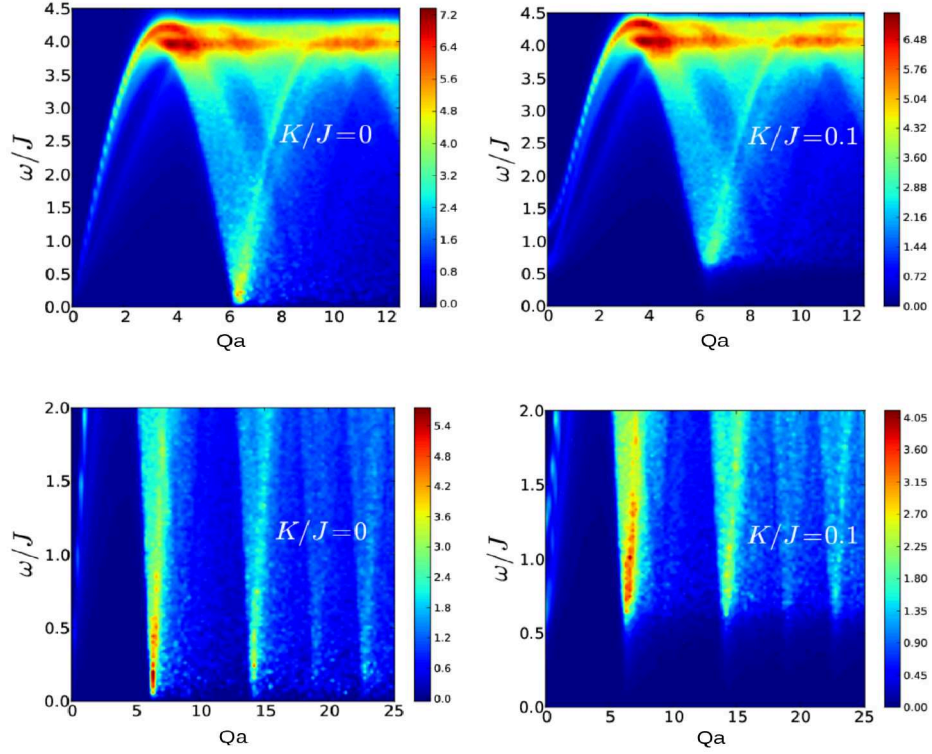


Figure 5.5: Calculated powder averaged inelastic intensity. Value of  $K$  included in the graphs. Different regions shown for  $K = 0$  and  $K = 0.1$ . Points of interest at  $2\pi$ ,  $2\pi\sqrt{5}$ ,  $2\pi\sqrt{9} = 2\pi \cdot 3$  and  $2\pi\sqrt{13}$ . Lower panels show details of the lower energy and also higher  $Q$  regions.

Fig. 5.6 shows the expected powder results using  $J = J' = 20$  meV,  $K = 2$  meV, and an incident energy of 100 meV. This  $J$  differs from the one calculated in Ref. [37] by a factor of 2 due to normalization. It shows what might be expected for an experimental setup with an appropriate experimental range for powder results using the developed model of inelastic neutron scattering for  $\text{IrMn}_3$ . Two main vertical sections are identified as the ordered peak locations corresponding to  $[100]$  and  $[210]$ , but not  $[110]$  as predicted, with a low energy gap caused by anisotropy.

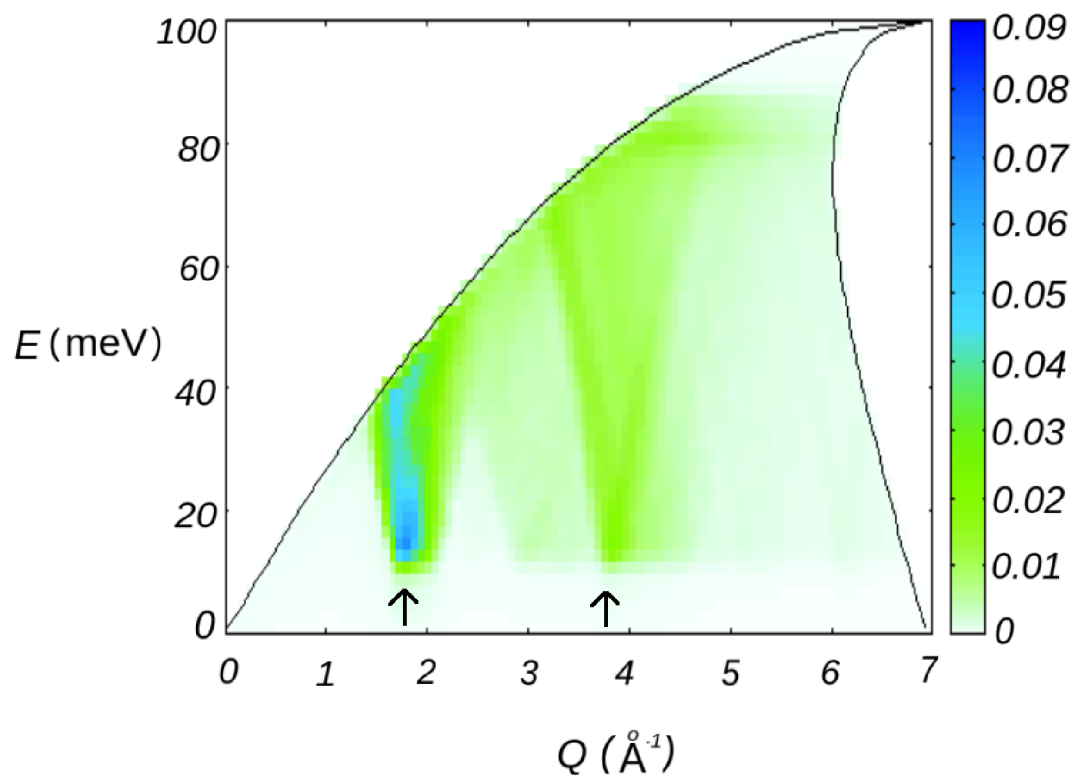


Figure 5.6: Calculated powder inelastic results showing  $E$  vs  $Q$  for an initial energy  $E_i = 100$  meV. Arrows point to the locations corresponding to  $[100]$  and  $[210]$  around  $Q = 1.67 \text{ \AA}^{-1}$  and  $3.75 \text{ \AA}^{-1}$  respectively, showing thick vertical bands. An expected band corresponding to  $[110]$  around  $Q = 2.37 \text{ \AA}^{-1}$  does not appear. Color corresponds to intensity (arbitrary units). Figure provided by Prof. B. Southern (Univ. of Manitoba).

### 5.4.3 Oak Ridge Results

An example of the inelastic results obtained at Oak Ridge is shown for a temperature of 5 K and an incident energy  $E_i = 100$  meV in Fig. 5.7. A subtraction of aluminum intensity (due to the sample holder) using Oak Ridge software with a fitting parameter was performed, but proves problematic as there is still considerable contribution remaining in regions of interest. Other incident energies such as  $E_i = 50$  meV and  $E_i = 200$  meV were used, but proved to give less useful results.

The intensity is shown as the color for different energy transfer (vertical axis) and scattering vector  $Q$  values (horizontal axis). As can be seen, there remains a strong intensity from the aluminum despite the subtraction at lower energy transfers which makes a quantitative analysis difficult. There are lighter bands corresponding to  $Q$  values at ordered peak positions that might correspond to an effect of the anisotropy. An elastic cut of the inelastic data around  $E = 0$  is provided in Appendix A.4, which shows more clearly the peak locations.

Comparing these experimental results in Fig. 5.7 to the results given by the predicted model in Fig. 5.6 proves difficult in large part because of background effects. The energy gap caused by anisotropy cannot be seen due to this low energy noise. Using a value of  $a = 3.75$  Å, ordered peak locations for [100], [110] and [210] correspond to  $Q = 1.67$  Å<sup>-1</sup>,  $2.37$  Å<sup>-1</sup> and  $3.75$  Å<sup>-1</sup>. The lighter vertical bands seen in Fig. 5.7 correspond to these ordered peak locations, although the lower  $Q$  peak is mostly hidden by the limitation of the experimental setup at this incident energy, but quantitative results proved difficult to obtain. Selected single crystal theory results, given in Appendix A.5 show that for the [110] direction there should be significant scattering, but in the powder average theory results of Fig. 5.6 there is no vertical band around [110], which is puzzling. A minor contribution from the

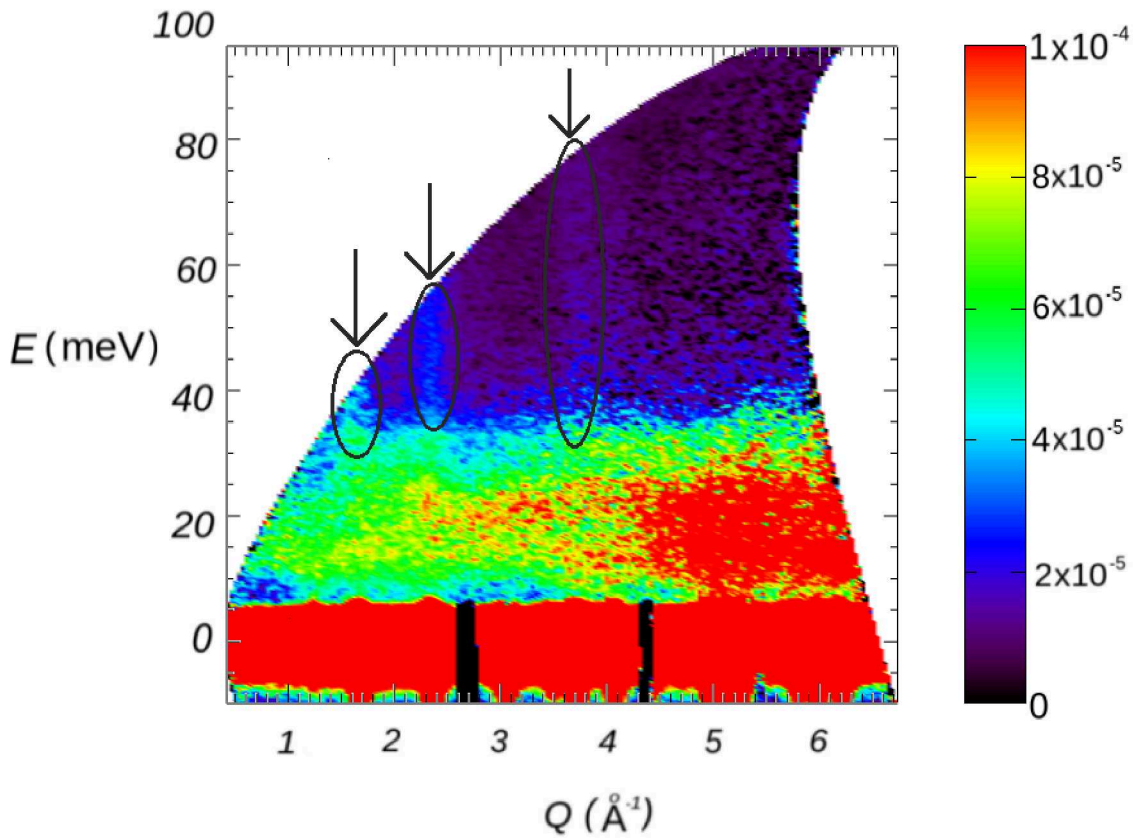


Figure 5.7: Experimental inelastic scattering results at  $T = 5$  K with an incident energy of 100 meV with the color representing intensity (arbitrary units). Imperfect aluminum intensity subtraction has been done which leads to negative (set to zero) black regions and the colorful red, yellow and green sections towards the bottom. Arrows point to the locations corresponding to [100], [110] and [210] around  $Q = 1.67 \text{ \AA}^{-1}$ ,  $2.36 \text{ \AA}^{-1}$  and  $3.75 \text{ \AA}^{-1}$  respectively, showing visible vertical bands.

[111] direction is also seen from these single crystal results, though it is too faint to clearly see in the corresponding powder results. It is not clear why there would be such a [111] contribution.

Other factors that contribute to the difficulty of analyzing the results include the fact that there is always a significant nuclear scattering component at every wavevector that contains a magnetic scattering component since the magnetic

order is of the  $q = 0$  type. Ideally, experiments at temperatures above  $T_N = 960$  K would be made to separate these components, but it was not possible to achieve such high temperatures in the experimental setup. The quality of the data also made it difficult to make direct comparisons on relative peak heights which can be used to distinguish nuclear and magnetic scattering [6]. It would be far more useful to have single crystal samples results to compare with the theory.

# Chapter 6

## Discussion and Conclusions

Several approaches are presented in this study of the magnetic structure of the fcc kagome model used to describe  $\text{IrMn}_3$ . Monte Carlo simulations, spin wave calculations and magnetic neutron scattering experiments are the primary focus of this thesis. Various quantities and consequences of adding anisotropy to the 3D Heisenberg model of the fcc kagome using the Monte Carlo method are studied, such as the ground state, the transition temperature  $T_N$ , energy histograms and cumulants to determine the order of the phase transition. A spin wave model is constructed to analyze any effects of a non-zero anisotropy. Building upon the 2D kagome model, elastic and inelastic scattering predictions are made for the 3D fcc kagome model. The inelastic results are adapted to account for a powder sample, as the experiment conducted on  $\text{IrMn}_3$  as part of this research used such samples. A background signal from the sample holder proved to cause significant noise in the experimental results which render comparison to theory less than ideal.

## 6.1 Monte Carlo Simulations

In Chap. 3, a detailed study of the effect of anisotropy on the fcc kagome lattice through Monte Carlo simulations is described. This work builds upon a previous study of the same model without anisotropy [12]. When  $K = 0$ , it is found that the system undergoes a first-order phase transition at the Néel temperature  $T_N = 0.476J$ . Furthermore, a macroscopic ground state degeneracy associated with interchanging the direction of two sub-lattice spins in planes in the fcc kagome lattice is discussed.

With the addition of anisotropy, this degeneracy in the ground state is broken and new discrete ones are formed. Spins are locked to a particular (111) plane, giving rise to eight possible ground state spin configurations per value of  $K$ . In theory, any nonzero value of  $K$  locks the spins in these ground states. In these Monte Carlo simulations, a finite system size must be used which causes finite size effects. It is found that  $K \gtrsim 0.06$  is needed to cause the system sublattice magnetization order parameter to saturate as  $T$  approached zero. In studying the effects of varying  $K$ ,  $T_N$  is found to first increase, then to decrease, as expected. For large values of  $K$ , the uniaxial anisotropy dominates and a broad maximum in the specific heat is seen due to the onset of short-range correlations. The anisotropy also cants the spins out of the (111) plane, inducing a ferromagnetic magnetization. Comparisons with expected spin angle deviations from the  $120^\circ$  structure at  $T = 0$  proved useful to explain the effects of  $K$  on the ground state. Unlike the first-order phase transition observed in the  $K = 0$  case, a continuous phase transition is determined to describe the anisotropic system using energy histograms and cumulants. This change in the order of the transition is believed to be associated with the removal of the macroscopic degeneracy of  $K = 0$ . The

development of a finite magnetic moment along the [111] direction as a consequence of anisotropy along with the expected in-plane canting of the spins on the top layer of the antiferromagnet in the presence of a ferromagnetic layer [11] are expected to be important to describe the exchange bias seen in IrMn<sub>3</sub>.

## 6.2 Elastic Neutron Scattering

Chap. 4 provides an overview of elastic magnetic scattering for the fcc kagome lattice with a focus on the effects of anisotropy. Starting from the fundamentals of magnetic scattering theory, the structure factor, both nuclear and magnetic, is developed specifically for IrMn<sub>3</sub>. The nuclear structure factor, published initially in [6], proves problematic as there is an accidental nearly exact cancellation of the structure factor for certain values of  $(h, k, l)$ , which makes it difficult to differentiate nuclear and magnetic peaks. Calculating the magnetic elastic cross section, using the magnetic form factor and magnetic structure factor, different peak height differences are obtained and tabulated. The effect of anisotropy is studied, but found to be minimal for the relevant value of  $K = 0.1J$  expected of IrMn<sub>3</sub>. Even using a high value of  $K = 5J$  shows only a small effect on the peak height and it is concluded that inelastic scattering should provide a stronger indication of the effect of anisotropy.

## 6.3 Spin Waves and Inelastic Neutron Scattering

Chap. 5 gives a somewhat elaborate development of spin waves and their use in inelastic magnetic scattering for IrMn<sub>3</sub>. A spin wave theory is developed for the kagome fcc antiferromagnet that shows the effect of anisotropy. Starting from a

ground state spin configuration, the Hamiltonian is developed to obtain a  $6 \times 6$  matrix that describes the motion of the three sublattice spins in  $x$  and  $y$  coordinates. An analysis of the zero anisotropy case confirms several extrapolated modes, with a zero-energy mode seen along certain directions (in contrast with the 2D case where this mode is zero for all directions) This difference between the 2D and 3D cases is a reflection of the reduction of degeneracy when kagome planes are coupled in a fcc structure. By including the anisotropy, this mode is raised as a function of the anisotropy strength, a consequence of the further reduction in degeneracy. The effects of this zero-energy mode is seen in Monte Carlo simulations where the sublattices do not fully saturate until a sufficiently large value of  $K$  is used. Such dynamics are linked to the change in order of the phase transition.

These spin wave calculations are used as the basis for the magnetic inelastic scattering theory. The scattering cross section depends mostly on the dynamic structure factor  $S(\boldsymbol{\kappa}, \omega)$ . This is derived using a Green's function approach, making use of the previous spin wave theory results, namely the  $6 \times 6$  matrix describing how the spins behave on the different sublattices with time. Analysis of a single crystal model shows the anticipated zero mode being raised with the anisotropy. To make direct comparisons with the experimental samples, the single crystal results must be averaged over all scattering angles, which is done through Monte Carlo simulations. Expected powder results for  $\text{IrMn}_3$  are calculated and shown.

An attempt is then made to compare these results to the experimental results of Fig. 5.7 obtained at ORNL. However, these experimental results exhibit a considerable amount of noise in the data due to the background aluminum sample holder which makes finding an elevated low energy mode, if anisotropy is present, difficult. There is also a possibility of a strong signal from single crystals along a

certain direction being kept in the experimental powder sample. Almost vertical bands of higher intensity are seen that correspond to several ordered peak locations expected from the scattering theory. The band corresponding to [110] is not seen in the theoretical powder results, but is present in both the single crystal theoretical calculations and the experimental results. Appendix A.5 also shows that a small scattering is seen for the [111] direction that is unexpected. The reason for these remains unclear.

## 6.4 Future Areas of Study

There still remains several unanswered questions in the study of  $\text{IrMn}_3$  using these methods or otherwise. The effect of next NN interactions could help elaborate on some of the spin wave and inelastic behavior of the system. Experimental verification of the presence of ferromagnetism in the bulk or thin-film ordered phase  $\text{IrMn}_3$  and related compounds is desirable.

Monte Carlo simulations of thin films of the fcc kagome structure have been performed [64] where a surface anisotropy is considered. When this surface anisotropy is sufficiently large, a net magnetization directed perpendicular to the film develops. This study could be extended to also include exchange coupling to a ferromagnetic layer as well as including dipole coupling within and between surface layers to provide a realistic atomic-level model of exchange bias. The model used in the present work can also serve as the foundation for further study of excitations associated with thin films of  $\text{IrMn}_3$ . Such results could be useful in an examination of dynamic effects in exchange bias phenomena.

There is also much interest in the magnetic-field vs temperature phase diagrams of 2D and 3D frustrated lattice systems based on coupled triangles of spins [65],

[66]. The magnetic phase diagram for the 2D and 3D triangular lattice appear to be very similar. The 2D kagome phase diagram is very different, where the enhanced effect of frustration prevents the onset of conventional spin order.

Intriguingly, preliminary Monte Carlo simulation results for the 3D fcc kagome lattice suggest a phase diagram similar to the triangular lattice [67]. Additional simulations are needed to confirm this behavior as well as to study the impact of cubic anisotropy  $K$ .

# Bibliography

- [1] J. Villain *J. de Physique*, vol. 38, p. 26, 1977.
- [2] M. Mekata *Physics Today*, vol. 56 (2), pp. 12–13, 2003.
- [3] M. F. Collins and O. A. Petrenko *Canadian Journal of Physics*, vol. 75 (9), pp. 605–655, 1997.
- [4] H. T. Diep, *Magnetic Systems with Competing Interactions*. World Scientific Publishing Company, 1994.
- [5] H. T. Diep, *Frustrated Spin Systems*. World Scientific Publishing Company, 2004.
- [6] I. Tomeno, H. N. Fuke, H. Iwasaki, M. Sahashi, and Y. Tsunoda *J. Appl. Phys.*, vol. 86, p. 3853, 1999.
- [7] U. Hartmann, *Magnetic Multilayers and Giant Magnetoresistance*. Springer, 2000.
- [8] K. O’Grady, L. E. Fernandez-Outon, and G. Vallejo-Fernandez *J. Magn. Mater.*, vol. 97, p. 072501, 2010.
- [9] H. Takahashi, Y. Kota, T. Tsunoda, K. Kodama, A. Sakuma, and M. Takahashi *J. Appl. Phys.*, vol. 110, p. 123920, 2011.

- [10] H. Takahashi, M. Tsunoda, and M. Takahashi *IEEE Trans. Magn.*, vol. 48, p. 4347, 2012.
- [11] B. Wang *et al.* *Phys. Rev. Lett.*, vol. 110, p. 117203, 2013.
- [12] V. Hemmati, M. L. Plumer, J. P. Whitehead, and B. W. Southern *Phys. Rev. B*, vol. 86, p. 104419, 2012.
- [13] M. D. LeBlanc, M. L. Plumer, J. P. Whitehead, and B. W. Southern *Phys. Rev. B*, vol. 88, p. 094406, 2013.
- [14] M. D. LeBlanc, B. W. Southern, M. L. Plumer, and J. P. Whitehead *Phys. Rev. B*, vol. 90, p. 144403, 2014.
- [15] A. B. Harris, C. Kallin, and A. J. Berlinsky *Phys. Rev. B*, vol. 45, p. 2899, 1992.
- [16] G.-W. Chern and R. Moessner *Phys. Rev. Lett.*, vol. 110, p. 077201, 2013.
- [17] M. E. Zhitomirsky *Phys. Rev. B*, vol. 78, p. 094423, 2008.
- [18] P. Mendels and A. S. Wills, *Introduction to Frustrated Magnetism*, vol. 164 of *Springer Series in Solid-State Sciences*. Springer, Heidelberg, 2011.
- [19] K. Marty, V. Simonet, E. Ressouche, R. Ballou, P. Lejay, and P. Bordet *Phys. Rev. Lett.*, vol. 101, p. 247201, 2008.
- [20] S. T. Bramwell and M. J. P. Gingras *Science*, vol. 294, p. 1495, 2001.
- [21] A. W. C. Wong, Z. Hao, and M. J. P. Gingras *Phys. Rev. B*, vol. 88, p. 144402, 2013.

- [22] J. Villain, R. Bidaux, J. P. Carton, and R. Conte *J. Phys. France*, vol. 41, p. 1263, 1980.
- [23] C. L. Henley *Phys. Rev. Lett.*, vol. 62, p. 2056, 1989.
- [24] K. Matan, D. Grohol, D. G. Nocera, T. Yildirim, A. B. Harris, S. H. Lee, S. E. Nagler, and Y. S. Lee *Phys. Rev. Lett.*, vol. 96, p. 247201, 2006.
- [25] F. Shahbazi and S. Moretezapour *Phys. Rev. B*, vol. 77, p. 214420, 2008.
- [26] S. Schnabel and D. P. Landau *Phys. Rev. B*, vol. 86, p. 014413, 2012.
- [27] M. Spenke and S. Guertler *Phys. Rev. B*, vol. 86, p. 054440, 2012.
- [28] M. Tsunoda, H. Takahashi, and M. Takahashi *IEEE Trans. Magn.*, vol. 45, p. 3877, 2009.
- [29] L. Szunyogh *et al. Phys. Rev. B*, vol. 83, p. 024401, 2011.
- [30] A. E. Berkowitz and K. Takano *J. Magn. Magn. Mater.*, vol. 200, p. 552, 1999.
- [31] R. L. Stamps *J. Phys. D*, vol. 33, p. R247, 2000.
- [32] H. Chen, Q. Niu, and A. H. MacDonald *Phys. Rev. Lett.*, vol. 112, p. 017205, 2014.
- [33] E. Krén, G. Kádár, L. Pál, J. Sólyom, and P. Szabó *Phys. Lett.*, vol. 331, p. 20, 1966.
- [34] E. Krén, G. Kádár, L. Pál, J. Sólyom, P. Szabó, and T. Tarnóczy *Phys. Rev.*, vol. 171, p. 574, 1968.

- [35] A. Sakuma, R. Y. Umetsu, and K. Fukamichi *Phys. Rev. B*, vol. 66, p. 014432, 2002.
- [36] T. Ikeda and Y. Tsunoda *J. Phys. Soc. Jpn.*, vol. 72, p. 2614, 2003.
- [37] L. Szunyogh *et al.* *Phys. Rev. B*, vol. 79, p. 020403(R), 2009.
- [38] M. S. S. Challa, D. P. Landau, and K. Binder *Phys. Rev. B*, vol. 34, p. 1842, 1986.
- [39] K. Binder and D. P. Landau *Phys. Rev. B*, vol. 30, p. 1477, 1984.
- [40] S. Tsai and S. R. Salinas *Braz. J. Phys.*, vol. 28, p. 58, 1998.
- [41] A. Kohn, A. Kovacs, R. Fan, G. J. McIntyre, R. C. C. Ward, and J. P. Goff *Sci. Rep.*, vol. 3, p. 2412, 2013.
- [42] C. Kittel, *Introduction to Solid State Physics*. John Wiley and Sons, Inc., 2005.
- [43] C. Kittel, *Quantum Theory of Solids*. Wiley, 1987.
- [44] W. Marshall and S. W. Lovesey, *Theory of Thermal Neutron Scattering*. Clarendon Press, Oxford, 1971.
- [45] G. L. Squires, *Introduction to the Theory of Thermal Neutron Scattering*. Dover Publications, Inc., 1996.
- [46] J.-C. Tolédano and P. Tolédano, *The Landau Theory of Phase Transitions*. World Scientific Publishing Co., 1987.
- [47] V. T. Ngo and H. T. Diep *Phys. Rev. E*, vol. 78, p. 031119, 2008.

- [48] F. G. West *J. Appl. Phys.*, vol. 32, p. 249S, 1961.
- [49] J. D. M. Champion and P. C. W. Holdsworth *J. Phys.: Condens. Matter*, vol. 16, pp. S665–S671, 2004.
- [50] M. E. Zhitomirsky, P. C. W. Holdsworth, and R. Moessner *Phys. Rev. B*, vol. 89, p. 140403(R), 2014.
- [51] M. E. Zhitomirsky, M. V. Gvozdkova, P. C. W. Holdsworth, and R. Moessner *Phys. Rev. Lett.*, vol. 109, p. 077204, 2012.
- [52] J. T. Haraldsen, R. S. Fishman, and G. Brown *Phys. Rev. B*, vol. 86, p. 024412, 2012.
- [53] P. J. Brown, “ $\langle j_0 \rangle$  form factors for 3d transition elements and their ions,” <https://www.ill.eu/sites/ccsl/ffacts/ffactnode5.html>, 1998. [Online; accessed 10-May-2016].
- [54] A. Aczel. (Oak Ridge National Laboratory) Private Communication, 2016.
- [55] S. Yan, D. A. Huse, and S. R. White *Science*, vol. 332, p. 1173, 2011.
- [56] E. Rastelli and A. Tassi *J. Phys. C: Solid State Phys.*, vol. 19, p. L423, 1986.
- [57] E. Rastelli and A. Tassi *J. Phys. C: Solid State Phys.*, vol. 21, p. 1003, 1988.
- [58] A. P. J. Jansen *Phys. Rev. B*, vol. 33, p. 6352, 1986.
- [59] K. A. Ross, Y. Qiu, J. R. D. Copley, H. A. Dabkowska, and B. D. Gaulin *Phys. Rev. Lett.*, vol. 112, p. 057201, 2014.
- [60] M. L. Plumer *J. Phys. C*, vol. 17, p. 4663, 1984.

- [61] H. Takana, S. Teraoka, E. Kakehashi, K. Ito, and K. Nagata *J. Phys. Soc. Japan*, vol. 57, p. 3979, 1988.
- [62] R. M. Morra, W. J. L. Buyers, R. L. Armstrong, and K. Hirakawa *Phys. Rev. B*, vol. 38, p. 543, 1988.
- [63] S. A. Brazovskii, I. E. Dzyaloshinskii, and B. G. Kukharenko *Sov. Phys. JETP*, vol. 43(6), pp. 1178–1183, 1976.
- [64] H. V. Yerzhakov, M. L. Plumer, and J. P. Whitehead *J. Phys.: Condens. Matter*, vol. 28, p. 196003, 2016.
- [65] M. V. Gvozdkova, P. E. Melchy, and M. E. Zhitomirsky *J. Phys.: Condens. Matter*, vol. 23, p. 164209, 2011.
- [66] V. S. Maryasin and M. E. Zhitomirsky *Phys. Rev. Lett.*, vol. 111, p. 247201, 2013.
- [67] R. McGouran undergraduate honours thesis, University of Manitoba, 2013.
- [68] D. N. Zubarev *Soviet Phys. Uspekhi*, vol. 3, pp. 320–345, 1960.

# Appendix A

## Magnetic Neutron Scattering

### A.1 General Derivation

#### A.1.1 Neutron Scattering

In neutron scattering, a sample is bombarded by neutrons and the deflections are studied [45]. This is done by finding the partial differential cross section  $\frac{d\sigma^2}{d\Omega dE'}$  (energy dependent), differential cross section  $\frac{d\sigma}{d\Omega}$  (independent of the energy) or the total cross section  $\sigma_{\text{tot}}$  (independent of angle). When looking at elastic scattering, the goal is to find  $\frac{d\sigma}{d\Omega}$ , whereas inelastic scattering seeks  $\frac{d\sigma^2}{d\Omega dE'}$ . These quantities give the number of neutrons scattered per second within a small angle  $d\Omega$  divided by the incident neutron flux. The change in spin state of the neutrons are not considered in the present work, but can be studied with polarization experiments.

By considering the processes where the state of the scattering system changes from  $\lambda$  to  $\lambda'$  and the wavevector of a neutron changes from  $\mathbf{k}$  to  $\mathbf{k}'$  for angles inside  $d\Omega$ , the differential cross section depends on the number of transitions per second from one state to another. The starting point for finding these differential

cross sections is Fermi's golden rule, which connects this transition number to the number of momentum states for a potential  $V$  the neutron feels. Writing the final energy of the neutron as  $E' = \frac{\hbar^2}{2m}k'^2$ , it is possible to write the cross section as

$$\left( \frac{d\sigma^2}{d\Omega dE'} \right)_{\lambda \rightarrow \lambda'} = \frac{k'}{k} \left( \frac{m}{2\pi\hbar^2} \right)^2 | \langle \mathbf{k}'\lambda' | V | \mathbf{k}\lambda \rangle |^2 \delta(E_\lambda - E_{\lambda'} + E - E'), \quad (\text{A.1})$$

where the delta function comes from the energy distribution of the scattered neutrons. The next step involves finding an appropriate  $V$ . A Fermi pseudopotential  $V(\mathbf{r}) = \frac{2\pi\hbar^2}{m}b\delta(\mathbf{r})$  is used that involves the scattering length  $b$  (which depends on the nucleus and the spin state of the nucleus-neutron system) and the Dirac delta function  $\delta(\mathbf{r})$ . The scattering length can vary considerably for different nuclei and is often treated as a parameter that needs to be determined experimentally. The cross section is summed over all final states  $\lambda'$  before averaging over all  $\lambda$ . With  $\mathbf{R}_j$  being the nucleus  $j$  position,  $\boldsymbol{\kappa} = \mathbf{k} - \mathbf{k}'$  and  $\hbar\omega = E - E'$ , this ends up giving

$$\left( \frac{d\sigma^2}{d\Omega dE'} \right) = \frac{k'}{k} \frac{1}{2\pi\hbar} \sum_{jj'} b_j b_{j'} \int_{-\infty}^{\infty} \langle e^{-i\boldsymbol{\kappa} \cdot \mathbf{R}_{j'}(0)} e^{i\boldsymbol{\kappa} \cdot \mathbf{R}_j(t)} \rangle e^{-i\omega t} dt. \quad (\text{A.2})$$

Neutron scattering is separated into coherent and incoherent scattering, with the coherent scattering corresponding to having all scattering lengths  $b_j$  per nuclei being equal to an average and the incoherent scattering being the correction to this. The incoherent scattering is not considered here, as is often done.

### A.1.2 Nuclear Scattering

For nuclear scattering, the crystalline structure of the system is exploited to consider harmonic forces and normal modes. Due to thermal motion, a nucleus  $l$  moves from its equilibrium position with displacement  $\mathbf{u}$ . Defining  $U = i\boldsymbol{\kappa} \cdot \mathbf{u}_0(0)$  and using a phonon expansion, the coherent cross section becomes

$$\left( \frac{d\sigma^2}{d\Omega dE'} \right)_{\text{coh}} = \frac{\sigma_{\text{coh}}}{4\pi} \frac{k'}{k} \frac{N}{2\pi\hbar} e^{\langle U^2 \rangle} \sum_l e^{i\boldsymbol{\kappa} \cdot \mathbf{l}} \int_{-\infty}^{\infty} e^{-i\omega t} dt, \quad (\text{A.3})$$

and

$$\left( \frac{d\sigma}{d\Omega} \right)_{\text{coh,el}} = \frac{\sigma_{\text{coh}}}{4\pi} N \frac{(2\pi)^3}{v_0} e^{-2W} \sum_{\boldsymbol{\tau}} \delta(\boldsymbol{\kappa} - \boldsymbol{\tau}), \quad (\text{A.4})$$

where the factor  $2W = -\langle U \rangle^2$  is the Debye-Waller temperature factor, which is often ignored. Here,  $v_0$  is the unit cell volume, the delta sum comes from a rewriting of the lattice sum,  $\boldsymbol{\tau}$  is a reciprocal lattice vector,  $N$  is the number of nuclei in the crystal and  $\sigma_{\text{coh}} = 4\pi b$ . Coherent elastic scattering of neutrons can also be considered as Bragg scattering. Inelastic nuclear scattering follows from phonon scattering.

### A.1.3 Magnetic Scattering

For magnetic scattering, the spin state of the neutron matters, specifically in how it interacts with the system. In addition to the state  $\lambda$  and wavevector  $\mathbf{k}$ , the spin  $\sigma$  also needs to be averaged

$$\left( \frac{d\sigma^2}{d\Omega dE'} \right)_{\lambda \rightarrow \lambda'} = \frac{k'}{k} \left( \frac{m}{2\pi\hbar^2} \right)^2 | \langle \mathbf{k}' \sigma' \lambda' | V_m | \mathbf{k} \sigma \lambda \rangle |^2 \delta(E_\lambda - E_{\lambda'} + E - E'), \quad (\text{A.5})$$

with  $V_m$  the potential between all the electrons in the scattering system and the neutrons.

For a non-Bravais crystal at position  $\mathbf{R}_{ld}$  with  $l$  the ionic unit cell and  $d$  the index of the ion inside the unit cell, the cross section for spin-only scattering with localized electron can be derived to give

$$\begin{aligned}
\frac{d\sigma^2}{d\Omega dE'} &= (r_0)^2 \frac{k'}{k} \sum_{\alpha\beta} (\delta_{\alpha\beta} - \tilde{\kappa}_\alpha \tilde{\kappa}_\beta) \sum_{l'd'} \sum_{ld} F_{d'}^*(\boldsymbol{\kappa}) F_d(\boldsymbol{\kappa}) \\
&\times \sum_{\lambda\lambda'} p_\lambda \langle \lambda | e^{-i\boldsymbol{\kappa} \cdot \mathbf{R}_{l'd'}} S_{l'd'}^\alpha | \lambda' \rangle \\
&\times \langle \lambda' | e^{i\boldsymbol{\kappa} \cdot \mathbf{R}_{ld}} S_{ld}^\beta | \lambda \rangle \frac{1}{2\pi\hbar} \int_{-\infty}^{\infty} e^{i(E_{\lambda'} - E_\lambda)t/\hbar} e^{-i\omega t} dt.
\end{aligned} \tag{A.6}$$

Here,  $p$  is the momentum,  $F$  the magnetic form factor,  $\alpha$  and  $\beta$  the  $x, y, z$  coordinates and the  $S$  terms represent the spin vectors. Using time-dependent operators and assuming electron spins have almost no effect on the interatomic forces, the magnetic cross section can be given by

$$\begin{aligned}
\frac{d\sigma^2}{d\Omega dE'} &= \frac{(r_0)^2 k'}{2\pi\hbar k} \sum_{\alpha\beta} (\delta_{\alpha\beta} - \tilde{\kappa}_\alpha \tilde{\kappa}_\beta) \sum_{l'd'ld} F_{d'}^*(\boldsymbol{\kappa}) F_d(\boldsymbol{\kappa}) \\
&\times \int_{-\infty}^{\infty} \langle e^{-i\boldsymbol{\kappa} \cdot \mathbf{R}_{l'd'}(0)} e^{i\boldsymbol{\kappa} \cdot \mathbf{R}_{ld}(t)} \\
&\times \langle S_{l'd'}^\alpha(0) S_{ld}^\beta(t) \rangle e^{-i\omega t} dt.
\end{aligned} \tag{A.7}$$

Note that the  $\mathbf{R}$  terms are factored as the Debye-Waller expression.

For elastic scattering, the limit as  $t \rightarrow \infty$  is used, which decouples spin terms. It is then possible to integrate with respect to the energy. A similar approach can be used to find Eq. A.9 below [44].

## A.2 Elastic Scattering

The following provides some background theory of coherent elastic scattering [44],[45], relevant for the intensity obtained in neutron diffraction experiments for the fcc kagome antiferromagnet IrMn<sub>3</sub>.

Beginning with a derivation of the magnetic neutron scattering cross section, a fundamental constant for magnetic neutron scattering is  $r_0$  given by the gyromagnetic ratio times the classical electron radius

$$r_0 = \gamma \frac{\mu_0}{4\pi} \frac{e^2}{m_e} = -0.54 * 10^{-12} \text{ cm}, \quad (\text{A.8})$$

with  $\gamma = -1.913$ . The magnetic cross section can be written as

$$\frac{d\sigma}{d\Omega} = r_0^2 \sum_{l'} e^{i\boldsymbol{\kappa} \cdot (\mathbf{l} - \mathbf{l}')} |\hat{\boldsymbol{\kappa}} \times (\mathcal{F}(\boldsymbol{\kappa}) \times \hat{\boldsymbol{\kappa}})|^2, \quad (\text{A.9})$$

with the magnetic unit-cell vector structure factor

$$\mathcal{F}(\boldsymbol{\kappa}) = \sum_d e^{i\boldsymbol{\kappa} \cdot \mathbf{d}} \mathcal{F}_d(\boldsymbol{\kappa}), \quad (\text{A.10})$$

with

$$\mathcal{F}_d(\boldsymbol{\kappa}) = \int d\mathbf{r}^3 \mathbf{S}_d(\mathbf{r}) e^{i\boldsymbol{\kappa} \cdot \mathbf{r}}. \quad (\text{A.11})$$

Here,  $\mathbf{l}$  is the position vector for Bravais lattice vectors (with  $\mathbf{l}'$  used as a complement for the double sum),  $\boldsymbol{\kappa} = \mathbf{k}' - \mathbf{k}$  is the scattering vector,  $\mathbf{d}$  (and  $\mathbf{d}'$ ) denotes the position of a particular ion within the unit cell,  $\mathbf{r}$  is an arbitrary position vector and  $\mathbf{S}_d(\mathbf{r})$  is the ion spin vector. For particular ions in a unit cell with a spin

density, then

$$\mathcal{F}_d(\boldsymbol{\kappa}) = e^{-W_d(\boldsymbol{\kappa})} \frac{1}{2} g_d \langle S_d \rangle \hat{\mathbf{S}}_d(\boldsymbol{\kappa}) F_d(\boldsymbol{\kappa}). \quad (\text{A.12})$$

Note that the atomic spin vector is related to the spin density through

$$\boldsymbol{\rho}(\mathbf{r}) = \sum_{\mathbf{l}, \mathbf{d}} \mathbf{S}_d(\mathbf{r} - (\mathbf{l} + \mathbf{d})). \quad (\text{A.13})$$

Here,  $g_d$  is the Landé splitting factor,  $W_d$  is the in Debye-Waller temperature factor,  $\langle S_d \rangle$  is the thermal average value of the spin associated with the ion (not a vector quantity) which drops to zero at a critical temperature.  $\hat{\mathbf{S}}_d$ , which can also depend on  $\mathbf{l}$ , is the unit spin vector for ion  $\mathbf{d}$  and  $F_d(\boldsymbol{\kappa})$  is the (non-vector) atomic or magnetic form factor which drops off for large  $\boldsymbol{\kappa}$ , and is unity for  $\boldsymbol{\kappa} = \mathbf{0}$ . It is then possible to write

$$\mathcal{F}(\boldsymbol{\kappa}) = \sum_d e^{i\boldsymbol{\kappa} \cdot \mathbf{d}} e^{-W_d(\boldsymbol{\kappa})} \frac{1}{2} g_d \langle S_d \rangle \hat{\mathbf{S}}_d(\boldsymbol{\kappa}) F_d(\boldsymbol{\kappa}), \quad (\text{A.14})$$

to finally obtain (see Eq. 2.23)

$$\frac{d\sigma}{d\Omega} = r_0^2 \sum_{\mathbf{l}'} e^{i\boldsymbol{\kappa} \cdot (\mathbf{l} - \mathbf{l}')} \left| \sum_d e^{i\boldsymbol{\kappa} \cdot \mathbf{d}} e^{-W_d(\boldsymbol{\kappa})} \frac{1}{2} g_d \langle S_d \rangle F_d(\boldsymbol{\kappa}) \left[ \hat{\boldsymbol{\kappa}} \times \left( \hat{\mathbf{S}}_d(\boldsymbol{\kappa}) \times \hat{\boldsymbol{\kappa}} \right) \right] \right|^2, \quad (\text{A.15})$$

as the magnetic cross section. If all the unit cells are the same ( $\boldsymbol{\kappa}$  is periodic), then

$$\sum_{\mathbf{l}'} e^{i\boldsymbol{\kappa} \cdot (\mathbf{l} - \mathbf{l}')} = N \sum_{\mathbf{l}} e^{i\boldsymbol{\kappa} \cdot \mathbf{l}} = N \frac{(2\pi)^3}{\nu_0} \sum_{\boldsymbol{\tau}} \delta(\boldsymbol{\kappa} - \boldsymbol{\tau}), \quad (\text{A.16})$$

with  $N$  being the number of unit cells in the sample and  $\nu_0$  their volume.

The double cross product can be developed with

$$\mathbf{a} \times (\mathbf{b} \times \mathbf{c}) = \mathbf{b}(\mathbf{a} \cdot \mathbf{c}) - \mathbf{c}(\mathbf{a} \cdot \mathbf{b}), \quad (\text{A.17})$$

so that

$$\hat{\boldsymbol{\kappa}} \times (\hat{\mathbf{S}}_d(\boldsymbol{\kappa}) \times \hat{\boldsymbol{\kappa}}) = \hat{\mathbf{S}}_d - (\hat{\mathbf{S}}_d(\boldsymbol{\kappa}) \cdot \hat{\boldsymbol{\kappa}})\hat{\boldsymbol{\kappa}}. \quad (\text{A.18})$$

Noting that

$$\left| \sum_d \mathbf{f}_d \right|^2 = \sum_{dd'} \mathbf{f}_{d'}^* \cdot \mathbf{f}_d, \quad (\text{A.19})$$

the double cross product can then be written in a number of useful ways

$$\begin{aligned} \left| \sum_d \hat{\boldsymbol{\kappa}} \times (\hat{\mathbf{S}}_d(\boldsymbol{\kappa}) \times \hat{\boldsymbol{\kappa}}) \right|^2 &= \sum_{dd'} \left[ \hat{\mathbf{S}}_{d'} - (\hat{\mathbf{S}}_{d'}(\boldsymbol{\kappa}) \cdot \hat{\boldsymbol{\kappa}})\hat{\boldsymbol{\kappa}} \right] \cdot \left[ \hat{\mathbf{S}}_d - (\hat{\mathbf{S}}_d(\boldsymbol{\kappa}) \cdot \hat{\boldsymbol{\kappa}})\hat{\boldsymbol{\kappa}} \right], \\ &= \sum_{dd'} \hat{\mathbf{S}}_{d'} \cdot \hat{\mathbf{S}}_d - (\hat{\mathbf{S}}_{d'} \cdot \hat{\boldsymbol{\kappa}})(\hat{\mathbf{S}}_d \cdot \hat{\boldsymbol{\kappa}}), \\ &= \sum_{dd'} \sum_{\alpha\beta} (\delta_{\alpha\beta} - \hat{\boldsymbol{\kappa}}_\alpha \hat{\boldsymbol{\kappa}}_\beta) \hat{S}_{d'}^\alpha \hat{S}_d^\beta, \end{aligned} \quad (\text{A.20})$$

where  $\alpha$  and  $\beta$  are the  $x$ ,  $y$  and  $z$  coordinates.

This shows that a nonzero scattering intensity is expected only if the scattering vector  $\boldsymbol{\kappa}$  is perpendicular to the spins  $\mathbf{S}$ . This is a very useful feature for the purpose of determining the orientation of the spin density vector.

For the determination of crystal structures, the nuclear (non-magnetic) scattering cross section is useful. The coherent elastic scattering contribution for a non-Bravais crystal is given by

$$\left( \frac{d\sigma}{d\Omega} \right)_{\text{nuc,coh,el}} = N \frac{(2\pi)^3}{\nu_0} \sum_{\boldsymbol{\tau}} \delta(\boldsymbol{\kappa} - \boldsymbol{\tau}) |F_N(\boldsymbol{\kappa})|^2, \quad (\text{A.21})$$

where the nuclear structure factor is given by

$$F_N(\boldsymbol{\kappa}) = \sum_d \bar{b}_d e^{i\boldsymbol{\kappa} \cdot \mathbf{d}} e^{-W_d}. \quad (\text{A.22})$$

Here,  $\bar{b}_d$  is the scattering length, a known quantity for each individual type of atom, which depends on the atomic electronic structure.

## A.3 Inelastic Scattering

### A.3.1 Green's Functions

The description outlined here is based on notes provided by Prof. B. Southern (Univ. of Manitoba). The relevant parts of the scattering cross section for inelastic magnetic scattering are given as [44]

$$\left( \frac{d^2\sigma}{d\Omega dE'} \right)_{\text{inel}} \propto \frac{k'}{k} F(\boldsymbol{\kappa})^2 S(\boldsymbol{\kappa}, \omega), \quad (\text{A.23})$$

where  $F(\boldsymbol{\kappa})$  is the form factor and  $S(\boldsymbol{\kappa}, \omega)$  is the dynamic structure factor. As stated in Chap. 2,

$$S(\boldsymbol{\kappa}, \omega) = \sum_{\alpha, \beta=x, y, z} S^{\alpha\beta}(\boldsymbol{\kappa}, \omega) (\delta_{\alpha\beta} - \hat{\kappa}_\alpha \hat{\kappa}_\beta), \quad (\text{A.24})$$

where  $S^{\alpha\beta}(\boldsymbol{\kappa}, \omega)$  is the double Fourier transform of the correlation function  $\langle S_i^\alpha(0) S_j^\beta(t) \rangle$  and can be calculated using the spin wave analysis dispersion relations along with standard Green's functions techniques [44].  $S^{\alpha\beta}(\boldsymbol{\kappa}, \omega)$  is equal to

the imaginary part of the time Fourier transform of the retarded Green's function

$$G^{\alpha\beta}(\boldsymbol{\kappa}, t) = -i\theta(t) \langle [S_{\boldsymbol{\kappa}}^{\alpha}(t), S_{-\boldsymbol{\kappa}}^{\beta}(0)] \rangle. \quad (\text{A.25})$$

This Green's function satisfies

$$\begin{aligned} i\hbar \frac{\partial}{\partial t} G^{\alpha\beta}(\boldsymbol{\kappa}, t) &= \hbar\delta(t) \langle [S_{\boldsymbol{\kappa}}^m(t), S_{-\boldsymbol{\kappa}}^n(0)] \rangle \\ &\quad - i\theta(t) \langle [[S_{\boldsymbol{\kappa}}^{\alpha}(t), \mathcal{H}], S_{-\boldsymbol{\kappa}}^{\beta}(0)] \rangle, \end{aligned} \quad (\text{A.26})$$

or

$$\omega G^{\alpha\beta}(\boldsymbol{\kappa}, \omega) = \frac{1}{2\pi} \langle [S_{\boldsymbol{\kappa}}^m(t), S_{-\boldsymbol{\kappa}}^n(0)] \rangle + \langle [[S_{\boldsymbol{\kappa}}^{\alpha}(t), \mathcal{H}], S_{-\boldsymbol{\kappa}}^{\beta}(0)] \rangle. \quad (\text{A.27})$$

The correlation function or equivalent Green's functions for  $\langle S_{\boldsymbol{\kappa}}^{\alpha} S_{-\boldsymbol{\kappa}}^{\beta} \rangle$  is needed, and thus has 81 components since there are 3 Cartesian elements and 3 sublattices.

In local coordinates, the Cartesian  $z$  components are not considered, leaving 36 local Green's functions that satisfy

$$\omega \tilde{\mathbf{G}} = i\tilde{\mathbf{z}} + i\boldsymbol{\Gamma} \tilde{\mathbf{G}}, \quad (\text{A.28})$$

where  $\tilde{\mathbf{z}}$  is a 6-component column vector involving commutators of the spin operators in the correlation function, and  $\boldsymbol{\Gamma}$  is the 6x6 matrix of Eq. 5.20.

For example, the correlation function  $\langle \tilde{S}_{-\kappa_y}^A \tilde{S}_{\kappa_x}^A \rangle$  involves the Green's func-

tions

$$\tilde{\mathbf{G}} = \begin{pmatrix} \langle\langle \tilde{S}_{\kappa_x}^A \tilde{S}_{-\kappa_y}^A \rangle\rangle \\ \langle\langle \tilde{S}_{\kappa_x}^B \tilde{S}_{-\kappa_y}^A \rangle\rangle \\ \langle\langle \tilde{S}_{\kappa_x}^C \tilde{S}_{-\kappa_y}^A \rangle\rangle \\ \langle\langle \tilde{S}_{\kappa_y}^A \tilde{S}_{-\kappa_y}^A \rangle\rangle \\ \langle\langle \tilde{S}_{\kappa_y}^B \tilde{S}_{-\kappa_y}^A \rangle\rangle \\ \langle\langle \tilde{S}_{\kappa_y}^C \tilde{S}_{-\kappa_y}^A \rangle\rangle \end{pmatrix}, \quad \tilde{\mathbf{z}} = \begin{pmatrix} \frac{1}{2\pi} \\ 0 \\ 0 \\ 0 \\ 0 \\ 0 \end{pmatrix} \quad (\text{A.29})$$

such that  $\tilde{\mathbf{G}} = (\omega\mathbf{I} - i\mathbf{\Gamma})^{-1}i\tilde{\mathbf{z}}$  with  $\langle\langle \rangle\rangle$  denoting the double time Green's function [68]. Other Green's functions are obtained in a similar manner. A small imaginary part is added to  $\omega \rightarrow \omega + i\epsilon$ . Only the transverse correlations in the local frame are considered as the  $z$ -components yield the elastic scattering. The correlations in the crystal frames can be transformed into local coordinates using the proper rotations matrices.

### A.3.2 Calculation of $S(\boldsymbol{\kappa}, \omega)$

The following establishes the transformation of the inverted matrix obtained above into  $S(\boldsymbol{\kappa}, \omega)$ . Here,  $\gamma_1, \gamma_2$  represent sublattices A, B, and C and  $\alpha, \beta$  represent  $x, y, z$ , with indices starting at 1. The  $i, j$  variables represent the  $x, y$  2D components from the spin wave calculations used in producing  $\mathbf{\Gamma}$ , the 6x6 matrix for the local frame, and  $\iota$  is the imaginary unit here (to avoid confusion with the indices  $i$  and  $j$ ). The multiplication by the  $\mathbf{M}$  rotation matrices components transforms the results from the local reference frame where the  $z$  component is not considered into the crystal axes frame. Simple algebra is used to obtain the correct components for the inverted matrix  $\mathbf{T} = [(\omega + \iota\epsilon)\mathbf{I} - \iota\mathbf{\Gamma}]^{-1}$ , with  $\tilde{\mathbf{G}} = \mathbf{T}\iota\tilde{\mathbf{z}}$

$$p_{\alpha,\beta}^{\gamma_1,\gamma_2} = \iota \sum_{i=1}^2 \sum_{j=1}^2 (2i-3) M_{\alpha,i}^{\gamma_1} M_{\beta,j}^{\gamma_2} T_{3(j-1)+\gamma_2,3(2-i)+\gamma_1}, \quad (\text{A.30})$$

$$\begin{aligned} S(\boldsymbol{\kappa}, \omega) &= S(\kappa_x, \kappa_y, \kappa_z, \omega) = S(\kappa, \theta, \phi, \omega) \\ &= \text{Im} \left[ \sum_{\alpha=1}^3 \sum_{\beta=1}^3 \sum_{\gamma_1=1}^3 \sum_{\gamma_2=1}^3 p_{\alpha,\beta}^{\gamma_1,\gamma_2} (\delta_{\alpha\beta} - \hat{\kappa}_\alpha \hat{\kappa}_\beta) \right]. \end{aligned} \quad (\text{A.31})$$

## A.4 Elastic Cut of Experimental Data

From the experimental inelastic scattering powder results of Fig. 5.7, it is possible to do horizontal “cuts” that amount to elastic scattering by averaging within the range  $E = -1$  meV to 1 meV to obtain a 2D graph. The averaging helps remove some of the effects of any background scattering from the aluminum sample holder. Fig. A.1 shows this cut for  $E_i = 100$  meV at  $T = 5$  K before any aluminum subtraction is done, while Fig. A.2 shows the same results after subtraction (using ORNL provided software).

The scattering includes both nuclear and magnetic peaks. Ordered peak locations corresponding to the [100], [110], and [210] directions around  $Q = 1.67 \text{ \AA}^{-1}$ ,  $2.37 \text{ \AA}^{-1}$  and  $3.75 \text{ \AA}^{-1}$ , respectively, are seen. A MnO byproduct magnetic peak is seen around  $Q = 1.23 \text{ \AA}^{-1}$  as the temperature is below its transition temperature  $T_N = 116$  K. Aluminum peaks are also present around  $Q = 2.70 \text{ \AA}^{-1}$  and  $3.05 \text{ \AA}^{-1}$  before and after subtraction, indicating that the subtraction was not complete. Finally, there is a smaller peak that appears around  $3.50 \text{ \AA}^{-1}$  that remains unexplained. Peaks at larger values of  $Q$  correspond to higher harmonics.

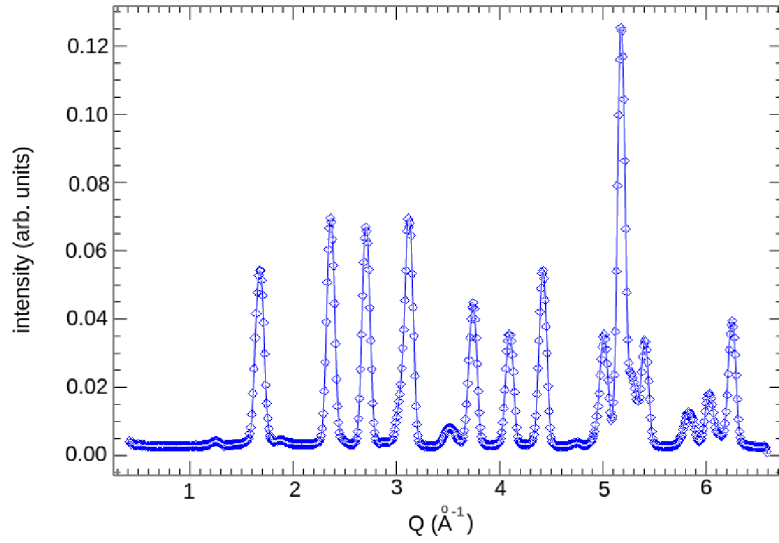


Figure A.1: Elastic cut of the inelastic data before aluminum subtraction. Peaks are marked in Fig. A.2.

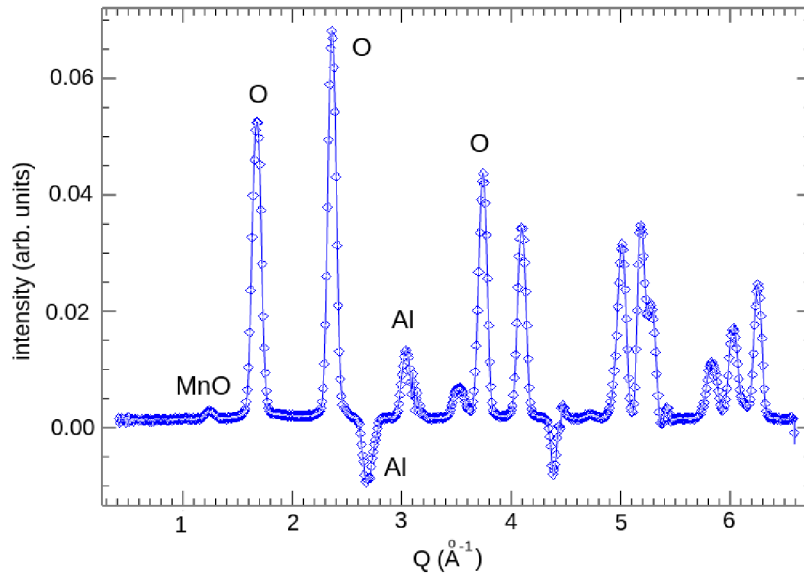


Figure A.2: Elastic cut of the inelastic data after aluminum subtraction. Several known  $\text{IrMn}_3$  ordered phase (O), aluminum (Al), and MnO peaks are marked.

## A.5 Single Crystal Calculations

Shown in Fig. A.3 are calculated results for  $S(Q, E)$  with  $Q$  along certain directions. These results are given for a single crystal and not powder. Here,

$J = J' = 20$  meV,  $K = 2$  meV, and an incident energy of 100 meV. The form factor term is included along with the term  $k_f/k_i$  in Eq. 5.31.

Along the [100] direction, the Bragg positions are  $2\pi/a = 1.67$  and  $6\pi/a = 5.03$  with  $a = 3.75\text{\AA}$ . There is a difficult to see low energy dispersionless mode at about 12.6 meV caused by the anisotropy. Along the [110] direction, the Bragg position is at  $2\pi/a2^{1/2} = 2.37$  which is not seen in the powder average results of Fig. 5.6. There are no low energy modes along this direction, but there is a gap of around 12 meV. The Bragg point along the [210] direction is at  $2\pi\sqrt{5}/a = 3.75$ , but there is significant low energy scattering at the  $[1\frac{1}{2}0]$  and  $[3\frac{3}{2}0]$  points. For the [210] direction, there is only the Bragg point around 4.1. Finally, the [111] direction has a Bragg point around 2.9 with a smaller contribution of intensity. This is contradictory to the expected result of having no scattering for [111].

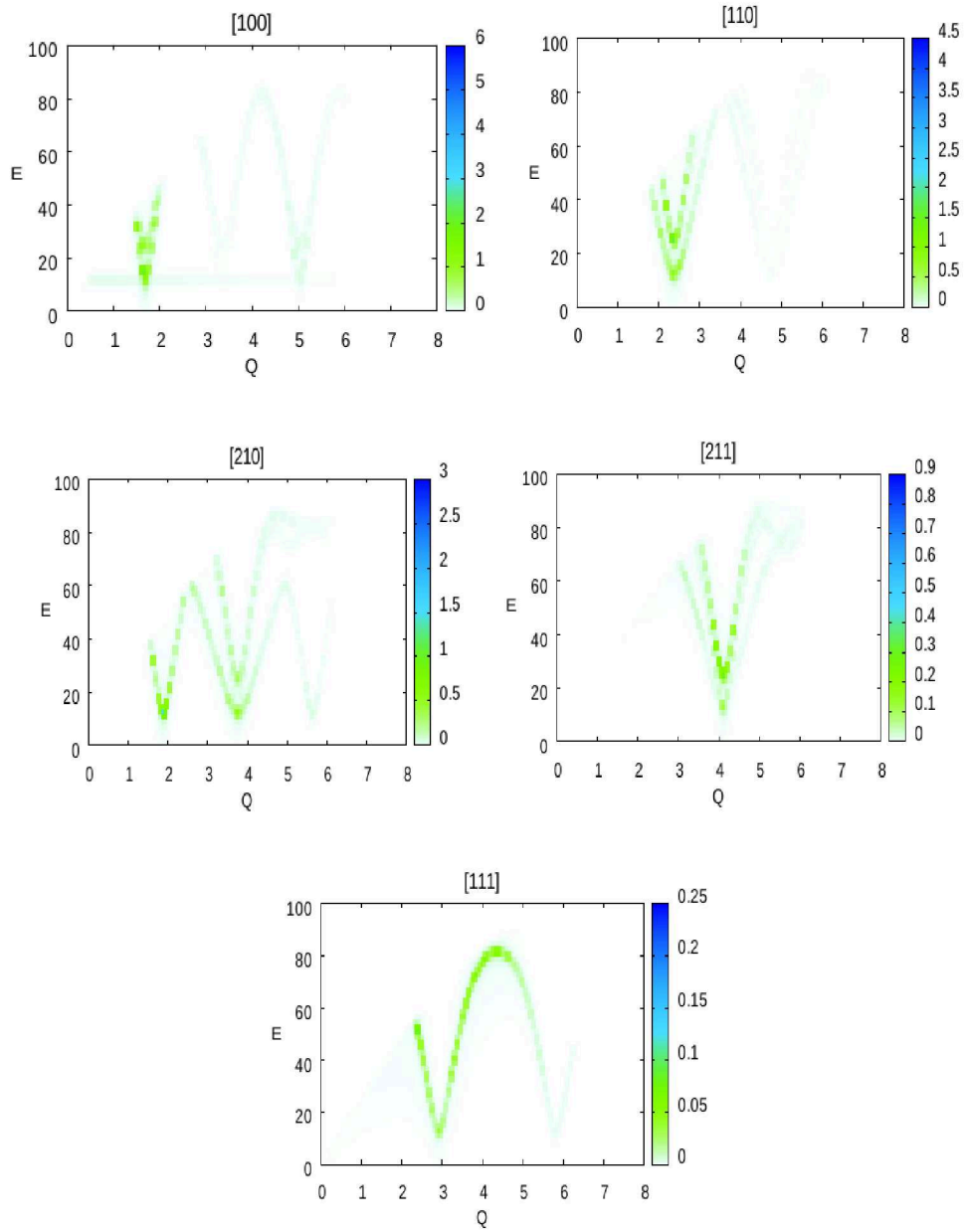


Figure A.3: Predicted  $S(Q, E)$  intensities for a single crystal sample along specific  $Q$  directions.  $J = J' = 20$  meV,  $K = 2$  meV, and an incident energy of 100 meV. The form factor term is included along with the term  $k_f/k_i$  in Eq. 5.31. Figures provided by Prof. B. Southern (Univ. of Manitoba).